

Department of Physics and Astronomy

University of Heidelberg

Diploma Thesis

in Physics

submitted by

Michael Mommert

born in

Schwetzingen

2009



# Polarimetric monitoring of Blazars at San Pedro Martir

This diploma thesis has been carried out by Michael Mommert

at the

Landessternwarte, Zentrum für Astronomie der Universität Heidelberg

under the supervision of

Mr. Priv.-Doz. Dr. Jochen Heidt



## Polarimetrische Überwachung von Blazaren am Standort San Pedro Martir

Ziel dieser Arbeit ist der Aufbau einer Software-Pipeline zur Reduktion und Analyse von polarimetrischen Aufnahmen mit dem 0.84 m Teleskop am *Observatorio Astronómico Nacional* in San Pedro Martir, Mexiko. Zusätzlich sollen die Qualität der Messungen und des Aufbaus untersucht werden.

Die Pipeline basiert auf dem Software-Paket IRAF und erlaubt eine automatisierte Reduktion, sowie photometrische und polarimetrische Analyse der Daten in kürzester Zeit. Photometrische Messungen hoher Genauigkeit sind möglich bis hin zu Grenzgrößen von 17 mag und mehr. Polarimetrische Messungen unterliegen einer höheren Ungenauigkeit deren Ursache nicht genau identifiziert werden konnte. Das Teleskop zeigt eine vernachlässigbar kleine instrumentelle Polarisation von  $(0.6 \pm 0.5)\%$ , die Rotation der Bildfeldebene gegenüber der Himmelsebene beträgt  $(-91 \pm 2)^\circ$ .

## Polarimetric Monitoring of Blazars at San Pedro Martir

The aim of this work is to develop a software pipeline for the reduction and analysis of polarimetric images with the 0.84 m telescope at *Observatorio Astronómico Nacional* in San Pedro Martir, Mexico. Additionally, the quality of measurements and setup are subject to investigation.

The pipeline is based on the IRAF software package and allows an automated reduction, as well as photometric and polarimetric analysis of the data in shortest time. Photometric measurements of high accuracy are possible up to limiting magnitudes of 17 mag and more. Polarimetric measurements are subject to a higher imprecision. The source of this could not exactly be identified. The telescope setup shows a neglectable small instrumental polarization of  $(0.6 \pm 0.5)\%$ , the rotation of the field-of-view against the sky orientation is determined to be  $(-91 \pm 2)^\circ$ .



Ich widme diese Arbeit meinen Eltern

**Christa und Peter Mommert**

und meinem Bruder

**Sascha Mommert**

ohne deren Unterstützung mein Studium und diese Arbeit nicht möglich gewesen wären.

I dedicate this work to my parents

**Christa and Peter Mommert**

and to my brother

**Sascha Mommert**

Without your support, my studies and this work would not have been possible.





# Contents

<b>1</b>	<b>Motivation</b>	<b>5</b>
1.1	The SPM Project . . . . .	5
1.1.1	Scientific Motivation . . . . .	5
1.1.2	Expected Scientific Goals . . . . .	6
1.1.3	Target List . . . . .	6
1.1.4	Observers and Observing Runs . . . . .	7
1.2	Aims of this Thesis . . . . .	7
<b>2</b>	<b>Theoretical Basics</b>	<b>9</b>
2.1	Blazars . . . . .	9
2.1.1	AGN . . . . .	9
2.1.2	Blazars . . . . .	16
2.2	CCD Astronomy . . . . .	18
2.2.1	CCD Detectors . . . . .	18
2.2.2	Image Acquisition and Reduction . . . . .	19
2.2.3	Image Postreduction . . . . .	23
2.3	Photometry . . . . .	23
2.3.1	Apparent Magnitude . . . . .	23
2.3.2	Signal-to-Noise Ratio and Errors . . . . .	24
2.3.3	Airmass . . . . .	26
2.4	Polarimetry . . . . .	27
2.4.1	Polarization Basics . . . . .	27
2.4.2	Mathematical Description of Polarization . . . . .	29
2.4.3	Application of Polarimetry in this Thesis . . . . .	31
2.5	Polarization in Astronomy . . . . .	32
2.5.1	Synchrotron Emission . . . . .	32
<b>3</b>	<b>Data Acquisition</b>	<b>35</b>
3.1	Observatory . . . . .	36
3.1.1	Observatory Site . . . . .	36
3.1.2	The 0.84m Telescope . . . . .	36
3.1.3	POLIMA Filter Wheel (Polarimeter) . . . . .	37
3.1.4	CCD Detectors . . . . .	38

---

3.2	Image Acquisition	39
<b>4</b>	<b>Data Processing - the Polima pipeline</b>	<b>41</b>
4.1	IRAF	41
4.1.1	Additional Software	42
4.2	Goals and Features of the Pipeline	43
4.2.1	Goals	43
4.2.2	Main Features	43
4.3	The <code>polima</code> package	44
4.3.1	Content	44
4.3.2	Installation	45
<b>5</b>	<b>Image reduction</b>	<b>47</b>
5.1	Raw Image Preparation - <code>polima.polidentify</code>	47
5.1.1	Parameters	47
5.1.2	Description	48
5.2	Reduction Task - <code>polima.polprocess</code>	50
5.2.1	Preface	50
5.2.2	Parameters	50
5.2.3	Description	52
5.3	Post Reduction Handling - <code>polima.popol</code>	55
5.3.1	General Concepts of Object Identification	55
5.3.2	Parameters	56
5.3.3	Description	58
5.3.4	Cosmics Correction	59
5.4	Auxiliary Tasks	60
5.4.1	<code>chimagetyp</code>	60
5.4.2	<code>chobject</code>	60
5.4.3	<code>chpolangle</code>	61
5.4.4	<code>checkcoo</code>	61
5.4.5	<code>cpcoo</code>	61
<b>6</b>	<b>Photometry</b>	<b>63</b>
6.1	Aperture Photometry	63
6.2	Photometry Software - <code>dophotometry</code>	65
6.2.1	Preface	65
6.2.2	Parameters	65
6.2.3	Description	67
6.3	Testing	69
6.3.1	Reliability of Results	69
6.3.2	Best Aperture Determination	70
6.3.3	Conclusion	71
6.4	Photometry Results	72
6.4.1	Results of the October/November Run 2008	72

---

6.4.2	Long-term Results of BL Lac, 1ES 1959+650 and OJ 287 . . . . .	77
<b>7</b>	<b>Polarimetry</b>	<b>79</b>
7.1	Polarization Measurements . . . . .	79
7.2	Polarimetry Script - <code>dopolarimetry</code> . . . . .	80
7.2.1	Parameters . . . . .	80
7.2.2	Description . . . . .	81
7.2.3	Testing . . . . .	83
7.2.4	Polarization Angle Calibration . . . . .	85
7.2.5	Instrumental Polarization . . . . .	89
7.2.6	Problems . . . . .	90
7.3	Polarimetry Results . . . . .	93
7.3.1	Results of the October/November Run 2008 . . . . .	93
7.3.2	Long-term Results of BL Lac, 1ES 1959+650 and OJ 287 . . . . .	98
<b>8</b>	<b>Conclusion</b>	<b>101</b>
8.1	Image Reduction - the <code>Polima</code> Pipeline . . . . .	101
8.2	Photometry . . . . .	101
8.3	Polarimetry . . . . .	102
<b>9</b>	<b>Discussion</b>	<b>103</b>
9.1	Telescope Setup . . . . .	103
9.1.1	Recommendations . . . . .	103
9.2	Image Reduction . . . . .	106
9.3	Photometry . . . . .	106
9.4	Polarimetry . . . . .	106
9.4.1	Scatter of Polarimetric Results . . . . .	106
	<b>Appendix</b>	<b>108</b>
<b>A</b>	<b>Target Lists</b>	<b>109</b>
A.1	Objects . . . . .	109
A.2	Standard Stars . . . . .	109
<b>B</b>	<b>Further Results</b>	<b>113</b>
B.1	October/November Run 2008 . . . . .	113
<b>C</b>	<b>Using the <code>Polima</code> Pipeline</b>	<b>127</b>
C.1	Image Reduction . . . . .	127
C.2	Post Reduction Handling . . . . .	129
C.3	Image Analysis . . . . .	130
<b>D</b>	<b>Pipeline Source Code</b>	<b>133</b>
<b>E</b>	<b>Acknowledgments</b>	<b>139</b>



# Chapter 1

## Motivation

This diploma thesis contributes to the SPM project, which is outlined in the following section.

*After a scientific motivation the expected goals of the project are introduced as well as the target list. Eventually, the contribution of this work to the project is pointed out.*

### 1.1 The SPM Project

The long-term project *Polarimetric monitoring of Blazars at San Pedro Martir* (SPM Project) is a collaboration of ten scientists and three Ph.D. and diploma students, mainly from Mexico, the US and Europe, which are involved in the project. Principal Investigator (PI) of the project is Jochen Heidt from Landessternwarte Heidelberg, Co-PI is Erika Benitez from UNAM Mexico City.

The project started in July 2008 and is initially set up for a duration of 3 years. Data acquisition takes place at the *Observatorio Astronómico Nacional* at San Pedro Martir in Mexico, where a 0.84 m telescope is mainly used for this purpose. A number of up to 37 objects is monitored over a period of seven nights centered on each new moon phase. Further information on the observatory and imaging process can be found in chapter 3.

The SPM project is closely connected to the *GLAST-AGILE support program*<sup>1</sup> (GASP), which is a collaboration within the *Whole Earth Blazar Telescope*<sup>2</sup> (WEBT). The former is a project to provide optical-to-radio long-term continuous monitoring of a list of selected gamma-ray-loud blazars during the operation of the *AGILE*<sup>3</sup> and *FERMI*<sup>4</sup> (formerly known as *GLAST*) gamma-ray satellites. The latter is a network of optical, near-infrared, and radio observers who in concert have the capability to obtain continuous, high-temporal-density monitoring of blazars.

#### 1.1.1 Scientific Motivation

Numerous multiwavelength campaigns from the observational side as well as theoretical modeling on the other have largely improved our understanding of how the central engine of blazars - presumably a supermassive Black Hole - and their associated relativistic jets work. Still, many

---

<sup>1</sup><http://www.to.astro.it/blazars/webt/gasp/homepage.html>

<sup>2</sup><http://www.to.astro.it/blazars/webt/>

<sup>3</sup><http://agile.iasf-roma.inaf.it/>

<sup>4</sup><http://fermi.gsfc.nasa.gov/>

details are an open issue such as the exact accretion mechanism onto the supermassive Black Hole, how the relativistic jets are launched as well as the onset and evolution of shocks within the jets. Especially the latter are of high interest since they are most likely responsible for the strong variability observed across the entire wavelength range accessible nowadays from ground and space in this class of active galactic nuclei.

Today several models exist to explain multifrequency variations observed in Blazars. These are based on different physical processes and can be discriminated using polarimetric measurements over a wide frequency range. Of particular interest in such observations is the interplay between the variable radiation observed at low frequencies, created by Synchrotron radiation, using radio telescopes and at high frequencies, which is most likely inverse-Compton radiation. However, this method of testing requires support from ground-based telescopes in the optical as a test for the Synchrotron branch.

Optical observations of Blazars are routinely carried out since more than a decade in a large number of observatories. However, the observations are traditionally carried out by means of flux measurements only, which allow to investigate e.g. the energy budget in these sources. So far largely neglected has been the potential of determining the properties of the sources in polarized light. This is a powerful tool, to e.g. determine strength and orientation of magnetic fields giving rise to the variable synchrotron radiation. Only few programs are currently conducted in this direction.

### 1.1.2 Expected Scientific Goals

The main scientific goals of the SPM project are

- Determine statistically the duty cycle, i.e. the variability in total and polarized light, changes/stability of polarization angle etc. on timescales of days on a long-term basis and compare them with other properties of the sources. This will be done for high priority sources.
- Monitor the sources as part of the GASP program and to set an alert in case of unexpected high activity of one of the sources.
- Participate in multi-wavelength campaigns initiated due to high activity of one of the GASP-sources or other ones.

### 1.1.3 Target List

The target list consists of blazars that are well known for their variabilities in total flux. They also show highly polarized emission in the radio and optical wavelengths. Most of the targets are radio-selected, few are X-ray-selected. This list is essentially build upon the GASP source list.

The total number of 37 objects is divided into two sections. 17 objects are part of the high priority list, 20 of them form the low priority list. A complete listing can be found in A.1.

High priority targets are supposed to be observed each night when possible. They are mainly selected due to their brightness ( $m_R \lesssim 16$  mag), which allows observing them easily without spending too much integration time. On the opposite, low priority target are fainter and need more integration time. They should be observed when necessary, i.e. for multifrequency campaigns with

---

other telescopes or if major variations are reported. To all targets a unique 5 character object code has been assigned to in order to simplify designation.

To calibrate polarization measurements, a list of highly polarized and unpolarized standard stars is available.

#### 1.1.4 Observers and Observing Runs

Observations are performed by the participants of the SPM project, which are in particular

- Jochen Heidt, Landessternwarte Heidelberg, project PI
- Erika Benitez, UNAM Mexico City, Co-PI
- David Hiriart, UNAM Ensenada, Director of the observatory
- Kari Nilsson, Tuorla Observatory (Finland), data quality control
- Deborah Dultzin, UNAM Mexico City
- Jose Manuel Lopez, UNAM Ensenada, PhD student
- Marco Sorcia, UNAM Mexico City, PhD student
- Raul Mujica, INAOE Tonanzintla (Mexico)
- Ivan Agudo, Instituto de Astrofisica de Andalucia (Spain)
- Svetlana Jorstad, Boston University, (USA)
- Matthias Dietrich, Ohio State University (USA)
- Alan Marscher, Boston University, (USA)
- Michael Mommert, Landessternwarte Heidelberg, diploma student

Observation runs are scheduled during the nights around new moon. One run usually covers seven successive nights. A listing of all observing runs so far is displayed in Tab. 1.1.

## 1.2 Aims of this Thesis

This thesis is divided into two major parts:

- production of a software pipeline to automatize image reduction and analysis to the highest possible degree
- characterization of the existing setup's ability to perform polarimetric measurements

Thus, it contributes to the project by simplifying data processing and analysis on the one hand and to test the setups limits on the other one. Especially, the limiting direct imaging object brightness is supposed to be determined, which is estimated to be 16 mag from previous measurements.

Table 1.1: Listing of observing runs with according observer

<b>Run</b>	<b>Observer</b>
October 17 - 24, 2007	David Hiriart, Jochen Heidt and Marco Sorcia
November, 12 -14, 2007	David Hiriart and Jose Manuel Lopez
February 26 - 29, 2008	David Hiriart and Jose Manuel Lopez
March, 8 - 14, 2008	David Hiriart and Jose Manuel Lopez
April, 10 - 17, 2008	David Hiriart and Jose Manuel Lopez
May, 3 - 8, 2008	David Hiriart, Jochen Heidt and Kari Nilsson
June, 2 - 6, 2008	David Hiriart and Erika Benitez
July, 7 - 13, 2008	David Hiriart and Jose Manuel Lopez
July, 29 - August 4, 2008	Erika Benitez
August 28 - September 2, 2008	Raul Mujica and guest
September 26 - October 2, 2008	David Hiriart, Jose Manuel Lopez and Marco Sorcia
October 24 - November 4, 2008	Jochen Heidt, Jose Manuel Lopez and Michael Mommert
November 27 - December 3, 2008	Ivan Agudo and Jose Manuel Lopez
January 23 - 29, 2009	David Hiriart and Jose Manuel Lopez
February 21 - 27, 2009	David Hiriart and Jose Manuel Lopez
March 23 - 29, 2009	Marco Sorcia
April 22 - 28, 2009	Michael Mommert
May 21 - 27, 2009	Raul Mujica
June 19 - 25, 2009	Erika Benitez
July 18 - 24, 2009	David Hiriart
August 15 - 22, 2009	not yet decided
September 17 - 23, 2009	not yet decided
October 14 - 20, 2009	not yet decided
November 12 - 18, 2009	not yet decided



# Chapter 2

## Theoretical Basics

This chapter outlines the theoretical basics which are used in this work.

*In the first part, astronomical terms are introduced and explained. The second part deals with technical ideas concerning data processing. Eventually, the concepts of photometry and polarimetry are outlined.*

### 2.1 Blazars

Blazars are a subgroup of the most powerful group of objects known today, which are called *Active Galactic Nuclei (AGN)*. These are introduced in the first section following. The second section gives an outline of the special features of Blazars.

#### 2.1.1 AGN

##### Historical View

First representatives of the AGN family were examined by Carl Seyfert in 1943. Objects studied by him - now called *Seyfert galaxies* - are galaxies showing an extremely high surface brightness of the core area and emission lines of high excitation. Some of these lines are extremely strong and broad, leading to the assumption of very high velocities of the emitting gas when interpreted as Doppler broadening. Later examinations by Woltjer in 1959 showed that the extent of the emitting regions in the cores of Seyfert galaxies must be relatively small, since they appear to be point-like. Assuming the emitting gas to be gravitationally bound and demanding its high degree of excitation, this speaks for an enormous mass concentration in the center of the galaxy.

A next important step in the history of AGNs was the completion of the *3C* and *3CR* radio catalogs in 1960. Many of these *3C* objects were able to be positionally matched with known optical galaxies. This identification process, however, turned out to be difficult due to the high positional uncertainty of this early radio measurements. Some *3C* objects showed no optical counterpart.

In 1963 Matthews and Sandage showed the point-like nature of the source *3C 48*. Its complex optical spectrum contains a blue continuum and strong, broad emission lines which could not be assigned to any atomic transition and therefore remained unidentified. Maarten Schmidt identified in the same year the radio source *3C273* with a point-like optical counterpart, which also showed

strong and broad emission lines. He was able to identify the emission lines as those of the Balmer series of hydrogen, which are shifted to longer wavelengths at an - at that time extremely high - redshift of  $z = 0.158$ . Presuming the validity of the Hubble law this implies an enormous distance of the object and an absolute brightness of the object, which is 100 times higher than normal spiral galaxies. Due to the point-like nature of the emission region, this enormous luminosity must origin from a small spatial region. This leads to the definition of the terms *Active Galactic Nucleus (AGN)* and *Quasar* as an abbreviation for the term *quasi-stellar radio source*. Many quasars have been identified in quick succession as a result of the improving determination of radio source positions. [Sch06]

Over the years many different types of AGN have been discovered. In the following subsections, general and some specific observational AGN features are introduced, an overview of the "AGN Zoology" is given and a unified model of AGN is outlined.

### Observational features

In the following, some observational features of AGN are listed. They may be shared by different types of AGN or be specific to one or some specific types.

**Point-like appearance** AGN are compact regions at the center of a galaxy with a much higher than normal luminosity. Therefore, they usually appear to be point-like objects. However, some objects in the lower redshifted regime are still close enough to be able to resolve the hosting galaxy, which is called *active galaxy*.

The extent of some radio source in AGN can reach 1 *Mpc* or even more. Emission in other wavelength regimes are concentrated in the center of the AGN.

**Electromagnetic spectrum** The spectra of AGN completely differ from those of normal galaxies. The latter represent an overlap of many different star spectra, i.e. thermal emission spectra. However, the former show a completely different behaviour ruled by *non-thermal emission*.

The general spectral behaviour of an AGN is sketched in Fig. 2.1 using a QSO (cf. 2.1.1) as prototype (the special features of QSOs are introduced in 2.1.1). The plot shows  $\nu F_\nu$ , a measure of energy per time impacting a certain area, in arbitrary units over a wide frequency range using a double-logarithmic scale.

There are two main classes of AGN, which have to be distinguished: *radio-loud* and *radio-quiet* types. The former show strong emission in the radio and X-ray/ $\gamma$ -ray regimes following a power law, the latter show weaker emission. The power law distribution clearly speaks for non-thermal emission, since thermal emission creates a spectral distribution according to the Planck-law. A feature both types have in common is the so called *Blue Bump*, a global maximum of the spectral energy distribution located in the UV regime. Besides this global maximum a local one exists in the M-IR regime - the IR-bump.

**Broad emission lines** The UV and optical spectra of quasars and some other AGN types feature strong and very broad emission lines. Typically, lines of the Balmer series and Ly  $\alpha$  of hydrogen are observed together with some metal lines. The width of a line can be specified either as a wavelength (e.g. FWHM) or a velocity if the line width is interpreted as Doppler broadening. Typical line

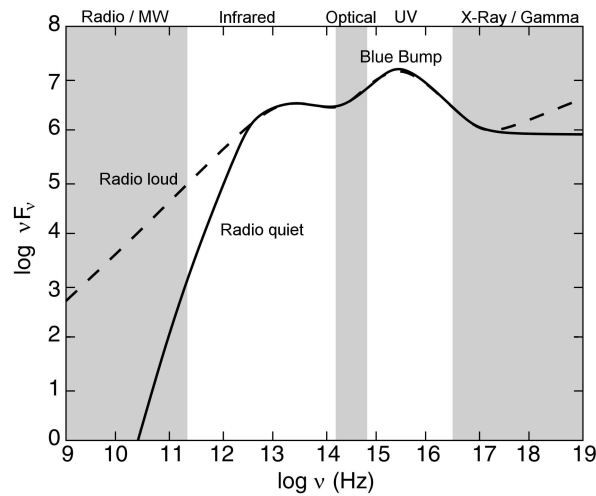


Figure 2.1: Sketch of the characteristic spectral behaviour of a QSO (taken from [Sch06]) Only darkened frequency ranges are observable from Earth-bound telescopes.

widths of broad lines show velocities of  $10^5$  km/s, narrow lines around 100 km/s. Thus, the narrow emission lines are still broad compared to the typical velocities in normal galaxies. This speaks for a high kinetic energy of the emitting material.

**High luminosity and variability** Luminous QSOs have luminosities up to  $L \approx 10^{47}$  erg/s, which makes them the most luminous objects in the universe (apart from Gamma Ray Bursts, which do not emit continuously).

The luminosity of some AGN varies by more than 50% on time-scales of a day. From this variability time-scale, an upper limit of the spatial extent of the emitting region can be estimated.

**Jets** Some active galaxies show linear structures in the optical regime originating from the nucleus of the galaxy. Optical features in this jet often match features in the radio regime and may evolve in the time-scale of years. Furthermore, matter packages - so-called *blobs* - moving along the jet have been observed. Blobs move at velocities close to the speed of light.

A famous example for an optical jet emerges from the elliptical galaxy M87 (Fig. 2.2).

**X-ray emission** X-ray emission is observed in some AGN. Continuum emission may be emitted by a jet and the hot corona of the accretion disc via scattering processes. The spectrum can be described by a power-law spectrum in both cases. X-ray line emission is a result of excitation of cold heavy elements by the X-ray continuum.

## AGN Zoology

To have a rough overview, the most important AGN types are listed below and some of their characteristics are outlined. A quick overview over all types and a comparison to a normal galaxy can be found in Tab. 2.1.

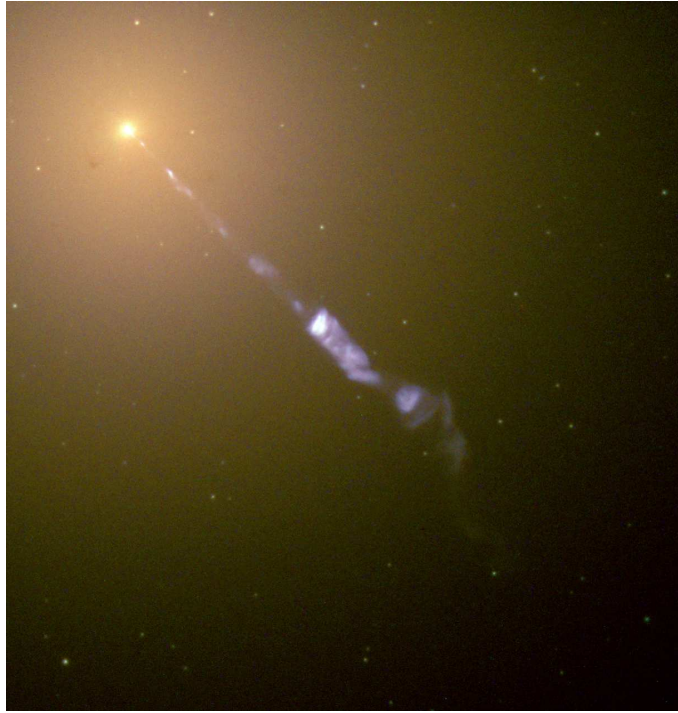


Figure 2.2: Optical jet emerging from M87 (image credit: NASA and The Hubble Heritage Team (STScI/AURA))

As a first distinctive feature, the emission in the radio regime is used to define one group of *radio-loud* and another one of *radio-quiet* objects. This differentiation is more historically conditioned, since radio-selected AGN were the first ones to be discovered. Selections using other wavelength regimes, e.g. X-ray-selection followed. Today it is clear, that all AGN types show radio emission, but with strong differences in flux. Hence, an arbitrary threshold of radio flux distinguishes between radio-loud and radio-quiet objects. Therefore, this differentiation is not used here.

**Quasars** The most luminous AGN, usually at high redshifts with a blue optical energy distribution containing strong and broad emission lines. The term *quasar* (Quasi-Stellar Radio Object) was usually intended to describe only radio-loud objects. Using photometric surveys, a number of radio-quiet quasars were found, which were first designated as *QSO* (Quasi-Stellar Objects). Today, about 10 times more radio-quiet QSOs than quasars are thought to exist. Therefore, the terms quasar and QSO today share the same meaning.

**Seyfert galaxies** On optical images they are identified as spiral galaxies hosting an extremely bright core. Their luminosity is considerably lower than that of quasars and they are radio-quiet.

One has to distinguish between *Type 1* and *Type 2* Seyfert galaxies: Seyfert 1 galaxies show both broad and narrow emission lines, while Seyfert 2 galaxies only show the narrow ones. Today, intermediate variants are known.

The spectra of quasars and Seyfert 1 galaxies are very similar. The separation of both types is historical due to the different methods of discovering them. Except for the different core luminosity,

Table 2.1: Overview of features of AGN types and normal galaxies

Galaxy Type	Emission lines		strong emission in ...			
	Narrow	Broad	X-ray	Radio	Jets	Variability
normal galaxy	weak	✗	weak	✗	✗	✗
quasar	✓	✓	some	some	some	✓
Seyfert 1	✓	✓	some	✗	✗	✓
Seyfert 2	✓	✗	some	✗	✗	✓
BLRG	✓	✓	some	✓	✓	✓
NLRG	✓	✗	some	✓	✓	✓
OVV	✗	✓	✓	✓	✓	✓
BL Lac	✗	✗	✓	✓	✓	✓

there does not seem to be a fundamental physical difference between both. Hence, both classes - together with the later introduced BLRGs - are often combined as *Type 1-AGN*. A *Type 2-AGN* is therefore the analog of a Seyfert 2 galaxy, i.e. an AGN not showing broad emission lines. The last combined type in this list is given by the family of blazars.

**Radio galaxies** Radio galaxies are elliptic galaxies containing an active nucleus. They can be considered a radio-loud Seyfert 1 and Seyfert 2 galaxies, which are called *Broad-Line Radio Galaxies (BLRG)* and *Narrow-Line Radio Galaxies (NLRG)* respectively.

**OVV** *Optical Violently Variables* are a radio-loud subclass of quasars which are characterized by a very strong and rapid variability of its optical radiation and strong emission and absorption lines in its spectra. Furthermore, they stand out due to the relatively high degree of optical polarization.

**BL Lacs** This type of AGN - like OVV - is characterized by its strong variability but does not show strong emission or absorption lines. Optical radiation is highly polarized and they are radio-loud. The lack of emission lines complicates the determination of the distance of these objects.

Due to the similar variability characteristics of both OVV and BL Lac they are often collectively called *blazars*.

All blazars are radio sources. Besides their optical violent variability - luminosity may vary over several magnitudes - blazars show highly energetic and strongly variable radiation in the  $\gamma$ -ray regime.

### Physical AGN model

Due to the usually large distances of AGN it is impossible to resolve the source of radiation. Therefore, the observational features listed above must be used to determine the physical components and circumstances which characterize an AGN.

AGN activity is only observed - if resolvable - in the center of spiral and elliptic galaxies. The

existence of broad emission lines in some types of AGN and the high luminosity emerging from a spatially small region argue for an extremely efficient and compact energy source. It is widely believed that only accretion onto a black hole is able to produce such amounts of energy, since the conversion of gravitational energy to kinetic energy is the most efficient process to achieve this. Using the observed luminosity one can derive an estimation for the mass of the black hole. The result is that *supermassive black holes (SMBHs)* with up to several  $10^8$  solar masses are required to drive the observed processes. Time-scales of brightness variability give an estimation for the spatial extension of the active region leading to sizes comparable to the extension of the Solar System.

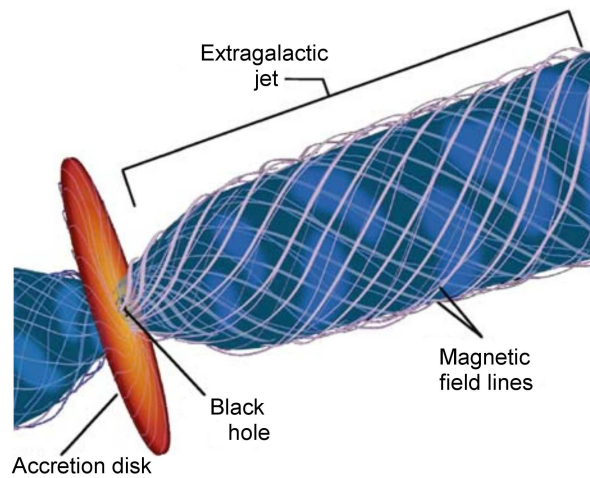


Figure 2.3: Illustration of the relativistic jet model. The host galaxy is concentrically arranged around the accretion disk. (taken from [Sch06])

The SMBH is fed from the host galaxy by accretion processes. This leads to a flat and extremely dense rotating *accretion disk* surrounding the black hole. The extreme conditions inside the disk are believed to give rise to x-ray and  $\gamma$ -ray emission, which is observed in some AGN. Furthermore, the gas of the disk is highly ionized leading to strong magnetic fields that penetrate the disk.

Jets, which are observed in many types of AGN, are launched from the center of the disk in both directions perpendicular to the disk plane. They play an important role by carrying away angular momentum from the rotating disk. The ejected gas reaches velocities which are close to the speed of light. The exact launching processes are still an open question but it is widely believed to be connected to strong magnetic field lines, which are created in the disk. These are drilled due to the rapid rotation of the disk and lead to an acceleration of ionized gas to such enormous velocities. Gas particles moving on curvature trajectories due to magnetic fields emit *synchrotron emission* (cf. 2.5.1), i.e. highly polarized non-thermal emission mostly observed in the optical and radio regime. The most distanced parts of the jets interact with the ambient gas and create shock fronts. The deceleration of the high velocity gas leads to emission in the radio regime, which is observed as so called radio-lobes. Therefore, radio emission regions usually match with jet structures. However, in many objects only one jet is observed instead of both ones. This can be explained as a matter of the viewing angle which leads to relativistic beaming of the incoming

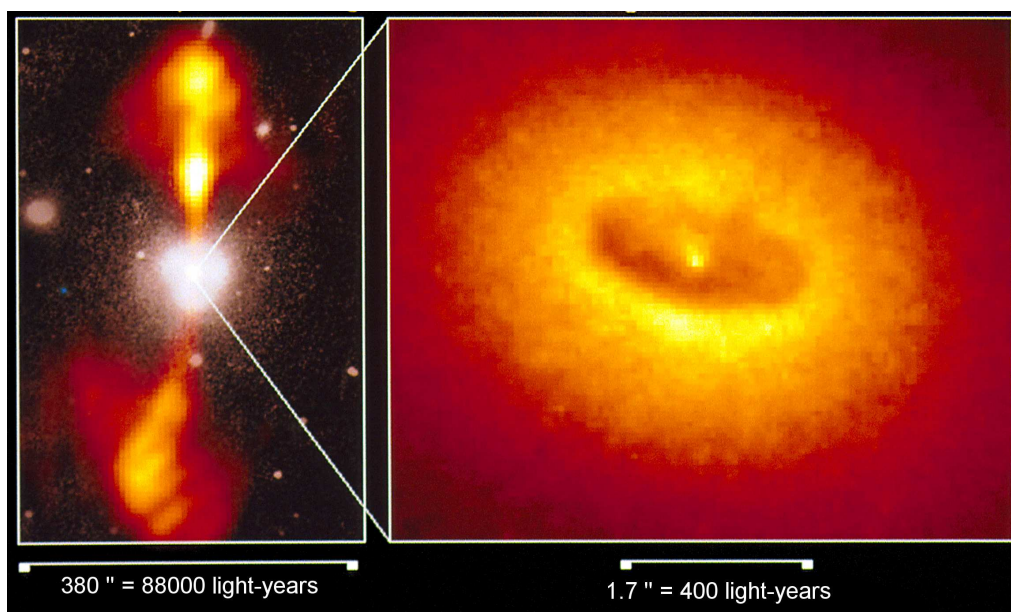


Figure 2.4: Core of the elliptic galaxy NGC 4261. The left image was taken with ground-based optical and radio telescopes. The reddish part shows the radio jet. The right image was taken using the Hubble Space Telescope. It shows the central part of the galaxy around the AGN containing hot gas and a dust disk which envelopes the accretion disk. [image credit: National Radio Astronomy Observatory, California Institute of Technology (left), Walter Jaffe/Leiden Observatory, Holland Ford/JHU/STScI, and NASA (right)]

jet, i.e. an amplification of the luminosity of the incoming jet and a weakening of the counterpart, or obstruction of the counterjet by the host galaxy.

The high degree of variability in many wavelength regimes is a consequence of fluctuations of the density distribution in the disk and gas clouds being ejected in the jet. Such *blobs* have already been observed.

### Unified Model of AGN

Many properties of AGN are common to all types, others are specific to some types. This leads to the question, whether the different classes of AGN consist of rather similar objects which differ in their appearance or whether one is dealing with completely different phenomena. Similarities in the 'AGN zoology' arouse the idea of a unification scheme which is based on the geometry between object and observer ([UP95] and [Ant93]).

The general idea is that all AGN follow the same physical model introduced above. However, the accretion disk is segregated from the host galaxy by a *dust torus* which absorbs most radiation from the inner regions (Fig. 2.5). In the vicinity of the black hole and the accretion disk, gas is heated from both and therefore thermally excited leading to broad emission lines. This region is designated as *broad line region (BLR)*. Outside the dust torus, the ambient gas is less thermally excited and emission lines are narrower. This is the *narrow line region (NLR)*. A relativistic jet is believed to emerge from every AGN. However, its visibility depends on effects like relativistic beaming or redshift.

The impression of the object and therefore the identification now depends on the observer's inclination angle. The following scenarios are possible and visualized in Fig. 2.5.

- *edge-on observation* The vicinity of the black hole and the accretion disk are obstructed by the dust torus. Only the narrow line region (NLR) is visible. If a jet is visible, the observer identifies the object as a BLRG, otherwise as a Seyfert 2 galaxy.
- *medium inclination* The observer is able to see at least parts of the accretion disk and the broad line region (BLR). The AGN would be classified as a Seyfert 1 galaxy or a BLRG, respectively.
- *face-on observation* In this case the inclination angle is very high, so that the jet is pointing in the direction of the observer. If the jet is visible, the object is identified as OVV or BL Lac. If there is no jet visible, the object is identified as radio-quiet quasar.

This unification scheme is widely acknowledged and in use.

#### 2.1.2 Blazars

As outlined before, blazars form a group of objects showing a strong variability over a wide wavelength range, i.e. from  $\gamma$ -rays to radio emission. Some objects even show variations on intraday timescales<sup>1</sup>.

---

<sup>1</sup>Heidt & Wagner, 1996, AA: Statistics of optical intraday variability in a complete sample of radio-selected BL Lacertae objects



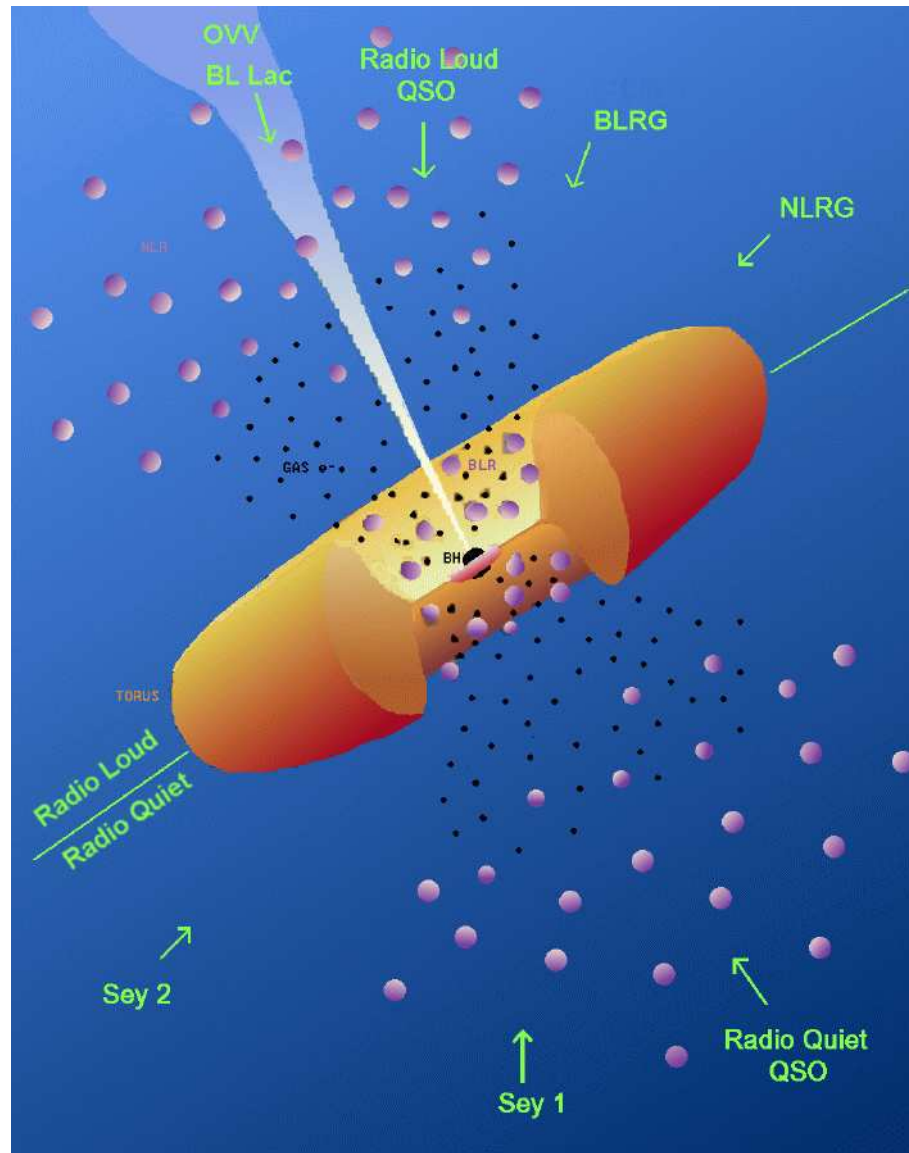


Figure 2.5: AGN unification scheme (taken from *The BeppoSAX Calendar 1999*, adapted from [UP95])

Compared to other AGN the variability behaviour seems to be much more violent in blazars. The reason for this incidence is called *relativistic beaming*, which states that the apparent luminosity of a jet can be much larger than the intrinsic luminosity, if the observer 'looks into' the relativistic jet. The same effects leads to the observation of single jets. Due to the conservation of momentum, each jet has a counterjet, ejecting in the opposite direction. Relativistic beaming leads to a weakening of the counterjet's luminosity which may be inobservable.

Another feature of blazars is the high degree of polarization over a wide wavelength range. A high degree of polarization means that more than 4% of the incoming light is polarized. Blazars can reach polarization degrees of up to and even more than 30%. The origin of the polarized light is *synchrotron emission*, i.e. radiation emitted by relativistic electrons which are forced to move on curvature trajectories due to magnetic fields. The magnetic field is created in the accretion disk. The field lines are drilled above the disk and believed to be involved in the jet launching, acceleration and focussing. Therefore, polarimetric measurements are a unique measure to probe the magnetic field and other physical processes involved.

## 2.2 CCD Astronomy

In the history of astronomy several different detector types have been used to perform measurements. The first and most simple detector used was the naked eye. It allowed estimations of the brightness and position of objects in the night sky. However, this kind of measurement is highly biased, since the impressions of the human eye are subjective, i.e. one and the same phenomenon might lead to different observational results when examined by two observers. Furthermore, the accuracy of both photometric and astrometric measurements is rather poor.

This accuracy was increased by the use of telescopes starting in the 17th century, but subjectivity remained as a main problem. A revolutionary step to solve this problem was the introduction of photographic plates in astronomy in the 19th century. For the first time, this allowed quantitative and reproduceable analysis of data. Furthermore, increased integration times allowed the detection of much fainter objects.

With the rise of semiconductor technology in the 1980's, the first CCD cameras appeared and photographic plates became obsolete. This detector type combines the advantages of digital technologies with the reproduceability of the photographic plate without some of its disadvantages.

### 2.2.1 CCD Detectors

A Charge-Coupled Device (CCD) detector is a two-dimensional array of semiconductor elements which are working as light-sensitive metal oxide semiconductor capacitors on a silicon substrate. Photons hitting the array release electrons from the semiconductor material according to the inner photoelectric process. These electrons are trapped in a potential well created by an anode for the duration of the integration time.

Professional detectors today contain up to several million pixels, each with a edge length of some  $\mu\text{m}$ . In order to transform the electric charge collected in one pixel into a computer readable signal, each CCD contains a readout register, an amplifier and an analogue-to-digital converter.

The readout process is sketched in Fig. 2.6. The  $5 \times 9$  array represents the CCD pixel array

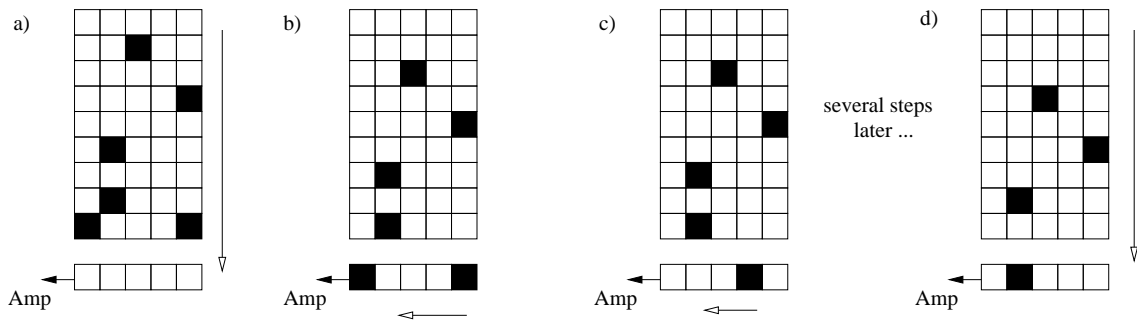


Figure 2.6: Principle of CCD readout process

and the line beneath stands for the readout register which is connected to the amplifier and the converter.

In the readout process the charge of each pixel is shifted line by line into the register by changing polarisation of the capacitors (a). The register is then read out pixel by pixel into the amplifier and the A/D converter (b). Here, collected charge is measured as a voltage and amplified before it is converted to a digital signal. This process is repeated until the register is empty and the next line can be read out into it (d).

The result is a two dimensional array of values that represents the spatial charge distribution on the chip. The digital values of each pixel are measured in *ADU* (*Analogue-to-Digital Unit*). The amount of electrons (or photons) needed to produce 1 ADU is called the *gain* factor of the device. There is a maximum number of ADUs one pixel can accept which depends on the *dynamical range* of the CCD. Professional devices usually have 16bit A/D converters, which means that the charge distribution collected by one pixel is assigned to one of  $2^{16} = 65536$  possible ADU values.

Compared to photographic plates, CCDs show a good linear behaviour between the charge collected within each pixel and the ADU output over a wide range. Nonlinearities can be observed close to the saturation of a pixel.

Another advantage of CCDs over photographic plates is the superior *quantum efficiency* (*QE*), which describes what fraction of the incoming photons are detected and which usually is a function of the wavelength. While plates reach QEs of 10% using specialized production processes like hypersensitization, modern CCD detectors easily reach QEs of 90% and more in specific wavelengths. Furthermore, photographic plates show a higher sensitivity in the UV to blue regime, while CCDs are more sensitive in the red to IR regime, which is more appropriate for astronomical use. However, CCD devices can also be modified to be sensitive for shorter wavelengths.

Some characteristics of the CCD devices used in the SPM project can be found in section 3.1.4. Further information on CCDs can be found in [How06].

## 2.2.2 Image Acquisition and Reduction

CCD detectors are software controlled which simplifies the imaging process compared to photographic plates. This includes the adjustment of imaging parameters like integration time and binning. *Binning* means the grouping of a number of pixels which are read out as a single pixel. The advantage of this method is an increased light sensitive area and a smaller relative read out noise per (unbinned) pixel.

When starting the integration the camera shutter opens and photons fall on the CCD surface. The *shutter* usually has the form of an iris that has to open quickly to prevent the CCD from being illuminated inhomogeneous. Shutter vignetting has to be considered if short integration time (e.g.  $< 5s$ ) are used.

After the integration time has passed the shutter closes and the image is read out and transferred to the computers memory. The downloaded image is not immediately useable for data reduction. It contains noises and artifacts caused by thermal effects and the readout process. Since the sources of this noise are well known, it is possible to correct the image, which is called *image reduction*. This is explained and visualized in Fig. 2.7 using an image of the galaxy M51 taken by the author using a semi-professional CCD camera.

The raw image Fig. 2.7 (i) shows a lot of noise and an inhomogeneous background illumination. To extract the signal from the image one has to use correction images like bias, flatfield and darkframe, which are introduced in the following paragraphs.

**Bias and Overscan** Pixel values are scattered according to a gaussian distribution around a mean value during the readout process, which is called *readout noise*. As a result negative ADU values might occur. However these cannot be interpreted by the A/D converter. To prevent the pixel values from being negative, a constant bias value  $B$  is added in form of a constant voltage to the measured one.

$$S_i^T = S_i + B$$

with the total measured pixel value  $S_i^T$  and the real signal value  $S_i$ . To obtain the real signal, this bias has to be subtracted from the image.

There are two ways to correct for the bias:

- *Bias frames*, which are taken with closed shutter and the shortest possible integration time, are subtracted from the raw image
- a constant bias value is subtracted from the image, which is obtained from the *overscan region*; this region is not a physical part of the CCD device itself but a number of pseudo-pixels which are generated by sending additional readout cycles

Using a bias frame has the advantage of correcting for two-dimensional noise as it may be caused by an amplifier (as can be seen in Fig. 2.7 (ii)) or *hot pixels*, which are damaged pixels that always seem to be saturated. On the other hand, using the overscan correction gives the best estimation for the bias, since pseudo-pixels are subject to readout noise only. Both methods can be used parallel to obtain the best correction, which is done in this work.

**Darkframe** Even in the complete absence of light, a CCD pixel accumulates charges due to the thermal energy of the electrons. This leads to a *dark current*  $S_d(t, T)$  which depends on the CCDs temperature  $T$  and the integration time  $t$ . One gets the relation

$$S_d(t, T) \approx T^{3/2} \cdot \exp[-E_g/(2k_B T)] \cdot t$$

with the Boltzmann constant  $k_B$  and the  $E_g$  the band gap of the semiconductor material. According to this, it is desirable to run the CCD at a very low temperature to minimize this thermal noise.

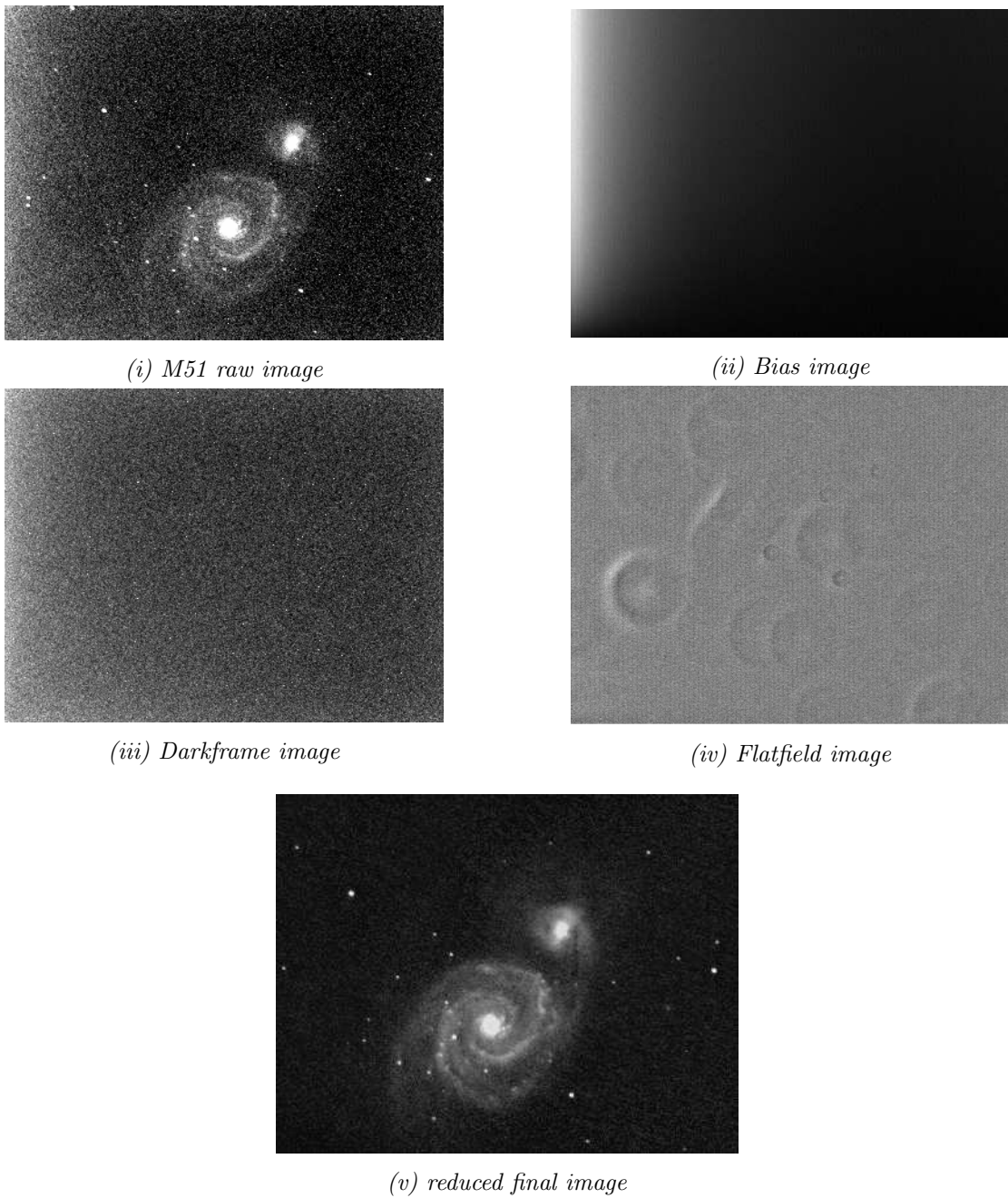


Figure 2.7: raw image, correction images and resulting image

As for bias frames, the darkframe is additive:

$$S_i^T = S_i + S_d(t, T)$$

and has to be subtracted from the science image. To obtain a darkframe, one has to integrate as long as the scientific image but with the shutter closed, to measure only the thermal noise. Another method is using the overscan region, which includes thermal noise, too.

Since modern CCD devices are cooled using liquid nitrogen, thermal noise has been decreased to

level which makes the use of darkframes unnecessary.

The example showed in Fig. 2.7 (iii) was taken using a semi-professional CCD device with thermoelectric cooling. This type of cooling is easier to handle but not sufficient. The image shows a uniform dark noise distribution.

**Flatfield** The sensitivity of pixels in a CCD array underlies spatial variations when imaging a homogenous illuminated surface which can not be avoided as part of the production process. Additional to that, there might be dust or other contaminations on the detector or the optical elements, which absorbs light. In order to perform photometric measurements, these inhomogeneities have to be taken into account using a flatfield image. To obtain a flatfield image, a uniformly illuminated area has to be imaged. The resulting flatfield image shows contaminations and CCD sensitivity variations.

One distinguishes between two kinds of flatfield images:

**Dome Flat** A white canvas or the telescopes dome itself is illuminated by artificial light and imaged using the complete optical system and the CCD. The advantage of this method is, that it is easy to do and the flatfield can be produced at any time, even in daytime. One disadvantage is that artificial light shows another wavelength characteristic than the light of night sky objects or the night sky background. This may lead to an incomplete correction.

**Sky Flat** In this case the twilight sky during dusk or dawn is imaged to get the flatfield. Since the field of view of the CCD is rather small there is no gradient expected. The advantage compared to the dome flat is that the wavelength characteristic of the twilight sky resembles pretty well to the one of the star light. The disadvantage is that there is little time to take a sky flat each night. Stars shining through the background light affecting the flatfield can be removed by medianing over several flats and dithering. It might be of relevance, whether sky flats are taken during dusk or dawn due to the different incident angle.

Once flatfield images are taken, they have to be normalized to a mean pixel value. Now, it is possible to assign a sensitivity  $I_i$  to each pixel which stands for its sensitivity normalized to a mean value  $I_0$ . So the signal one specific pixel measures  $S_i$  is

$$S_i = I_i \cdot S_0$$

with  $S_0$  being the homogenous illumination intensity. In order to get the real incoming signal one has to divide by the sensitivity  $I_i$ . Hence, the science image has to be divided by the flatfield image.

**Image combination** Each CCD image, science or correction image, contains noise. Sources of this noise are the dark current mentioned above and others, which are discussed in 2.3.2. Measures exist to minimize this noise down to a certain degree. When applying correction images to science images using image arithmetics the noise level of each participating image propagates to the resulting image. Therefore it is eligible to have low noise correction images, since a number of these are applied to each science image.

As known from the theory of errors, a set of independent measurements may lead to a smaller error of the combined measurement. This can be transferred to CCD imaging. If a set of  $n$  images

is combined using the *mean*, the noise of the combined image is  $1/\sqrt{n}$  the mean noise of a single image. However, the mean is prone to outliers, which may be induced by cosmics. For this reason, the *median* is usually used for the combinatin of astronomical images. This reduces the noise level significantly.

Correction images are usually combined using a set of 5 or more raw images and the median. These combined images are referred to as *masterbias*, *masterflat* and *masterdark*.

### 2.2.3 Image Postreduction

After applying all the image reduction steps mentioned above, the image is cleaned from most detector characteristic noises. However, there are still some corrections necessary to be able to analyze the image.

**Cosmics Rejection** High energy particles hitting the CCD are able to release electrons by collision ionisation. The origin of these particles can be extraterrestrial (e.g. supernovae) or terrestrial (decay product of radioactive atoms). On an image, these impacts appear as small, sharp-edged streaks. The latter characterizes the so called *cosmics*. The sharp-edged occurrence is due to their origin in the detector material. Therefore their image is not influenced by the telescope's optic. Hence, their signal is not convolved with the telescope's point-spread-function (cf. 6.1). That allows a robust detection of cosmics. They are removed by replacing the affected pixels using interpolation.

Now, the image is cleaned from all influences which can be corrected automatically. Some artifacts might remain, which are difficult to remove like satellite or airplane trails, reflections or fringes. These demand a special treatment which usually cannot be automatized. Suggesting, the image does not suffer from one of the above listed artifacts, it is ready to perform photometry, polarimetry or other analysis methods.

## 2.3 Photometry

Photometry means the measurement of the flux of an astronomical object's electromagnetic radiation. This demands a quantitative determination of the amount of radiation that impacted the detector during the integration time. Methods to obtain this information from an astronomical image are introduced in 6.1.

This section explains the equations which turn a measured flux into an object's magnitude. Furthermore, errors and problems of photometry are be discussed.

### 2.3.1 Apparent Magnitude

The first classification of stars according to their brightness was done by Hipparchos in ancient greece. He created six classes in which he divided all with the naked eye visible stars by brightness. He grouped the brightest stars in the first class and the dimmest ones into the sixth class. This rather qualitative classification was replaced by a more quantitative one by Pogson in 1856, which intentioned to follow the old one as close as possible. The idea is based on the fact that the

human perception of brightness is logarithmic and the postulate, that a star of the first class is about a hundred times brighter than a star of the sixth class, which originated from the old classification. This leads to the definition that a difference in brightness of two stars from successive classes equals a brightness ratio of  $\sqrt[5]{100} = 2.512 \approx 2.5$ . The resulting relation between the magnitudes  $m_1, m_2$  of two stars with fluxes  $F_1, F_2$  can be displayed in two different forms depending on the photometric method used to obtain the magnitude. The two most important methods are:

**Absolute Photometry** calculates the magnitude of an object directly from the measured flux. To have a calibration point, a zeropoint of magnitude  $m_0$  has to be defined which can be obtained from calibration measurements.

$$m = m_0 - 2.5 \log_{10} F \quad (2.1)$$

This method is easy to apply but needs a zeropoint definition, which has to be done in advance. However, this calibration process leads to some problems since the observing conditions of two nights are never the same and the zeropoint might vary. Using this method requires perfect photometric conditions during the measurement or subsequent corrections to be applied.

**Differential Photometry** uses a reference object in the field to calculate another objects magnitude. The magnitudes  $m_\star, m_{\text{ref}}$  of the two objects are correlated with referring fluxes  $F_\star, F_{\text{ref}}$  through

$$m_\star - m_{\text{ref}} = -2.5 \log_{10} \frac{F_\star}{F_{\text{ref}}} \quad (2.2)$$

The advantage of this method compared to absolute photometry is that both objects underly the same observational conditions. Therefore, no corrections have to be applied which makes this method less vulnerable to varying observing conditions. However, at least one reference object has to be in the same field-of-view, of which the magnitude has to be known.

Since differential photometry is the method used in this work, all following explanations and equations will be subject to this.

### 2.3.2 Signal-to-Noise Ratio and Errors

The Signal-to-Noise ratio (S/N ratio) is a measure of how good a signal is measured against background noise. It is defined as the quotient of signal strength and noise. In astronomy, the signal strength refers to the object's flux and the noise consists of several terms which contribute to the total noise of the image. A usual definition of the S/N ratio is given by equation 2.3.

$$\frac{S}{N} = \frac{S}{\sqrt{S + n_{\text{obj}}(N_{\text{sky}} + N_{\text{dark}} + N_{\text{read}}^2)}} \quad (2.3)$$

Herein,  $S$  denotes the collected object flux over the integration time within an area consisting of  $n_{\text{obj}}$  pixels, e.g. using aperture photometry. It appears in the numerator as signal strength. The noise term in the denominator is expressed as the square-root of a quadratic summation of single noise terms, which are in detail:



- $\sqrt{S} = \sigma_{\text{photon}}$  **photon shot noise**; Flux measurements underlie Poisson statistics, therefore the statistical error of the flux  $S$  itself is expressed by  $\sqrt{S}$ .
- $\sqrt{n_{\text{obj}}N_{\text{sky}}} = \sigma_{\text{sky}}$  **sky background noise**; The sky background has a brightness of its own due to airglow or scattering of ambient light on air particles. Sky background illumination is subtracted from the total integrated flux of the object as part of the analysis process (cf. 6.1). However, the background illumination underlies Poisson statistics as well. Therefore, the statistical error of the background illumination is the square-root of the total background flux, which is the product of the number of pixels involved  $n_{\text{obj}}$  and the total number of photons per pixel from the background  $N_{\text{sky}}$ .
- $\sqrt{n_{\text{obj}}N_{\text{dark}}} = \sigma_{\text{dark}}$  **dark current noise**; Dark current means the generation of a detector signal due to thermal excitation (cf. 2.2.2). Dark noise also follows Poisson statistics. The value  $N_{\text{dark}}$  describes the total number of generated dark current electrons per pixel during integration time.
- $\sqrt{n_{\text{obj}}N_{\text{read}}}$  **readout noise**; This type of noise is not subject to Poisson statistics. Hence, the total number of electrons per pixel resulting from read noise  $N_{\text{read}}$  enters the equation not as a square-root. Read noise describes statistical variations during the readout process.

Other noise sources like digitization noise might be considered, but lead to small deviations only. This and further topics are discussed in [How06].

In the case of observing a bright object, the photon noise term overweights all other noise terms. Hence, the according terms in Eq. 2.3 can be neglected leading to

$$\frac{S}{N} = \frac{S}{\sigma_{\text{signal}}} = \frac{S}{\sqrt{S}} = \sqrt{S} \quad (2.4)$$

yielding the result for a measurement of a single Poisson behaved value.

Eq. 2.3 provides a theoretical approach to calculate the Signal-to-Noise ratio. In this work, a software routine of the IRAF package is used to estimate the total noise  $\sigma_{\text{total}}$  in an image which is then used to calculate the S/N ratio. This approach is believed to give the best results, since this kind of measurement may contain noise terms which are unregarded in the theoretical approach. The S/N ratio is then calculated using the simpler equation 2.5.

$$\frac{S}{N} = \frac{S}{\sqrt{S + \sigma_{\text{total}}^2}} \quad (2.5)$$

### Error of the Magnitude

The error of the brightness magnitude is obtained using Gaussian error propagation on Eq. 2.2. One gets a standard deviation  $\sigma_{\star}$  for the object with flux  $F_{\star}$  using a reference object with flux  $F_{\text{ref}}$ , magnitude  $m_{\text{ref}}$  and according standard deviation  $\sigma_{\text{ref}}$  expressed by

$$\begin{aligned}
\sigma_{\star} = \Delta m_{\star} &= \sqrt{\left(\frac{\partial m_{\star}}{\partial m_{\text{ref}}} \cdot \sigma_{\text{ref}}\right)^2 + \left(\frac{\partial m_{\star}}{\partial F_{\star}} \cdot \Delta F_{\star}\right)^2 + \left(\frac{\partial m_{\star}}{\partial F_{\text{ref}}} \cdot \Delta F_{\text{ref}}\right)^2} \\
&= \sqrt{\sigma_{\text{ref}}^2 + \left(-\frac{2.5}{\ln 10} \frac{1}{\sqrt{F_{\star}}}\right)^2 + \left(\frac{2.5}{\ln 10} \frac{1}{\sqrt{F_{\text{ref}}}}\right)^2} \\
&= \sqrt{\sigma_{\text{ref}}^2 + \left(-1.085736 \cdot \frac{1}{S/N_{\star}}\right)^2 + \left(1.085736 \cdot \frac{1}{S/N_{\text{ref}}}\right)^2}
\end{aligned} \tag{2.6}$$

Stepping from line one to line two one uses the fact that  $\Delta F = \sqrt{F}$  which expresses the Poisson behaviour of the flux. The transition to the final line uses the expression of the standard deviation of the flux ( $\sigma = \sqrt{F}$ ) using the Signal-to-Noise ratio

$$\frac{1}{\sqrt{F}} = \frac{F}{\sqrt{F}} = \frac{1}{S/N}$$

This is possible, since the total noise is dominated by photon noise for all measurements.

As a result of Eq. 2.6 one receives a relation which only depends on the Signal-to-Noise ratios of the object (displayed by a star) and the reference objects used for comparison. If more than one reference object was used for calibration, one term for each object appears under the square-root. The resulting error includes all uncertainties, i.e. the magnitudal errors of the reference objects ( $\sigma_{\text{ref}}$ ) as well. It therefore represents a *total error of the photometric measurement*.

To have a measure for the quality of the measurement, one can use the *instrumental error of the photometric measurement*. This is defined equally to Eq. 2.6 but disregards the magnitudal error of the reference objects, i.e.  $\sigma_{\text{ref}} = 0$ . This error is usually of the order of  $10^{-3}$  or even smaller and therefore underestimates the real error of the measurement. However, it is useful as a quality estimator.

### 2.3.3 Airmass

When taking astronomical measurements using ground-based telescopes one has to regard the optical path length of the light through Earth's atmosphere. Light passing the atmosphere gets attenuated by scattering and absorption effects. The longer the optical path length, the greater the attenuation. Therefore, sky objects near the horizon appear to be less bright than in the zenith. There are numerous models to mathematically describe atmospheric extinction. They are described in according literature of observational astronomy. In this case, it is sufficient to know that the *airmass* parameter is a function of an objects elevation. Hence, an object's airmass parameter changes over the time. The airmass value of an image is usually provided by the FITS header.

Since a polarimetric measurement consists of several images, which are taken successively, the airmass parameter of an object might vary during one measurement. Therefore, fluxes have to be corrected for this. Otherwise, polarimetric measurements underlie a systematic error.

Atmospheric extinction is described as an additive component of the apparent magnitude

$$m(\lambda, z) = m_0(\lambda) + \kappa(\lambda) \cdot X(z)$$

with the wavelength  $\lambda$ , the extinction coefficient  $\kappa(\lambda)$  and the airmass  $X$  depending on the elevation  $z$ . Together with Eq. 2.2 one gets a correction factor for fluxes of

$$\frac{F(z)}{F_0} = 10^{0.4 \cdot \kappa \cdot X(z)} \quad (2.7)$$

$\kappa$  is usually wavelength dependent and empiric (cf. 3.1.1).

## 2.4 Polarimetry

### 2.4.1 Polarization Basics

#### Definition

Light is an electromagnetic wave, i.e. it consists of an electric  $\vec{E}$  and a magnetic  $\vec{B}$  field vector which oscillate perpendicular to the direction of propagation  $\vec{k}$ . Both vectors are coupled in a self-preservative way. Comparable to a RLC circuit, the intrinsic energy oscillates between the electric and magnetic field leading to a harmonic oscillation. One can derive the wave equation describing this process easily from Maxwell's Equations, which also lead to the alignment of the waves:

$$\vec{k} = \vec{E} \times \vec{B} \quad (\text{in natural units})$$

Hence, the electric field vector oscillates in a plane perpendicular to that of the magnetic field vector. Both planes are aligned perpendicular to the direction of propagation. Hence, the wave is completely described either the plane of the electric or magnetic field vector is known. In order to prevent confusion, the plane of the electric field vector is defined to describe the *polarization plane* of the wave. The angle between the polarization plane and an arbitrary predefined plane, which is also aligned perpendicular to the propagation direction, is referred as *polarization angle*.

Most sources of electromagnetic radiation contain a large number of atoms or molecules that emit light. These emitters usually have no preferred alignment and point in arbitrary directions. Therefore, the emitting light is *unpolarized*, since all polarization angles appear with the same probability. If all emitters are aligned parallel, the light is *fully polarized*. If there is only a partial correlation between the alignment of the emitters, the light is *partially polarized*. This can be described as a superposition of a completely unpolarized component, and a completely polarized one. The fraction of the amount of polarized and unpolarized light defines the *polarization degree*.

#### Polarization states

Since waves obey the principle of superposition, one may arbitrarily divide the electric field vector into two perpendicular components, named  $\vec{E}_x$  and  $\vec{E}_y$  for instance.

As illustrated in Fig. 2.8, the superposition of both waves  $E_x(\vec{x}, t)$  and  $E_y(\vec{x}, t)$  (represented by the red and blue wave) leads to a resulting wave (black). The shape of the resulting wave in the xy-plane (which is perpendicular to  $\vec{k}$ ) depends on the phase shift of both  $E_x$  and  $E_y$ . If both waves are not shifted at all, the resulting wave oscillates along a line, i.e. the light is *linear polarized* (Fig. 2.8.(i)). If the phase shift is exactly  $90^\circ$ , the resulting wave describes a circle, the light is *circular polarized* (Fig. 2.8.(iii)). For all other phase shift values the polarization of the resulting

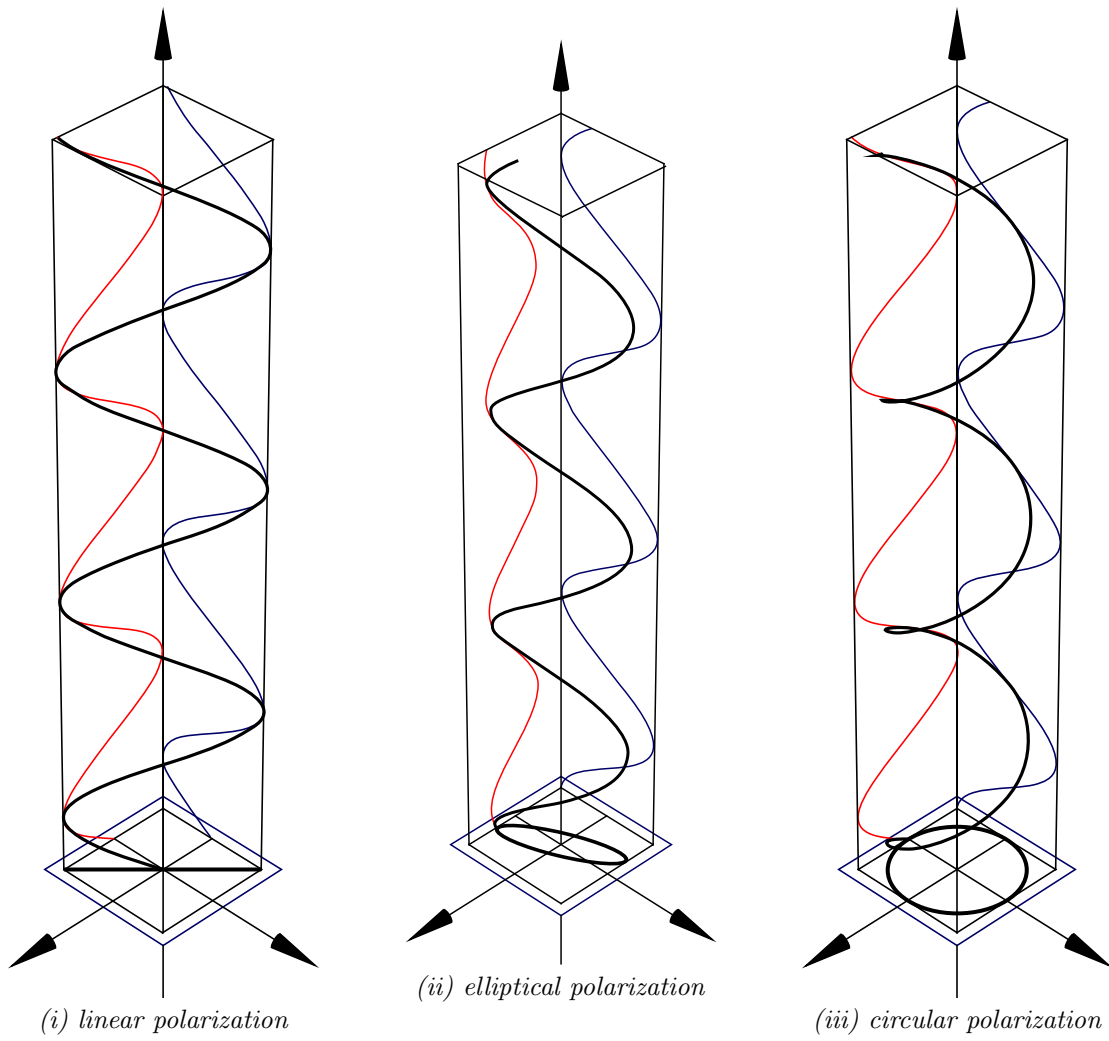


Figure 2.8: Illustration of different polarization states

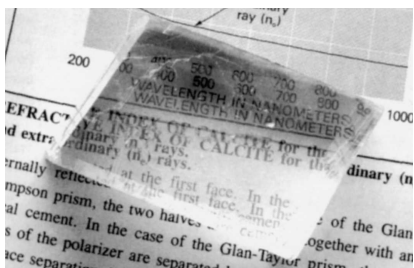


Figure 2.9: Calcite crystal displaying birefringence (taken from [Dem06])

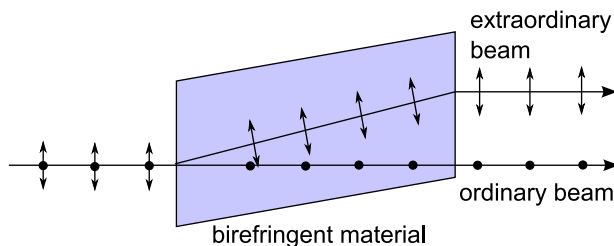


Figure 2.10: Illustration of birefringence

wave is called *elliptical* (Fig. 2.8.(ii)). This general type of polarization state can be described as a superposition of both, linear and circular polarization.

The polarization state of a light wave can be changed using polarization analyzers, which usually are made of *calcite* or another *birefringent material*. Such crystalline materials have the feature to decomposit an unpolarized ray of light in two beams, called the *ordinary* and the *extraordinary* beam, which are polarized perpendicular to each other. The ordinary beam follows *Snell's law*, whereas the extraordinary beam shows an exit angle  $\neq 0$  even for an entrance angle parallel to the plane's normal vector. This leads to double refracted transmission (Fig. 2.9). The origin of this behaviour is the anisotropy of the material's crystal structure leading to different refraction indices for beams of different polarization angles. A more detailed explanation can be found in [Dem06].

Obviously, birefringent material can be used to linearly polarize a beam of light. The anisotropic refraction indices however may be used to start a rotation of the electric field vector (in the  $xy$ -plane, cf. Fig. 2.8) and lead to circular polarization. This is achieved using so called *retarder plates* which lead to a phase shift between the two polarization directions.

As part of this thesis only linear polarization of the incoming light is examined. Therefore, the focus will lie on this polarization state.

## 2.4.2 Mathematical Description of Polarization

### Polarization ellipse

The polarization behaviour of a light beam is completely described by parameterizing the polarization ellipse (which becomes a straight line in case of linear polarized light or circular in case of circular polarized light). An illustration can be found in Fig. 2.11.

The polarization angle  $\chi$  describes the spatial orientation of the ellipse in respect to a predefined plane (in Fig. 2.11 represented by the  $x$ -axis). The value  $\tan \beta$  represents the ratio of the two major axis of the ellipse and  $a$  is a measure of the intensity of the electric field vector.

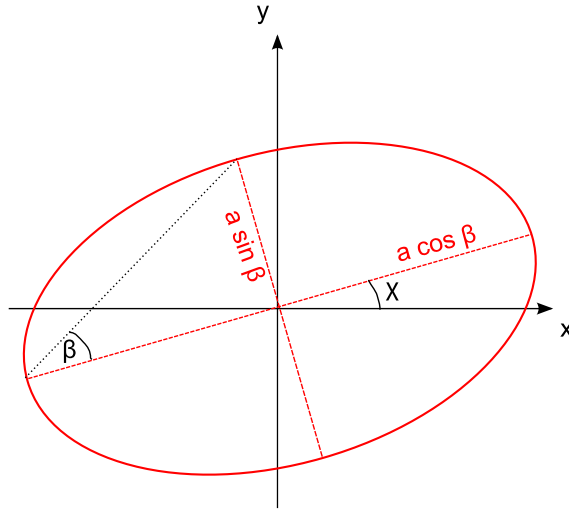


Figure 2.11: Illustration of the polarization ellipse ( $\chi$  = polarization angle,  $\tan \beta$  = axial ratio of ellipse)

### Stokes parameters

In order to simplify this description, George Gabriel Stokes introduced in 1852 his own set of parameters. The Stokes parameters are often combined into a vector, known as the *Stokes vector*:

$$\vec{S} = \begin{pmatrix} I \\ Q \\ U \\ V \end{pmatrix} = \begin{pmatrix} a^2 \\ a^2 \cos 2\beta \cos 2\chi \\ a^2 \cos 2\beta \cos 2\chi \\ a^2 \sin 2\beta \end{pmatrix} \quad (2.8)$$

Note that  $I \geq 0$ , but  $Q$ ,  $U$  and  $V$  may be positive or negative. Another important relation is:

$$I^2 \geq Q^2 + U^2 + V^2$$

whereas equality is only true for total polarization, i.e. a polarization degree of 1.

The Stokes parameters can therefore be interpreted as:

**I** total intensity of the light beam

**Q** horizontally/vertically polarized fraction of light

**U** diagonally polarized fraction of light

**V** right-handed/left-handed circular polarized fraction of light

Hence, an arbitrary ray of light can be completely described using Stokes parameters, even if the light is only partially polarized. For further readings please confer [Tin96].

Since only linear polarization of light is of interest in the context of this thesis, the Stokes parameter  $V$  equals 0 for the rest of this work.

### 2.4.3 Application of Polarimetry in this Thesis

In order to obtain the Stokes parameters of an object, at least four images have to be taken using a *polarimeter* in the optical path of the telescope. The polarimeter contains a *polarization analyzer* (i.e. a birefringent element) allowing only linear polarized light to pass. Hence, one measures the object's intensity of one specific polarization angle. In order to measure the polarization degree and polarization angle of the object, the polarization analyzer is rotatable. To measure the wanted values, one has to take four images using different alignments of the polarization analyzer, covering at least an angular region of  $90^\circ$ . This provides a complete set of information to calculate the Stokes parameters. The relevant equations are taken from [Hea] following:

$$\begin{aligned}
 I &= I_0 + I_{45} + I_{90} + I_{135} \\
 Q &= \frac{I_0 - I_{90}}{I_0 + I_{90}} \cdot I \\
 U &= \frac{I_{45} - I_{135}}{I_{45} + I_{135}} \cdot I
 \end{aligned} \tag{2.9}$$

(For convenience the angular positions of the polarimeter used in the project have been used already)

From this, one can calculate the polarization angle and polarization degree:

$$\begin{aligned}
 P &= \frac{\sqrt{Q^2 + U^2}}{I} \\
 \Theta &= \frac{1}{2} \arctan \frac{U}{Q}
 \end{aligned} \tag{2.10}$$

#### Errors

The errors of the polarization degree and angle follow from equations 2.9 to 2.10 using gaussian error propagation. One gets

$$\begin{aligned}
 \Delta P &= \sqrt{\left(\frac{Q}{I\sqrt{Q^2 + U^2}} \cdot \Delta Q\right)^2 + \left(\frac{U}{I\sqrt{Q^2 + U^2}} \cdot \Delta U\right)^2 + \left(\frac{\sqrt{Q^2 + U^2}}{I^2} \cdot \Delta I\right)^2} \\
 \Delta \Theta &= \sqrt{\left(\frac{1}{Q[1 + (U/Q)^2]} \cdot \Delta U\right)^2 + \left(\frac{U}{Q^2[1 + (U/Q)^2]} \cdot \Delta Q\right)^2}
 \end{aligned} \tag{2.11}$$

with the errors of the Stokes parameter being

$$\begin{aligned}
\Delta I &= \sqrt{\Delta I_0^2 + \Delta I_{45}^2 + \Delta I_{90}^2 + \Delta I_{135}^2} \\
\Delta U &= \left[ \left( \frac{1}{I_{45} + I_{135}} \left( 1 - \frac{U}{I} \right) \cdot I + \frac{U}{I} \right)^2 \cdot \Delta I_{45}^2 + \left( \frac{U}{I} \right)^2 \cdot \Delta I_0^2 \right. \\
&\quad \left. + \left( \frac{-1}{I_{45} + I_{135}} \left( 1 + \frac{U}{I} \right) \cdot I + \frac{U}{I} \right)^2 \cdot \Delta I_{135}^2 + \left( \frac{U}{I} \right)^2 \cdot \Delta I_{90}^2 \right]^{\frac{1}{2}} \\
\Delta Q &= \left[ \left( \frac{1}{I_0 + I_{90}} \left( 1 - \frac{Q}{I} \right) \cdot I + \frac{Q}{I} \right)^2 \cdot \Delta I_0^2 + \left( \frac{Q}{I} \right)^2 \cdot \Delta I_{45}^2 \right. \\
&\quad \left. + \left( \frac{-1}{I_0 + I_{90}} \left( 1 + \frac{Q}{I} \right) \cdot I + \frac{Q}{I} \right)^2 \cdot \Delta I_{90}^2 + \left( \frac{Q}{I} \right)^2 \cdot \Delta I_{135}^2 \right]^{\frac{1}{2}}
\end{aligned} \tag{2.12}$$

## 2.5 Polarization in Astronomy

Polarimetry is highly valuable in astronomy since astronomers have to stick on observational information. Experiments on Earth help to find the origins of polarized light. These results now have to help to understand observations and transfer the results found in laboratories to understand the processes leading to observed phenomena.

Wherever there is appreciable asymmetry in an astronomical situation, there is likely to be polarization at some level. The main asymmetries giving rise to astronomical polarization are magnetic fields and an asymmetric distribution of scattered radiation. Some example are given below [Tin96]:

- The longitudinal Zeeman effect has been used extensively to analyze the strong magnetic fields of  $A_p$  stars.
- Some white dwarfs have been found to have magnetic fields so strong that the Zeeman effect can be detected even in very wide features in the optical spectrum.
- The magnetic field configuration and radiation mechanism of pulsars have been studied in great detail by measuring the polarization during the radio pulses.
- In the radio domain, *Faraday rotation* of the plane of polarization is used to estimate the strength of the longitudinal field component in the region between source and observer.

The most important phenomenon in the context of this thesis is the *synchrotron radiation* emitted from a wide range of objects including many types of AGN and blazars as well.

### 2.5.1 Synchrotron Emission

If electrons are accelerated to high energies in the GeV-range (highly relativistic regime) and move inside a magnetic field they describe a circular trajectory if the Lorentz force equals the centrifugal



force. Along their track, they emit radiation due to the continuous acceleration towards the center of the circular trajectory. The emission is of non-thermal nature and follows a power law. The spectral emission reaches from the radio to the  $\gamma$ -ray regime in the case of extremely high electron energies.

Due to the parallel motion of the electrons in the magnetic field, synchrotron emission is highly polarized with polarization degrees of up to 60% maximum.



## Chapter 3

# Data Acquisition

Image data used in this thesis were obtained at *Observatorio Astronómico Nacional* at San Pedro Martir, Mexico. A 0.84m Ritchey-Chrétien telescope was used for this purpose. To receive polarimetric information a rotating polaroid foil was installed in the telescope's light path - the POLIMA instrument.

*In this chapter the observatory and the telescope are introduced first. Later, the data acquisition process is presented.*

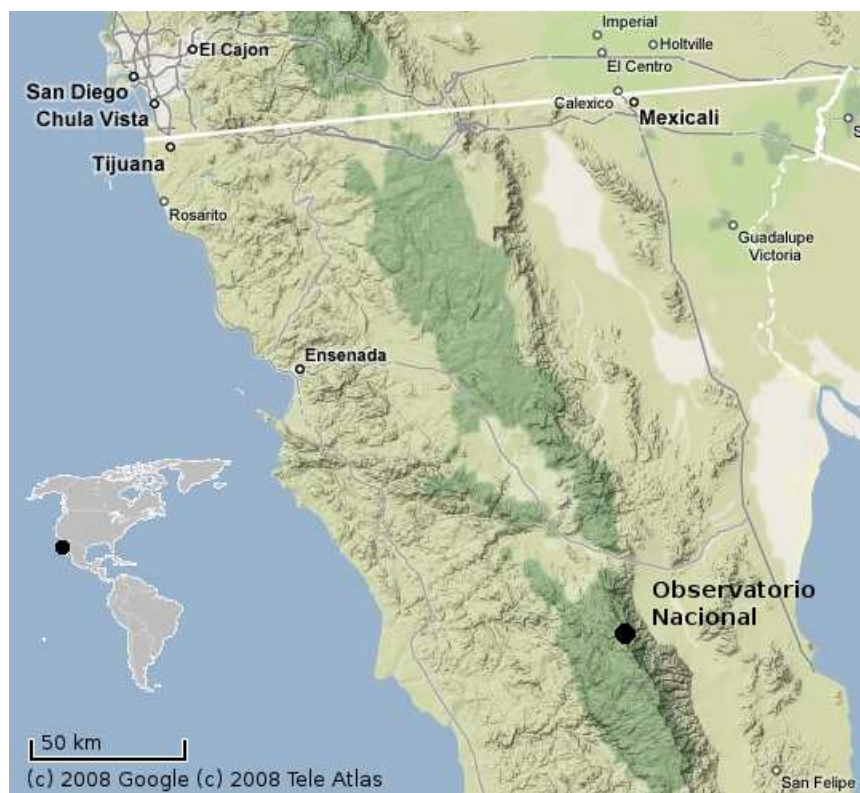


Figure 3.1: Observatory location in Baja California

## 3.1 Observatory

### 3.1.1 Observatory Site

The National Observatory of Mexico (*Observatorio Astronómico Nacional*) is located in the *Sierra de San Pedro Mártir* National Park. This is at the top of a spur arising from San Felipe Desert in the northern part of the Baja California peninsula. The observatory site is located at an elevation of approximately 2800 m above sea level. The nearest bigger cities are Ensenada in the northwest (140 km), Mexicali in the northeast (180 km) and San Felipe in the southeast (100 km).

The National Observatory was founded in 1878 and was first erected in Mexico City. Due to increasing light and air pollution it was moved to today's site in the year 1967. Today it consists of a main building surrounded by some bungalows and the domes which are located a few kilometers from these buildings to limit light pollution. Three telescopes are in use:

- 1.5 m Ritchey-Chrétien:  $f/13.5$ , installed in 1970, used for direct imaging, optical spectroscopy and photometry
- 0.84 m Ritchey-Chrétien:  $f/15$ , installed in 1972, used for direct imaging, optical spectroscopy and photometry
- 2.12 m Ritchey-Chrétien:  $f/7.5$ ,  $f/13.5$ ,  $f/35$  built between 1974 and 1979, used for direct imaging and optical spectroscopy

The telescopes can be equipped with a set of filter wheels, analyzers and CCD detectors. That allows using the telescopes for a variety of applications.

The Observatory is administered by the Astronomical Institute of the National Autonomous University of Mexico (*Universidad Nacional Autonomico de Mexico*, UNAM) which is located in Ensenada. The institute was established in 1974, with the purpose of supporting the activities at the observatory, which can be accessed using a shuttle service from there.

### Climate and Airmass

The Sierra de San Pedro Martir is one of the three best cloud-free areas in the world which marks the location as an excellent observatory site. Furthermore, it is characterized as a site with low water vapor and an excellent image sharpness. Testing revealed a median seeing of  $0.61 \text{ arcsec}$ , showing some seasonal dependence. [Eea98]

Examinations by Schuster and Parrao [SP01] show that average extinction at SPM, excluding the effects of volcanic outbursts, does not seem to have changed significantly over a period of more than 20 years. They derived a mean extinction coefficient for red light ( $630 \text{ nm}$ ) of  $\kappa(630 \text{ nm}) = 0.1$ .

### 3.1.2 The 0.84m Telescope

Most of the images in this thesis were taken with the 0.84m telescope. This is a Ritchey-Chrétien-type telescope with an 84cm primary mirror. It delivers a roughly  $f/15$  beam to a Cassegrain focus where scientific instruments are mounted. Experience of other observers show, that telescope optics often suffers from astigmatism. The telescope has an equatorial mount. Its pointing is limited to declinations between  $+80$  and  $-45$  degrees and hour angles between  $+5$  and  $-5$  hours. The



Figure 3.2: 0.84m telescope building



Figure 3.3: telescope equipment

telescope may have problems pointing at the northern and southern extremes of declination if it is not well balanced.

The guider hardware consists of an intensified CCD camera and an inclined plane mirror. The camera is mounted on a carriage, providing control of the focus and field of view movement. Guiding stars can be selected automatically from the HST Guide Star Catalog which requires an accurate telescope pointing. For reliable guiding, stars should have a brightness of at least 12 mag. Due to reflections on the guiding system carriage, ghost images might appear on the image if the guider camera is placed in the northern half of the field. [Wat01]

The usual setup of the 84cm telescope consists of:

- MEXMAN filter wheel, all images were taken using R filter ( $\approx 640$  nm)
- POLIMA polarization analyzer wheel, cf. subsection 3.1.3
- MARCONI CCD detector, cf. subsection 3.1.4

Additionally, the telescope is equipped with a video camera attached to the finder scope to simplify the pointing and positioning process. Telescope positioning and focus control is computer controlled.

Since April 2009, the telescope dome can be opened and closed automatically using the telescope software.

### 3.1.3 POLIMA Filter Wheel (Polarimeter)

The POLIMA filter wheel (*Polarímetro óptico de imagen*) is a direct imaging polarimeter that has been developed at the *Instituto de Astronomía, UNAM*. After entering the metal boxing of the polarimeter, the light ray cross section diameter is limited by an aperture. Until this point the light is polychromatic and of random polarization. Passing the polarization analyzer, only light beams of a specific linear polarization remain. Since the beam is still polychromatic, a color filter limits the spectral distribution. Therefore, the light beam leaving the polarimeter and hitting the

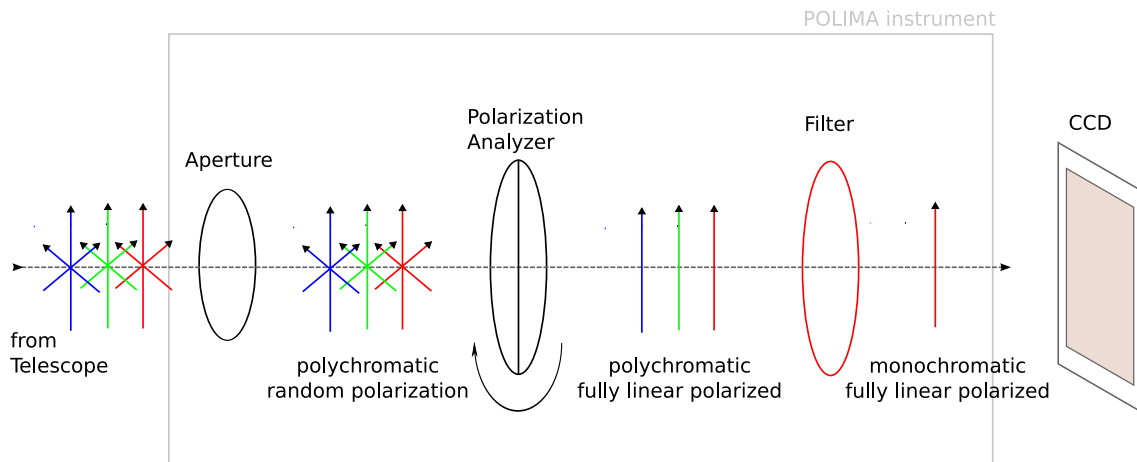


Figure 3.4: Illustration of light characteristics in POLIMA

CCD is monochromatic and linear polarized. This is illustrated in Fig. 3.4.

The polarization analyzer used in the POLIMA instrument is a *Glan-Taylor prism*, which is made of two right-angled prisms of calcite that are separated on their long faces with an air gap. The prism is designed in a way to have a fully polarized transmitting beam. In order to perform polarimetric measurements, the polarimeter is designed to be rotatable around the optical axis. The rotational angle is later referred to as *polarimeter angle* or similar.

The POLIMA instrument's prism specifications show a transmittance of 90 % and a field of view of  $\pm 4$  degrees. Together with the 0.84m telescope, this leads to a unobscured field of view of  $3 \times 3$  arcminutes in the sky plane. [Hea]

Due to the limited geometrical diameter of the calcite element, not the complete field of view of the CCD is illuminated and therefore usable. The unobscured field of view can approximately be described as a square field (Fig. 3.5). Using the MARCONI detector, its edge length is approximately 550 pixels. Since the prism can be rotated but the sky background alignment is fixed, the usable field all four polarization angles have in common is smaller than this field. This is illustrated in Fig. 3.5 and 3.6.

As one can see, the unobscured field of the combined images forms a octagonal area, which can in approximation be described by a circle. To perform polarimetric measurements, the source of interest has to be present in the bounds of this circle in each image. Otherwise the polarization information is incomplete and the determination of the polarization angle and degree is impossible.

### 3.1.4 CCD Detectors

A number of Charge Coupled Devices (CCDs) are available at OAN-SPM. In order to keep images comparable, the technical support team of the telescope is advised to attach the same detector to the telescope, which is the MARCONI detector. Due to technical or organizational problems it is inevitable to have other cameras attached to the telescope. Since now, two other detectors were used: a THOMSON 2k (CCD2000) and a SITE 1. Table 3.1 shows some important detector characteristics.

All detectors are cooled using liquid nitrogen, which is filled in some hours in advance of the

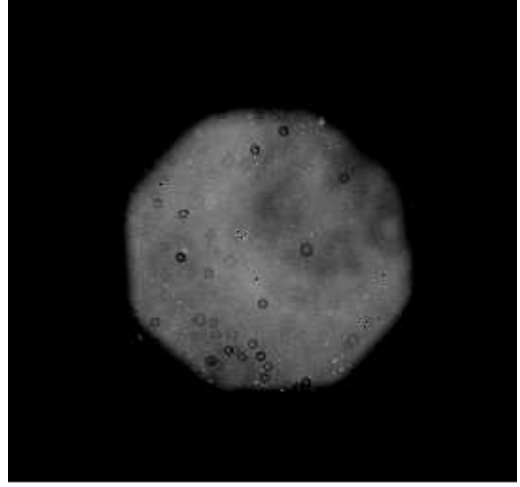
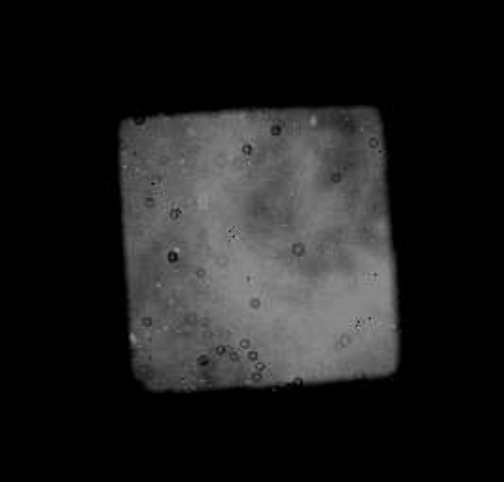


Figure 3.5: MARCONI flatfield, 0 degree polarization angle  
 Figure 3.6: combination of MARCONI flatfields of different alignment

observation by the technical staff to guarantee a stable and low temperature during operation.

## 3.2 Image Acquisition

The image acquisition process is completely controlled via a graphical user interface. The software allows macro definitions to simplify and speed up the imaging process. Such macros exist for bias and flatfield images as well as for object exposures. The latter means an automated sequence of exposures with different polarization analyzer angles.

In order to collect a maximum number of objects per night, binning mode  $2 \times 2$  is used to increase the efficient pixel size and therefore decrease the integration and read-out time. Furthermore the maximum integration time is limited to 600 s per image. To save setup time, the autoguider is only used for images with an integration time longer or as long as 180 s.

To make sure that enough correction images are available for the image reduction process, flatfield

Table 3.1: CCD characteristics [Wea04]

	MARCONI	THOMSON 2k	SITe 1
CCD chip	e2vm E2V-4240	Thomson TH7398M CCD	Site SI003
pixel array	$2174 \times 2048$	$2048 \times 2048$	$1024 \times 1024$
pixel size [ $\mu m$ ]	13.5	14	24
used binning mode	$2 \times 2$	$2 \times 2$	$2 \times 2$
gain [ $e^-/ADU$ ]	1.73 @ binning 2	1.97 @ binning 2	4.97 @ binning 2
readout noise [ $e^-$ ]	5.3	6.8	12.7
operating temperature [ $^{\circ}C$ ]	-120	-93	-88 to -84
dark current [ $e^-/h$ ]	-	-	8.1

and bias images are taken both at dusk and dawn. During the flatfielding, the telescope should point to the east during dusk and to the west during dawn, respectively. This is to avoid problems with sky polarization. Furthermore, the integration time for flatfields must not be shorter than 5 s to prevent shutter effects on the image.

Until the observing run of April 2009 the observing strategy offered two macros for scientific object integration, which are

**full cycle** a series of 8 exposures with different polarization angles of 0, 45, 90, 135, 135, 90, 45 and 0°

**half cycle** a series of 4 exposures with different polarization angles of 0, 45, 90 and 135°

The former macro was used for bright targets, the latter for faint ones.

This definition was replaced in April 2009 in order to improve image quality and quantity. The idea is to only use half cycle sequences for objects to save observing time and therefore increase the number of objects imaged in one night. Furthermore, image quality is improved by switching the angle sequence to 0, 90, 45 and 135°. As can be seen in Eq. 2.9 and 2.10 the images belonging to polarimeter angles of 0° and 90° determine the Stokes parameter  $Q$  and 45° and 135° do so for  $U$ . Since variations of the observing conditions lead to flux variations affecting the measurement, images needed to the same Stokes parameter have to be taken successively to minimize variations. Observing conditions are influenced by the sky coverage (clouds or cirrus) and the sky transparency. The impact of flux variations is estimated in 9.1 for the example of incorrect dome tracking.

The sky quality of each measurement (i.e. set of four images) can be estimated by comparing the comparison star fluxes in the four images. Since there are no comparison stars defined in standard star fields, there are still two successive measurement mandatory. Due to the short integration time for such objects, this does not affect other observations.



## Chapter 4

# Data Processing - the Polima pipeline

The main objective of this thesis was the design of a pipeline for automatized image reduction and analysis as far as technically possible. The software ought to be based on the IRAF software package, which is used by most participants of the SPM project.

*The following section gives an introduction to the IRAF software package, the main goals and features of the `polima` pipeline and an overview of the `polima` package.*

### 4.1 IRAF

Most functions of the `polima` pipeline are based on the *IRAF*<sup>1</sup> (*Image Reduction and Analysis Facility*) software packages. IRAF is written and supported by the IRAF programming group at the *National Optical Astronomy Observatories* (NOAO) in Tucson, Arizona. The software provides routines for the reduction and analysis of astronomical data and is available for all major operating systems.

IRAF uses the *SAOImage DS9*<sup>2</sup> software for image display.

IRAF commands (tasks) are organized into package structures. Additional packages for many different applications are available and can be installed. IRAF offers the opportunity to create user-defined tasks and bundle them in packages. This has been done for the `polima` pipeline. The term 'polima package' refers to all tasks, which have been created by the author. The package can be downloaded from the internal section of the SPM homepage<sup>3</sup>.

In order to prevent confusions, terms in context with IRAF or the `polima` package are highlighted using **typewriter letters**. Furthermore, FITS header descriptors are displayed in *italic letters*.

---

<sup>1</sup><http://iraf.noao.edu/>

<sup>2</sup><http://hea-www.harvard.edu/RD/ds9/>

<sup>3</sup><http://www.lsw.uni-heidelberg.de/users/jheidt/spm/intern/polima/polima.html>

### 4.1.1 Additional Software

#### IMWCS

The `polima` pipeline uses the standalone software routine *IMWCS*<sup>4</sup> which is part of the *WC-STOOLS*<sup>5</sup> package maintained by Douglas Mink from the *Smithsonian Astrophysical Observatory Telescope Data Center*. This routine is a utility for setting the *world coordinate system* (*WCS*) of a FITS image. The *WCS* is the relationship between sky coordinates and image pixels and can be described in a standard way in the header of an image.

*IMWCS* identifies a sky field by matching an object catalog extracted from an image with an existing catalog. In this work, the *USNO-A2.0*<sup>6</sup> catalog is used, since it provides a large number of faint stars. *WCS* data are written in the FITS header and allow a conversion of sky coordinates (right ascension and declination) to image coordinates (*x* and *y*).

#### Identification Scripts

The *identification scripts* are standalone shell scripts which are creating coordinate and reference-magnitude files from images. One script exists for each object of the target list. The scripts are located in the *identify* subdirectory of the `polima` directory.

The setup is explained using the identification script for the object 3C 273:

```
1: #!/bin/bash -x
2:
3: # $1 = FITS file
4:
5: #source
6: sky2xy -n 1 -o x $1 12:29:06.79 +02:03:06.0 >> $1_x.coords
7: sky2xy -n 1 -o y $1 12:29:06.79 +02:03:06.0 >> $1_y.coords
8: echo -e "src\t0\t0" >> $1_ref.mag
9:
10:
11: # comparison star E
12: sky2xy -n 1 -o x $1 12:29:08.42 +02:00:18.4 >> $1_x.coords
13: sky2xy -n 1 -o y $1 12:29:08.42 +02:00:18.4 >> $1_y.coords
14: echo -e "E\t12.27\t0.05" >> $1_ref.mag
15:
16: # comparison star G
17: sky2xy -n 1 -o x $1 12:29:03.23 +02:03:18.0 >> $1_x.coords
18: sky2xy -n 1 -o y $1 12:29:03.23 +02:03:18.0 >> $1_y.coords
19: echo -e "G\t13.16\t0.05" >> $1_ref.mag
20:
21:
```

<sup>4</sup><http://tdc-www.harvard.edu/wcstools/imwcs/>

<sup>5</sup><http://tdc-www.harvard.edu/software/wcstools/wcsprogs.html>

<sup>6</sup><http://tdc-www.harvard.edu/catalogs/ua2.html>

---

```

22: # merge coordinate and magnitude tables to filter off image stars
23: paste -d "\t" $1_x.coords $1_y.coords > aux1
24: paste -d "\t" aux1 $1_ref.mag | grep -Ev 'off' > aux2
25:
26: # split table into coordinate and magnitude table again
27: awk '{print $1"\t"$2}' aux2 > $1.coo
28: awk '{print $3"\t"$4"\t"$5}' aux2 > $1_ref.mag
29:
30: rm $1_x.coords $1_y.coords aux1 aux2

```

The first line chooses 'bash' as interpreter for this file. The variable '\$1' designates the filename of the FITS image which is handed over via command line argument. The following three blocks obtain the image coordinates the objects expected. One block covers one one object, each. The approach is explained using one block as an example.

Each script uses the routine *SKY2XY*<sup>7</sup> which is part of the *WCSTOOLS* package, too. It is used twice for each object. The task receives a FITS image carrying WCS information and a set of sky coordinates and outputs the according image coordinates. The option '-n 1' means to give the accuracy of the output coordinates on one decimal place. Using '-o x' and '-o y' give the x and y-coordinate, respectively. Each coordinate is written to a file. If an object does not appear on the image, the term 'off image' is printed in the file. Line 8 (14 and 19, too) writes the source's name, magnitude and magnitude error into another file (cf. 5.3.1).

Lines 23 merges the two files carrying the x and y-coordinate into one file with two columns. This file is again merged with the magnitude file in line 24. But this time only lines are merged, which do not carry the term 'off' as in 'off image'. Thus, only objects that really appear on the image also appear in the file. Lines 27 and 28 split the resulting file again into one coordinate and one reference-mag-file. The last line removes all auxiliary files.

The routine is robust and leads to good positional precision if WCS identification succeeded.

## 4.2 Goals and Features of the Pipeline

### 4.2.1 Goals

The primary goal of the pipeline is the development of an automated image reduction routine. The idea is to be able to reduce the data of one observing run or a single night in short time and make the reduced data accessible to other team members for analysis.

In the beginning, further routines for image analysis, meaning photometry and polarimetry, were eligible but a realization was depending on the possibility of automatic object identification in each image. However, the development of routines to simplify the image analysis were aimed.

### 4.2.2 Main Features

The latest version of the *polima* package includes the following features:

---

<sup>7</sup><http://tdc-www.harvard.edu/wcstools/sky2xy.html>

- complete image reduction
- automatic WCS identification/brightest object detection for each image
- automated photometry task
- automated polarimetry task
- a number of auxiliary tasks to simplify image handling
- complete set of help files

Each task of the package is introduced and explained in detail in the following three chapters.

## 4.3 The polima package

The complete software package is available as 'tar.gz'-file from the project homepage<sup>8</sup>.

### 4.3.1 Content

The archive file contains the following files and directory: (listed after appearance in directories)

```
checkcoo.cl    cpcoo.cl          identify (dir)  polima.cl      popol.cl
chimagetyp.cl doc (dir)         lib (dir)      polima.hd      README
chobject.cl   dophotometry.cl  objects.lst    polima.men     spm_polima.dat
chpolangle.cl dopolarimetry.cl polidentify.cl polprocess.cl
```

content of directory 'doc':

```
checkcoo.hlp   chpolangle.hlp   dopolarimetry.hlp polprocess.hlp
chimagetyp.hlp cpcoo.hlp        polidentify.hlp  popol.hlp
chobject.hlp   dophotometry.hlp polima.hlp
```

content of directory 'identify':

```
3c273_identify.sh ct102_identify.sh h2048_identify.sh p1510_identify.sh
3c279_identify.sh e0033_identify.sh h2123_identify.sh p2155_identify.sh
3c371_identify.sh e0647_identify.sh h2453_identify.sh r0136_identify.sh
3c454_identify.sh e0806_identify.sh oj287_identify.sh r0214_identify.sh
3c66a_identify.sh e1959_identify.sh p0420_identify.sh s0716_identify.sh
a0235_identify.sh e2344_identify.sh p0528_identify.sh s0954_identify.sh
bllac_identify.sh g191b_identify.sh p0735_identify.sh
```

content of directory 'lib':

```
helpdb.mip  root.hd  rootpolima.hd
```

The main level directory contains program scripts ('.cl') and supplementary files. A 'README'-file explains the installation of the package.

<sup>8</sup><http://www.lsw.uni-heidelberg.de/users/jheidt/spm/spm.html>

The 'doc'-directory contains help-files for each task. Stand-alone scripts needed for object identification are found in the 'identify'-directory while the 'lib'-directory contains further supplementary files.

### 4.3.2 Installation

The package content should be copied into a new created directory (e.g. 'polima/') in the '/iraf/iraf/local/'-directory. Using the pipeline tasks needs some preparations, explained below.

#### Adjustment of login.cl or loginuser.cl

The 'login.cl' and 'loginuser.cl' files are both located in the IRAF-directory of the user (usually in his home-directory, i.e. '/home/username/iraf/'). To use the `polima` package, one has to insert the following lines into one of both files above the `keep` command at the end of the file:

```
### polima package setup
set polima = "/home/username/iraf/polima/"
task $polima = "polima$polima.cl"
reset helpdb = (envget ("helpdb") // ",polima$lib/helpdb.mip")

# set standard imagetype IRAF is using to FITS
set intype = "fits"

# initialize IMWCS
task $imwcs = "$/home/username/wcstools-3.7.6/bin/imwcs $1"
```

The first block defines the path of the `polima` files, initializes the package and the helpfiles. The second block, sets the image file format used by IRAF to FITS. Therefore, each image file has to carry the suffix '.fits'. The last block initializes the IMWCS-software as IRAF task (the path '/home/username/wcstools-3.7.6/' is just a suggestion and has to be adjusted).

The same information is given in the 'README' file contained in the package.

#### IMWCS installation

In order to use the automatic wcs registration via *IMWCS* (cf. 5.3.3) one has to download the software<sup>9</sup>. The software has to be unpacked into a directory where the user has writeable access.

In order to use the **USNO-A2.0** catalog online, one has to alter the IMWCS source code and compile the software. For this reason, one has to change into the WCS-TOOLS directory and open the file 'libwcs/uaread.c' using an editor. Uncommenting the following line as shown below allows online access:

```
/* Uncomment following line to use ESO USNO-A server for UA2 */
static char ua2path[64]="http://archive.eso.org/skycat/servers/usnoa-server";
// -----
```

<sup>9</sup><http://tdc-www.harvard.edu/software/wcstools/wcsprogss.html>

To compile the software, return to the WCSTOOLS directory and type 'make'.

In the following three chapters, the tasks of the `polima` package are introduced. The task parameters are outlined and a detailed description of what the tasks do is given.

A brief overview of how the pipeline is used properly can be found in C.

# Chapter 5

## Image reduction

Images acquired using CCD detectors contain artifacts which have to be removed before analysis starts. The theoretical basics have been outlined in 2.2.

*The following sections explain the approach used to perform the necessary corrections in the `polima` pipeline. Furthermore, some additional measures are introduced to simplify data handling.*

### 5.1 Raw Image Preparation - `polima.polidentify`

This task was originally designed to identify the imaged object using the image coordinates. This provides a unique designation for each object using a code (*5char-code*, cf. Tab. A.1, A.2 and A.3) and therefore a clear identification instead of observer-created labels. Later, the task was expanded by several header modifications to ease further image analysis.

The use of `polidentify` is mandatory for all following reduction and analysis steps.

#### 5.1.1 Parameters

`polidentify` is controlled via the following parameters:

```
all_images = "*fits"           image files
```

Images to be processed. Wildcard-symbols like the asterisk or question mark may be used.

```
(reference_catalog_string = "polima$objects.lst") reference catalog
```

Path to the reference-catalog-file containing object information (see below).

```
(logname = "logfile")         name of logfile
```

Name of the log file in which the task logs all processing steps.

```
(max_residual = 25)           max. residual in arcmins
```

Maximum residual the users allows. The residual is the difference between the catalog position and the telescope position during integration. 25 arcmins seem to be a good value to identify the SPM catalog objects. Smaller values may be possible but demand a very good telescope pointing.

Table 5.1: Excerpt of the SPM reference-catalog-file

3C_66A	3c66a	35.66500	43.03555	02:22:39.6	43:02:08
1ES_0647+250	e0647	102.69375	25.05000	06:50:46.5	25:03:00
S5_0716+714	s0716	110.47250	71.34333	07:21:53.4	71:20:36
PKS_0735+178	p0735	114.53083	17.70527	07:38:07.4	17:42:19
OJ_287	oj287	133.70375	20.10861	08:54:48.9	20:06:31
S4_0954+650	s0954	149.69666	65.56527	09:58:47.2	65:33:55
Mkn_421	mk421	166.11375	38.20888	11:04:27.3	38:12:32
ON_231	on231	185.38208	28.23305	12:21:31.7	28:13:59
3C_273	3c273	187.27791	2.052500	12:29:06.7	02:03:09
3C_279	3c279	194.04625	-5.78944	12:56:11.1	-05:47:22
Mkn_501	mk501	253.46750	39.76027	16:53:52.2	39:45:37

```
(imagelist = "no entry here")      internal list variable
(reference_catalog = "no entry here")  internal list variable
```

These parameters have no meaning for the user but have to be initialized here.

The **reference-catalog-file** has to be placed in a directory which is accessible for IRAF (usually the directory containing the `polima` package files). The file contains a table with the following columns (in this order):

- complete object name
- 5char object code
- right ascension as a real number
- declination as a real number
- right ascension in hour, minute and second
- declination in degrees, arcminute and arcsecond

The columns have to be separated using tabulators. The number of lines is not limited. Therefore, the table can be expanded or replaced by an alternative table. An example for a reference-catalog-file can be found in Tab. 5.1.

### 5.1.2 Description

After initializing internal parameters and checking for the necessary IRAF packages, a file is created containing all image-filenames to be processed. This list is successively run through. All following steps are done for each image separately.

First, the image identification is done. Therefore, the telescope pointing coordinates are read from the FITS header descriptors *RA* and *DEC* and each is converted to a real number. These



coordinates are compared to those provided by the reference-catalog-file and a residual is calculated for each. The 5char-code of the catalog entry leading to the smallest residual is the new object code. It replaces the FITS header descriptor *object* if the following is given:

- the FITS header *imagetyp* is not 'zero'/'bias', 'flat' or 'bad' (*imagetyp* described the image type meaning whether it is a scientific, correction ('object') or bad image, cf. 5.2.1)
- the calculated residual is smaller than the value of the parameter `max_residual`

If one of the former is not given, the FITS header will be updated providing a corresponding image type. In case of a too large residual, the object code is set to 'unknown' and a warning is displayed. Usually, such an image shows a target which is not part of the reference-catalog-file.

In any case, a line is written to the log file containing the image-filename, the calculated (smallest) residual, the new and the old header descriptor *object* and the image type. This allows the user to check for correct processing.

As a next step, the header descriptor *polangle*, which contains the polarimeter angle alignment, is checked for carrying one of the following values: 0, 45, 90, 135. This seemed necessary since the polarimeter alignment sometimes is read out incorrectly. Furthermore, for some measurements, the polarimeter angle sequence seemed to be corrupted which had to be checked manually. This problem was solved after the October/November-run 2008.

Eventually, some FITS header descriptors are updated:

- *epoch* gives the epoch of the provided coordinates and is set to '2000', which is necessary for the automatic WCS identification
- *secpix*, the angular resolution per pixel in arcseconds, depends on the detector type
- *gain*, CCD gain parameter, depends on the detector type
- *rdnoise*, CCD read noise, depends on the detector type
- *tra* (read 'TelescopeRA') and *tdec* ('TelescopeDEC'), the telescope pointing coordinates are transferred to these new descriptors respectively
- *ra* and *dec* are updated using the coordinates provided by the reference-catalog-file
- *tjd* (read 'TelescopeJD') contains the value of the descriptor *JD* which is calculated inaccurately in older observing runs
- *jd* contains the calculated Julian Date of the start of the integration with a accuracy down to seconds; for this calculation the descriptors *date-obs* and *ut* are used as a basis

After running `polidentify`, a message is displayed. Before starting image reduction, the user should check the log file for peculiarities and warnings. All necessary steps can be done using the auxiliary tasks `chimagetyp`, `chobject` and `chpolangle`.

## 5.2 Reduction Task - `polima.polprocess`

This task forms the core of the pipeline. Raw sciences images together with raw correction images are automatically processed and result in reduced science images ready to analyze. The user may also use external correction images.

Running the `polidentify` task before running `polprocess` is crucial for the reduction.

### 5.2.1 Preface

In order to keep the code as simple as possible, some features of the `imred.ccdred` package of IRAF are used. This demands correct information provided by two FITS header descriptors, namely `POLANGLE` and `IMAGETYP`. Both descriptors are written automatically by the telescope control software but may be incorrect for some reason. Their importance is explained together with the concepts both are featuring.

#### Subsets - *polangle*

The concept of `subsets` allows to group images using a specific feature and process images of different groups separately. Images are assigned to a subset using a predefined FITS header descriptor. In the case of SPM images, it was found reasonable to use the descriptor *polangle*, describing the polarimeter alignment angle during the integration, for this reason. This provides that all images of a specific *polangle*-value are processed together (using the same flatfield image e.g.). This significantly reduces the code.

The descriptor was sometimes written improperly in the past for some reason. The `polidentify` task helps to find anomalous angle values. However, the user should check for incorrect polarimeter sequences using the log file of the `polidentify` task.

#### Groups - *imagetyp*

The *imagetyp* descriptor describes the type of the image it belongs to. Supported are the types: `object` for sciences images, `flat` for flatfield images, `bias` or `zero` for bias images and `bad` for unknown or corrupted images. An image type is assigned automatically by choosing a macro in the CCD control software. If, for instance, a science image is accidentally flagged as flatfield image by setting the *ccdtype* descriptor to `flat`, it will not be regarded as science image but as a bias image. This may lead to some problems regarding image reduction.

Some problems occur in old data sets when macros were not available. Since the introduction of macros no severe problems have been observed.

### 5.2.2 Parameters

```
all_images = "*fits"           all files to process
```

Images to be processed. Wildcard-symbols like the asterisk or question mark may be used.

```
(create_bias = yes)           use masterbias created from data
(biasfile = "masterbias.fits") name of masterbias
```

If the parameter `create_bias` is set to 'yes', a masterbias is created from bias images included in `all_images`. If it is set to 'no', an already existing masterbias is used for bias subtraction. In this case, the filename including path has to be given to the parameter `biasfile`.

The creation of a masterbias demands at least one bias image. More than 5 images are recommended to have sufficient statistics. A warning will be displayed if the number of bias images is smaller than 3.

```
(create_flat = yes)           use masterflat created from data
(flatlistfile = "masterflats.lst") list of masterflats
(flatprefix = "masterflat_")  masterflat prefix
```

If the parameter `create_flat` is set to 'yes', masterflatfield images are created from flatfield images included in `all_images`. If it is set to 'no', already existing masterflatfield images are used for flatfield division. In this case, a file has to exist containing the filenames of all four masterflatfield images. The name of this file must be entered in `flatlistfile`. The parameter `flatprefix` provides the prefix for the filenames of the masterflatfield images which are created using raw data. If external flatfields are used, this parameter has no meaning.

The creation of masterflatfield images demands at least one flatfield image per polarimeter angle. More than 5 images per angle are recommended to have sufficient statistics. A warning will be displayed if the number of flatfield images per angle is smaller than 3.

```
(logname = "logfile")       name of logfile
```

Name of the log file in which the task logs all processing steps.

```
(redpath = "reduced/")     where to save reduced images? (must exist!)
```

The parameter `redpath` provides the path where the reduced image have to be saved to. It is crucial that

- the pathname has to end with a slash ('/') and
- the referred directory has to exist in advance.

```
(hthresflat = 50000.)      upper threshold for flatfields
(lthresflat = 5000.)       lower threshold for flatfields
```

These parameters set the upper and the lower threshold for flatfield images. If the median value of the central region of a flatfield image is outside these limits, the image is considered underexposed or saturated. Thus, it is not used for the creation of a masterflatfield image. The preset values satisfied all expectations so far.

```
(tmplist = "no entry here")  internal list variable
(objlist = "no entry here")  internal list variable
(pollist = "no entry here")  internal list variable
(imlist = "no entry here")   internal list variable
```

These parameters have no meaning for the user but have to be initialized here.

### 5.2.3 Description

After initializing internal parameters and checking for the necessary IRAF packages, the *ccdred* and *ccdproc* routines are set up, as well as detector depending settings like the overscan region and the innermost image section, which is later used for image statistics since it is vignetting free (later referred to as *statsec*, cf. Fig. 3.6).

If external masterflatfield and/or masterbias images are used, the following two paragraphs are skipped.

#### Masterbias creation

First, the number of raw bias images is determined. If it is smaller than three, a warning is displayed proposing to use an external masterbias. If there is no raw bias image at all, the process is cancelled and stopped.

To create a masterbias, the IRAF task `zerocombine` is used, which is part of the `ccdred` package. It offers automatized routines for the creation of masterbias images. The task's settings are

- input images are all 'bias'-flagged images contained in `all_images`
- images are combined using the median operation
- 'avsigclip' (*averaged sigma clipping*) algorithm is used for bad pixel rejection. The algorithm estimates a noise level (sigma) for each pixel using a calculated gain factor and a median pixel value in ADU. Pixels exceeding this the median pixel value by 3 times the sigma value (in positive or negative direction) are rejected. This process is repeated using a recalculated sigma until no more pixels are rejected. This algorithm makes sure that no bad pixels or cosemics propagate into the masterbias image.
- all image statistics operations are limited to the `statsec`-area of the image to prevent polarimeter-vignetting from affecting the statistics
- all raw bias images are overscan corrected

The resulting file is named 'masterbias.fits'. Detailed information on the process and it's settings are found in the log file.

Since bias images are not illuminated in any way, the polarimeter angle *polangle* is neglected. Masterbias images using different `polangle` parameters, partly taken in an illuminated telescope dome, have been compared and showed no differences. Therefore, bias images may be taken at any time during the observations.

#### Masterflatfield creation

Proper flatfield handling is crucial to receive a high data quality. Therefore, each flatfield image contained in the set is checked for over- and underexposition. For this reason, the median value of each raw flatfield image is determined (using the `statsec` area) and compared with the `hthresflat` and `lthresflat` parameters set by the user. If the median value lies outside the threshold, the `imagetyp` descriptor is set to 'badflat', i.e. the image is disregarded in the further process. The

selection process is protocolled in the log file. As a result, only flatfield images providing good S/N-ratios are passed to the combining process. Furthermore, passing images are normalized using the median.

The remaining number of raw flatfield images is checked. Here, the number of flatfield images per polarimeter angle is regarded. One image per *polangle* is mandatory, a warning is displayed if only three or less images are available.

The raw flatfield images are combined using the `flatcombine` task of the `ccdproc` package. The task makes use of the `subset` concept, i.e. images carrying the same *polangle* descriptor value are combined to one resulting image. The procedure is explained using the task parameters

- input images are all 'flat'-flagged images with the same *polangle* value contained in `all_images`
- images are combined using the median operation
- 'avsigclip' (*averaged sigma clipping*) algorithm is used for bad pixel rejection (cf. master-bias creation)
- all image statistics operations are limited to the `statsec`-area of the image to prevent polarimeter-vignetting from affecting the statistics
- all raw flatfield images are bias and overscan corrected
- output images are named according to the `flatprefix` parameter; the *polangle* value is appended

As a result, a set of four masterflatfield images is created according to the four possible *polangle* values. Furthermore, a file named after the parameter `flatlistfile` is created containing the filenames of the masterflatfields.

The `flatcombine` task creates a FITS header descriptor *ccdmean* containing the mean (the `polima` software uses the median) pixel value of the complete image, which is used for a second normalization when applying the correction images. However, the task is not able to use a pre-defined image section for this determination. Therefore, the vignetted areas at the edges of each image are included here, distorting the real mean value. To solve this problem, the *ccdmean* descriptor is changed to a more realistic value determined using the `statsec` area. This approach was tested using data of different runs and leads to satisfying results.

When setting up the pipeline, the question arose which kind of flatfield images should be used. The differences between image reduction using flatfields taken during dawn and dusk were examined, as well as the impact of using a single flatfield image for each polarimeter angle and flatfields averaged over the different polarimeter angles.

**Dawn-Flatfield vs. Dusk-Flatfield** For this examination an image set was reduced using three different flatfield images. One is a combination of flatfield images taken during dusk, the second one consists of dawn-flatfields, respectively. The third flatfield is a combination of all available flatfield images, ignoring the daytime of exposure. The single flatfield images were taken in the same night and combined using the median to one masterflatfield image per polarimeter angle.

The reduced images were examined using statistical methods for background brightness and background noise. Visual comparison showed no difference, as well as background brightness.

However, noise comparison showed that the noise level of combined flatfield images is smaller than the highest noise level of the dusk- or dawn-flatfields. Neither one of the latter shows a clear preference of having a smaller noise level compared to the other one.

Therefore, it is recommended to combine both types of flatfield, i.e. images taken during dusk and dawn, to a single masterflatfield image per polarimeter angle.

**Combining Flatfields of Different Polarimeter Angles?** A second question is, whether one should use one masterflatfield image per polarimeter angle or rather combine all flatfield images to one single masterflatfield image disregarding polarimeter angle (cf. Fig. 3.6). A test sequence similar to the one outlined above was performed.

Again, noise level comparison between both types of flatfield images shows slightly better results when using a single masterflatfield for each polarimeter angle. Another argument speaking for this approach is, that dust contaminations on optical surfaces of the polarimeter can be corrected this way. Otherwise, contaminations strongly affect analysis results.

Therefore, the pipeline uses all existing flatfield images contained in the image set, without respect to the time of exposure but regarding the polarimeter angle to create a set of masterflatfield images. The user can control which flatfield images to be used by confining the set.

## Object Image Handling

First, a list of all raw object images is created. Essentially, each image is now reduced using the task `ccdproc` which is part of the `ccdred` package. The task provides a complete image reduction (bias, overscan and flatfield correction) using the correction images created before or external correction images. The reduced images are saved under a preliminary filename.

An important feature of the `polprocess` task is that reduced images are saved under a certain filename which is constructed from FITS header information. The filename contains four segments which are segregated using an underscore '\_':

1. 5char-object code
2. polarimeter alignment angle (*polangle*, displayed using three figures)
3. data acquisition date using the format 'YYYY-MM-DD'
4. a counting variable which increases with every image carrying the same three values mentioned above

For instance, the filename `'b11ac_045_2009-04-23_3.fits'` marks an image of BL Lac, taken on April 23rd, 2009, using a polarimeter alignment angle of  $45^\circ$ . This image is the third one taken with the characteristics listed above.

Hence, the software assures to assign a unique filename to each reduced image. The first two segments are directly taken from the header descriptors. The **data acquisition date**, however, has to be corrected since the header only provides a descriptor carrying the acquisition date given in Universal Time (descriptor *date-obs*). For the sake of simplicity, the daynumber is decreased by one. This is possible since the OAN uses Pacific Standard Time (PST), which means  $UT - 7h$ .

Observations never start before 5 p.m. local time. Hence, this simple correction leads to a correct date. Ambiguities are not possible. The only problem occurs on the last day of a month. Since the UT date of such a day is the first day of the next month, the correction leads to the 0th day of the new month. This oddity is acceptable. Otherwise, an algorithm would be needed which is aware of the number of days of each month. The benefits would not justify the efforts.

Eventually, the reduced images are transformed to have them aligned correctly: north points to the top, east to the left. This transformation depends on the detector type used:

**THOMSON 2k** : rotate image by  $180^\circ$

**MARCONI** : rotate image by  $180^\circ$

**SITE 1** : mirror image at y-axis and rotate  $90^\circ$  counter-clockwise

Images created by `polprocess` are properly reduced and ready for any kind of analysis. In order to use the analysis tasks `dophotometry` and `dopolarimetry` running the task `popol` is highly recommended.

### 5.3 Post Reduction Handling - `polima.popol`

This task prepares reduced images for the use of the analysis tasks `dophotometry` and `dopolarimetry`. Using this task is not mandatory but highly recommended. It provides image cropping to decrease the file size and automatized object identification. Two methods for object identification are available and described below. The correctness of the identification can be tested using the `checkcoo` task.

#### 5.3.1 General Concepts of Object Identification

In order to be able to perform automatized photometry (or polarimetry) it is important to identify objects in the image properly. Three steps are necessary to achieve this.

1. Objects in the image have to be detected.
2. The detected objects have to be identified using an existing catalog.
3. The image coordinates of identified objects have to be extracted and saved.

The first two steps depends on the object which was observed. The two possible approaches are explained in detail below. The third step is the most important for the user. The idea is to create for each FITS image two catalog files. One is called **coordinate-file**. It contains the image coordinates of each object of interest in the image, i.e. usually one science object and comparison objects. The second file is called **reference-magnitude-file** and provides for each entry of the coordinate-file the following information: object-name, magnitude of the object, error of the magnitude. In case of the to be measured source the according line in the reference-magnitude-file must be

```
src      0      0
```

in order to identify this object as the source of interest. Furthermore, to prevent any confusion, this line should always be the first line in both files.

It is crucial that the **objects are listed in the same order in both files**. Both files carry the original filename of the FITS image with a suffix: `'_coord'` for the coordinate-file and `'_ref.mag'` for the reference-magnitude-file.

An example is displayed in Fig. 5.1. It shows an image of BL Lac in which important objects are marked using red crosses. The coordinate-file carries the image coordinates (x and y in this order) of each object. The reference-magnitude-file lists the corresponding names of the objects, as well as their magnitudes and errors in magnitude. For instance, comparison star H has a magnitude of 13.73 mag with an statistical error of 0.06 mag and is positioned at the image coordinates  $x=365.650$  and  $y=366.735$ .

The advantage of this concept is to have all object data concerning one image well-arranged in special files. This allows the user to check positions and information and even alter them. Furthermore, it is easily possible to create both files manually. Positions can be obtained using the IRAF task `imexam`. This may be necessary in case of a wrong automatical object identification using `popol` which is part of the `polima` package.

### 5.3.2 Parameters

```
all_images = "*fits"          image files
```

Images to be processed. Wildcard-symbols like the asterisk or question mark may be used.

```
(logname = "logfile")       name of logfile
```

Name of the log file in which the task logs all processing steps.

```
(crop = yes)                crop images?
```

If set to 'yes', the relevant (central) image section is cropped from the image. The cut-out region depends on the CCD detector.

```
(wcs = yes)                  find wcs coordinates using WCSTools?
```

Identifies the objects in the image and writes WCS data into the FITS header. Uses the `imwcs` task of the `wcstools` package (more information below). Furthermore a coordinate- and reference-file are created.

```
(brighteststar = no)        find brightest star
```

Identifies the brightest source in the image and creates a coordinate- and reference-file.

```
(imagelist = "no entry here") internal list variable
(tables = "no entry here")   internal list variable
```

These parameters have no meaning for the user but have to be initialized here.



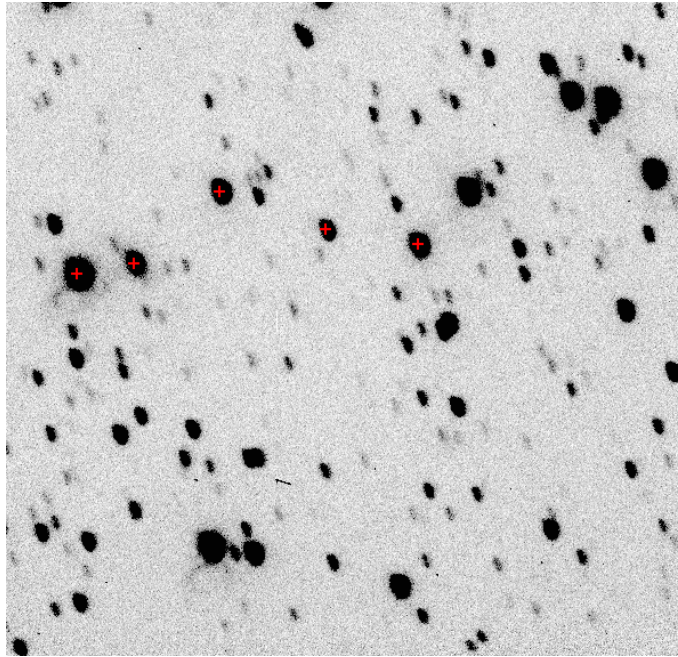


Figure 5.1: Image of BL Lac displayed using `checkcoo` (colors inverted, crosses colored red)

Figure 5.2: coordinate-file

```
116.861 349.949
67.059 340.923
191.953 412.982
365.650 366.735
285.100 379.939
```

Figure 5.3: reference-magnitude-file

```
src      0      0
B        11.99  0.04
C        13.79  0.05
H        13.73  0.06
K        15.00  0.07
```

### 5.3.3 Description

After initializing internal parameters and checking for the necessary IRAF packages, a file is created containing all image-filenames to be processed. This list is successively run through. All following steps are done for each image separately.

The following three paragraphs explain the main functions of the task. Each is run, if the according parameter is set.

#### Image crop

After reading the *detector* descriptor from the FITS header, the image file is overwritten using the according central image section. Eventually, a FITS header descriptor *crop* is created as part of the new file.

**Background** The relevant image area is cropped in order to save memory, accelerate further image processing and prevent interferences from the obstructed image sections. This obstruction is created by the polarimeter (cf. 3.1.3) and leads to a quasi circular unobstructed region of the CCD image (Fig. 3.6) for all polarimeter alignment angles. Only objects inside this area are later used for image analysis, which is checked in the according task. The rectangular section cropped here includes this area completely and leaves some space for adjusting the circular region if necessary (e.g. if comparison stars are positioned at the edge of the circular region). The extent of the rectangular section depends on the detector: (each for  $2 \times 2$ -binning)

- MARCONI: [250:850,200:780]
- THOMSON 2k: [240:760,230:760]
- SITe 1: [90:420,90:420]

using the format  $[x_1:x_2, y_1:y_2]$  with  $x_i$  representing columns and  $y_i$  representing lines.

The unobstructed area is described by a circle. Center coordinates and radius depends on the detector type

- MARCONI: center [302,292], radius 285
- THOMSON 2k: center [267,268], radius 264
- SITe 1: center [157,165], radius 161

(all specifications according to binning  $2 \times 2$ )

#### Object identification using WCS

According to the three steps of object identification, all objects in the image have to be detected first. This is done using the *daofind* task of IRAF, which locates local density maxima. The task demands two parameters to run properly: the FWHM of the pointspread-function of the objects and a measure for the background noise. However, these parameters, especially the FWHM of the PSF, vary from one image to another and choosing the correct parameter value is delicate.

Therefore, the task is first run using preset values for both. The twenty brightest objects resulting are extracted and analyzed using the task `psfmeasure` to get a median FWHM of the PSF. The object detection using `daofind` is then redone using the estimated FWHM and a scaled down image (factor 3). This rescaling process was found useful to anticipate double detections of objects due to tracking problems. Again, the 15 brightest objects are extracted and matched with the USNO-A2 catalog to find the exact position of the image using the *IMWCS* standalone-routine of the external *WCSTOOLS* package (cf. 4.1.1). WCS information are written to FITS header.

WCS identification works with good results if enough objects are found in the field-of-view. If the number of objects is smaller than seven, the automatic identification may fail. In this case, a manual object identification is inevitable. Using the FWHM-determination and down-scaling of the image improves the success rate clearly. Success is nearly independent from focus quality.

Eventually, the coordinate and reference-magnitude files are created using external scripts which are found in the *identify* subdirectory of the *polima* directory. The appropriate script is chosen using the *OBJECT* descriptor. Setup and purpose of the *identification scripts* are explained in 4.1.1.

### Brightest Star Identification

Due to the extreme brightness of standard stars compared to other objects integration times are here much shorter. This leads to a small number of stars in the field-of-view which complicates the use of *IMWCS*. However, one can take an advantage of the brightness of standard stars by looking for the brightest source in the image. This is explained in the following.

First, the center of the not-obstructed image area is determined depending on the detector type. The FITS image is then scaled down by a factor of five using the IRAF task `magnify` to smooth small features like cosemics and small objects. Flux is conserved in this process. Therefore, the brightest pixel in the image must be the center of the brightest object. This brightest pixel is found by converting the image into a sorted pixel list. Pixels at the edge of the image might interfere this assumption since a lot of image processing artifacts are present here. Therefore, the distance of the brightest pixel from the center of the unobstructed area is determined and compared to a threshold. If the pixel lies outside the bounds, the next brightest one is regarded.

The final coordinates are then written to a coordinate file. A reference-magnitude file is created too, to enable compatibility to the analysis tasks.

### 5.3.4 Cosmics Correction

A correction algorithm was integrated in the script but removed again later. It showed a clear impact on polarization measurements.

Usually, there is no need for cosmics removal in SPM images. Contaminations of objects are extremely rare but obvious, since they lead to anomalous results.

## 5.4 Auxiliary Tasks

In order to simplify the use of the `polima` pipeline a set of auxiliary tasks was created. This enables everybody to use the pipeline without having a deeper knowledge of its internal structure or IRAF programming.

### 5.4.1 `chimagetyp`

This task changes the *imagetyp* header descriptor and therefore the image type assignment of the image. The parameters are:

```
filename = "*.fits"      image file
```

Images to be processed. Wildcard-symbols like the asterisk or question mark may be used.

```
newtype = "obj"         new IMAGETYP
```

The new *imagetyp* descriptor. Possible values are 'object', 'zero', 'bias', 'flat' or 'bad'.

```
(logname = "logfile")   name of logfile
```

Name of the log file in which the task logs the change.

The task uses the `hedit` routine of IRAF. If the descriptor does not exist in the image header, it is created. Otherwise, the value is overwritten.

### 5.4.2 `chobject`

This task changes the *object* header descriptor. The parameters are:

```
filename = "*.fits"      image file
```

Images to be processed. Wildcard-symbols like the asterisk or question mark may be used.

```
newobj = "none"         new OBJECT
```

The new *object* descriptor. There are no restrictions to the value.

```
(logname = "logfile")   name of logfile
```

Name of the log file in which the task logs the change.

The task uses the `hedit` routine of IRAF. If the descriptor does not exist in the image header, it is created. Otherwise, the value is overwritten.

Technically, every string is possible as new value of the descriptor. However, the user has to keep in mind that a change of the *object* descriptor might affect the filename generation and lead to problems in image identification.

### 5.4.3 chpolangle

This task changes the *polangle* header descriptor. The parameters are:

```
filename = "*.fits"      image file
```

Images to be processed. Wildcard-symbols like the asterisk or question mark may be used.

```
newangle = "0"          new POLANGLE
```

The new *polangle* descriptor. Possible values are '0', '45', '90' and '135' according to the polarimeter alignment angles of the Polima device.

```
(logname = "logfile")  name of logfile
```

Name of the log file in which the task logs the change.

The task uses the `hedit` routine of IRAF. If the descriptor does not exist in the image header, it is created. Otherwise, the value is overwritten.

### 5.4.4 checkcoo

The `checkcoo` task provides a visual check of the correctness of the wcs or brightest star identification. It uses the `display` and `tvmark` tasks to display the image in DS9 and plot object positions, respectively. It offers the parameters:

```
files = "*fits"        image files to check
```

The image files to be displayed. Wildcard-symbols like the asterisk or question mark may be used.

```
(polygons = no)       show polygons?
```

Show polygon aperture instead of coordinate-file.

```
(count = 200000)     number to count to
```

Each image is displayed for some time. The duration controlled by this parameter. The larger this value, the longer is each image displayed.

```
(imagelist = "no entry here") internal list variable
```

This parameter has no meaning for the user but has to be initialized here.

An example for the output of `checkcoo` is displayed in Fig. 5.1.

### 5.4.5 cpcoo

Sometimes, wcs identification using `popol` works only for some images of a set, but not for all of them. Determined object positions may be shifted, or there may be none of the objects identified. In this case, the properly processed images may be used to correct the other ones using `cpcoo`. The routine makes use of the IRAF task `incentroid`, which calculates shifts between selected objects in an image set.

`cpcoo`'s parameters are:

---

```
images = "*.fits"      image files
```

Input images, which are about to be corrected. It is not necessary that they already have a coordinate- or reference-magnitude-file.

```
refimage = "ref.fits"  reference image file
```

The reference image file has to have a correct coordinate- and reference-magnitude-file.

```
(logname = "logfile")  name of logfile
```

Name of the log file in which the task logs all steps.

```
(centerbox = 11)      centering boxsize
```

Boxsize used for object centering (refers to 'bigbox' parameter of the `imcentroid` task). This value can be seen as a measure for the PSF's diameter. The initial value (11) works fine for well-focused images with little guiding problems. For perfect guiding, smaller values are recommended. If the image suffers from severe guiding or focus problems, the `centerbox` parameter should be increased. Generally, the smallest working value gives the best results.

```
(iterations = 5)      centering iterations
```

Number of iterations in the centering process.

```
(imagelist = "no entry here") internal list variable  
(tables = "no entry here") internal list variable
```

These parameters have no meaning for the user but have to be initialized here.

The script determines the shift of each image from the `images` set in respect to the reference image `refimage` using `imcentroid`. A proper choice of `centerbox` is mandatory. If centering did not succeed, a warning is displayed and the task can be rerun.

If centering did succeed, reference-magnitude-file of the reference image is copied to each of the input images and a adapted coordinate-file is created.

The script works well for image sets taken during one night with small shifts up to approximately 20 pixels. For larger shifts, for one image of the input set the coordinate- and reference-magnitude-file should be created manually and then used as reference file.

# Chapter 6

## Photometry

Before going into the details of polarimetry methods, it is useful to have a proper handling of photometry, since both is based on flux measurements. Furthermore, photometric analysis is of interest, too.

*The first section explains the principles of aperture photometry, following the designed photometry script is introduced. The third section shows testing methods and results. Eventually, some selected photometric data are presented.*

### 6.1 Aperture Photometry

Photometry in general means the measurement of an objects flux in a specific wavelength range. This gives not as much information about the originating physical processes as a complete resolved spectrum would give, but is rather easy to obtain. Shorter integration times and therefore a higher scientific yield argue for photometric methods, if data of low spectral resolution are needed. This is just the case in variability monitoring projects.

There are two main methods in photometry to determine an objects flux: PSF-Photometry and Aperture Photometry.

**PSF-Photometry** uses the fact that the objects image gets convolved by the telescope optics. The resulting image is described by a **point spread function** (PSF). Assuming a point-like source

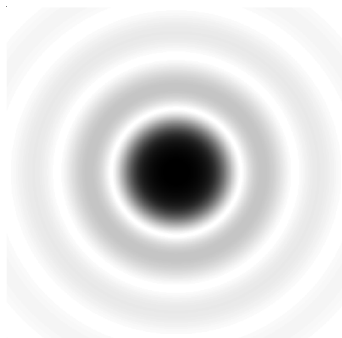


Figure 6.1: Airy disc as Point Spread Function of a circular Telescope Aperture

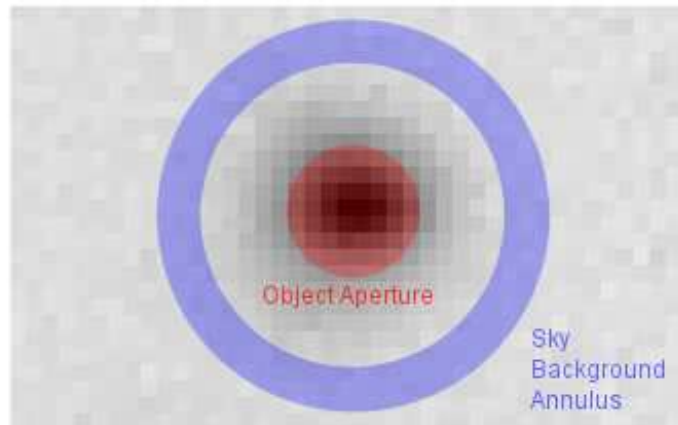


Figure 6.2: Aperture Photometry: definition of aperture and sky annulus

and a circular telescope mirror, the image is - in the non-realistic case of disregarding atmospheric influences - an *Airy disc* (Fig. 6.1). By fitting the theoretical PSF to the image, one can determine the objects flux. PSF fitting is useful for crowded fields, where some objects might overlap. On the other hand it is computationally intensive and hard to implement when object images suffer from bad focus, guiding errors or bad seeing. This leads to additional distortion of the airy disc and makes fitting more complicated.

**Aperture photometry** means a technique to measure an objects flux using a circular (or other shaped) aperture. Hence, it makes no assumption about the objects point spread function. It is suitable for non-crowded fields and requires only simple arithmetics.

The basic application of aperture photometry starts with finding the best approximation for the objects center on the image. This can be obtained by calculating the weighted average over the objects profile. Around this best estimate for the center, a circular software aperture of radius  $r$  is inscribed. To obtain the flux of the object, all pixel values that lie within the radius are summed up. However, this value also includes some photons coming not from the object itself, but from the sky background, e.g. *airglow*. Since this additional sky background brightness is not part of the objects flux, it has to be subtracted from the sum of the pixel values. The sky background is determined using an annulus around the center of the object and summing up all pixel values that are covered by the annulus. To avoid inclusion of other objects like neighboring stars or cosmics, rejection algorithms are needed. The arrangement of aperture and sky annulus is illustrated in figure 6.2.

Although aperture photometry is a simple technique, it may lead to avoidable errors if applied in an unsuitable manner. One important question is the choice of the aperture radius. One may find it appropriate to include in the aperture as much of the object's flux as possible, hence to choose a large radius of e.g. 3 FWHM of the stars brightness distribution. In this case, nearly 100 % of the flux are included. On the other hand, the aperture area here is large compared to the case when using a smaller radius. Having a look at the S/N equation 2.3 shows that a large flux increases the signal-to-noise ratio. But on the other hand, a large aperture area  $n_{\text{pix}}$  increases the noise term, decreases the S/N ratio and increases the error of the magnitude (cf. Fig. 6.3). One can interpret this as the following: the inclusion of many pixels lying far away from the source



center means the inclusion of additional noise contributions. Thus, a balance between inclusion of more signal (larger  $r$ ) and minimizing  $n_{\text{pix}}$  in the source aperture (smaller  $r$ ) leads to an optimal extraction radius for a given source. [How06]

Another problem of aperture photometry is how to treat pixels which are only partially covered by the aperture. This is illustrated in figure 6.2. State-of-the-art software counts these pixels weighted by the percentage of the pixel which is covered. This is the best way to minimize this digitization error.

The apparent magnitude of the object of interest can now be calculated using relation 2.2. Since differential photometry is performed here, at least one comparison star of well-known magnitude is needed. The error of the measurement can be minimized by increasing the number of measurements, i.e. to use a set of comparison stars and average the measurements.

## 6.2 Photometry Software - dophotometry

This task determines the apparent magnitude of a source from a set of up to 10 images. Since this script is designed for photometry of polarimetric images, one has to have the same number of images for each polarimeter angle to avoid polarization effects. For object identification the script makes use of coordinate- and reference-magnitude-files (cf. 5.3.1). Flux determination is performed by the `apphot-tasks phot` and `polyphot`. To calculate the apparent magnitude of the source, fluxes of each image are summed up and errors are propagated accordingly.

To be able to follow calculations done, a photometry logging file is set up containing all important results.

The script is developed for processing polarimetric images, but can be used with any image set.

### 6.2.1 Preface

The `dophotometry` script is based on the IRAF package `digiphot.apphot` [Dav90]. This package contains a set of photometry tasks for use on uncrowded or moderately crowded stellar fields in either interactive or batch mode. Several tasks are provided for computing accurate object positions and sky background fluxes for a list of objects and performing photometry using circular or polygonal apertures.

Since the amount of images in the SPM project is large, it was found useful to automatize photometry as far as possible. For this reason, object identification using the coordinate and reference-magnitude-file was designed (cf. 5.3.1).

### 6.2.2 Parameters

`polima.dophotometry` input parameters are:

```
images = "*.fits"          images to be used
```

Images which are about to be analyzed. Wildcard-symbols like the asterisk or question mark may be used. Polarimetric input images have to include the same number of images for each of the four polarimeter angles to avoid polarization effects.

---

```
(aperture = 1)           full aperture in px or multiple FWHM
```

Inner aperture radius for aperture photometry. The scale and meaning of this parameter depends on the settings of `fitaperture`:

- `fitaperture = no`: `aperture` means the full diameter of a circular aperture in pixels
- `fitaperture = yes`: `aperture` means the full diameter of a circular or the major axis of an elliptical aperture, respectively, measured in FWHM of the object image

```
(fitaperture = no)       fit aperture using psfmeasure?
(ellipticfit = no)       if fitting, use an ellipse?
```

If `fitaperture` is set to 'no' a circular aperture is used with a fix aperture diameter. In this case the parameter `ellipticfit` has no meaning. However, if `fitaperture` is set to 'yes' the aperture is fitted to the objects image. The shape of the aperture depends on the parameter `ellipticfit`:

- `ellipticfit = yes`: a polygonal aperture of elliptical shape is fitted; the polygon has 12 vertices and is fitted using the objects FWHM, ellipticity and position angle
- `ellipticfit = no`: a circular aperture is fitted using the objects FWHM as diameters

```
(minapradius = 1.)       minimum aperture radius in px
(maxapradius = 50.)      maximum aperture radius in px
```

Both parameters define the range of allowed aperture radii in pixels. The intention is to limit the size of the aperture in case of crowded fields and provide a minimum aperture size. Please give attention to the fact that these parameters define a radius while `aperture` defines the diameter of the aperture.

```
(logname = "photlog")    prefix of logging file
```

All steps of analysis are documented in a log file. The filename of this file uses this string as prefix. Object name and acquisition date are appended.

```
(writetotable = no)      write result to table?
(tablefile = "result.tab") result table file
```

If `writetotable` is set to 'yes' the results of the analysis are written to the file `tablefile` in table form. This allows a quick access to analysis results for further processing.

```
(usecomp = "")           use only these comparison obj.
```

This parameter allows to constrain the use of comparisons objects. If `usecomp = ""`, all available comparison objects are used to determine the objects magnitude. The use of comparison objects may be constrained by listing them here. For instance, the string 'A,B,C1' allows only the objects 'A', 'B' and 'C1' to be used as comparison objects. All other objects are disregarded. It is important to have comparison object names in exactly the same notation as used in the reference-magnitude-file and to have them separated by comma without whitespaces.

```
(vignetting = 1.)       use multiple radius of unobscured field
```

Image regions close to the edge of the CCD are subject to obstruction due to the polarimeter device. In order to have proper photometry results only objects are used which are completely unobstructed (cf. 5.3.3). Sometimes objects are located at the rim of the unobstructed circular area. If the user wishes to increase the radius of the usable area he has to increase the **vignetting** parameter by a small portion. It represents a factor which is multiplied to the radius of the unobstructed area.

```
(imagelist = "no entry here") internal list variable
  (tables = "no entry here") internal list variable
```

These parameters have no meaning for the user but have to be initialized here.

### 6.2.3 Description

First, internal parameters and arrays are initialized and a check for necessary IRAF packages is performed. After that, the **apphot** package is initialized which is needed to run included tasks properly. Some settings may be changed again later. Eventually, a file is created containing all image-filenames to be processed. This list is successively run through. The next steps are done for each image separately.

Since the availability of a coordinate-file and a reference-magnitude-file is mandatory, the existence and the content of the former is checked for the actual image. After that the program follows one of three possible branches depending on the settings of the parameters **fitaperture** and **ellipticfit**. Each branch provides a different method of flux determination.

If the parameter settings are **fitaperture = yes** and **ellipticfit = yes**, an elliptical fit of the objects image (i.e. PSF) is performed. For this reason the objects FWHM, ellipticity and position angle are determined using the IRAF task **psfmeasure** which is part of the **obsutil** package. The properties of each object listed in the coordinate and reference-magnitude-files are measured. Each variable is then averaged. The determined FWHM is checked for being in the limits of the **maxapradius** and **minapradius** parameters and adapted if necessary. To ensure best estimations of object center positions, the **apphot.center** task is run, which improves object center coordinates taken from the coordinate-file using a centroid algorithm. These improved center coordinates, the averaged FWHM, ellipticity and position angle are now used to calculate 12 vertices of a polygon in the shape of an ellipse for each object contained in the coordinate file. The 12 vertices are distributed homogeneously around the center with an angular distance of 30°. Their radii depend on the values mentioned above. The positions of all vertices of each object are successively written to a second coordinate-file with the suffix '.coo.polygons' - the **polygon-file**. This file is mandatory for running the **polyphot** task, which finally performs flux determinations of all objects. It provides arbitrary aperture shapes described by polygons.

However, if parameter settings are **fitaperture = yes** and **ellipticfit = no**, a circular fit of the object is performed which simplifies the routine. In this case only the FWHM of all objects is determined using **psfmeasure**. The averaged value is then checked for being in the limits of **maxapradius** and **minapradius** and used by the **phot** task of the **apphot** package to perform

circular aperture photometry.

Eventually, if `fitaperture = no`, flux determination is performed by the `phot` task using a fixed circular aperture, given by `aperture`.

For each method of flux determination, the sky background annulus is determined the same way: its inner radius equals 3 aperture radii with a thickness of 3 aperture diameters. This provides a sufficient number of pixels for proper sky background estimation. The resulting value equals the median of the pixel value distribution. This approach was tested using a number of different images and results agree perfectly with measurements performed by hand.

The results of each flux determination method are written to a text file named after the image filename with the suffix `.mag` containing all results of the aperture photometry for each object contained in the coordinate-file. Important results are exported to a table file (image filename`.tbl`), namely: sky background flux per pixel (`'MSKY'`), object flux error (`'STDEV'`), number of pixels inside the annulus (`'NSKY'`), number of pixels inside the aperture (`'AREA'`) and flux (`'FLUX'`). The file contains one line per object. Following, a number of FITS header information is read from the image needed for further analysis.

The following steps are performed when the former ones have been applied to each image, i.e. when fluxes of all images are determined.

Data contained in the `.tbl`-file are read in according array variables. Before calculations starts, each object is checked to be inside the obstruction free area of the image (cf. 5.3.3). Objects outside this area or on the edge are not used in the further process. Photometric data and all following calculation steps are written to the logfile to enable transparency and allow the user to follow each step.

Calculations start with the summation of fluxes, errors and areas of each object from all images. One has to keep in mind, that the images have not been taken at the same time, i.e. there might be differences in airmass which have to be taken into account (cf. 2.3.3). Following, summed up fluxes and areas are used to calculate the SN-ratios of the objects according to Eq. 2.5. Finally, object magnitudes (Eq. 2.2) and magnitude errors (Eq. 2.6) are calculated from these.

In order to have a measure for the quality of the measurement, the mean magnitude and rms error of each comparison object is calculated using all other comparison objects as reference objects. The deviation of the calculated from the real magnitude of the comparison object given in multiple mean errors is calculated and printed to the logfile. Outliers are clearly visible this way and may be excluded using the `usecomp` parameter (cf. 6.3.1). Furthermore, the magnitude of the first comparison object (denoted as object *i*) from the reference-magnitude-file (which is authorized by the `usecomp` parameter) is determined. The residual in magnitude  $\Delta m_i$  (also referred to as: *compstar residual*) between the 'real' magnitude ( $m_{i,\text{real}}$ , as given by literature) and the calculated one using the comparison object *j* ( $m_{i,\text{computed using } j}$ ) is averaged over all objects *j* (Eq. 6.1). The rms error is determined, too.

$$\Delta m_i = \frac{1}{\#j} \sum_{j \neq i}^j (m_{i,\text{real}} - m_{i,\text{computed using } j}) \quad (6.1)$$

If only one comparison object is available, the residual is set to 0. The residual may be high if the scattering of comparison object magnitudes is high. Residuals can be decreased - i.e. accuracy increased - by using a selected sample of comparison objects.

Eventually, the mean time of exposure is calculated. It represents the mid-time of all exposures. Its errors overlap the total exposure time, i.e. the time between the start of the first exposure and the end of the last one. Furthermore, the logfile is renamed using the `logname`-prefix, the object name from the FITS header and the observation date. Results are written to `tablefile` if wanted.

The entry of the `tablefile` contains the following data, separated by tabulars:

1. mean magnitude of the object of interest
2. rms error of the object of interest (including errors of the comparison objects)
3. rms instrumental error of the object of interest (determined by flux only)
4. compstar residual
5. rms error corresponding to compstar residual
6. SN-ratio of the object of interest
7. mean time of exposure
8. error of the mean time of exposure (represents half of the total measurement time)
9. aperture parameter
10. maximum residual magnitude of all comparison objects expressed in multiples of its rms error
11. list of applied aperture diameters (in pixels) for each image

## 6.3 Testing

### 6.3.1 Reliability of Results

The script shows good results and a robust handling. Using several comparison objects allows good quality control. This is outlined using an excerpt of a photometry logging file.

magnitudes and S/N ratios:

```
-----
[1]: object, [2]: magnitude, [3]: magnitude error, [4]: instrumental error,
[5]: comparison object, ([6] measured magnitude inbetween x-sigma)
src    14.2761  0.0401  0.0022  B
src    14.2605  0.0501  0.0022  C
src    14.2943  0.0601  0.0022  H
B      11.9744  0.0500  0.0006  C  0.2
B      12.0082  0.0600  0.0006  H  0.2
C      13.8056  0.0400  0.0016  B  0.3
C      13.8237  0.0600  0.0016  H  0.4
```

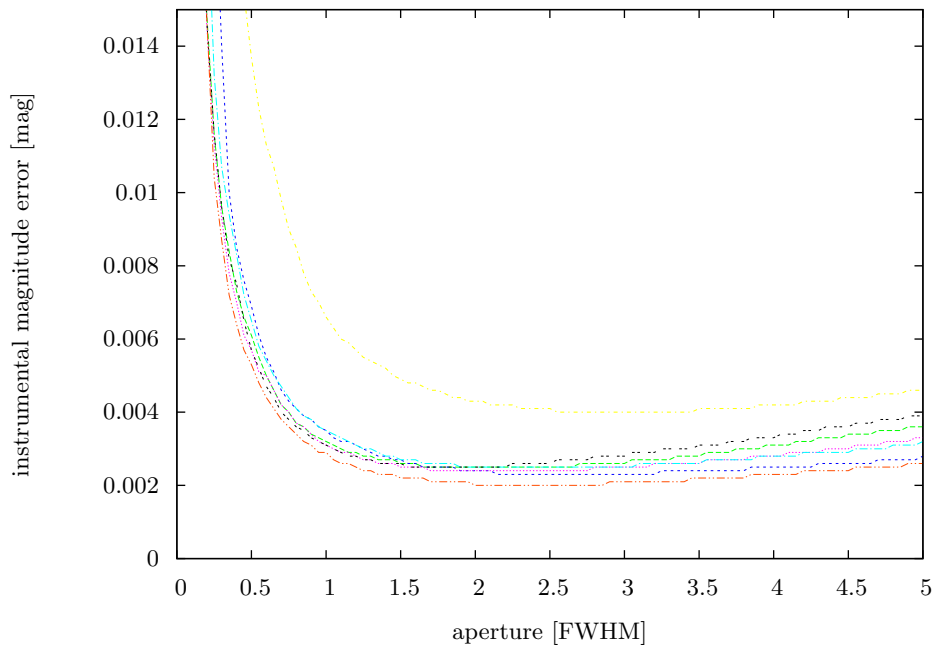


Figure 6.3: Instrumental error as a function of aperture diameter (different graphs correspond to different measurements of 3C 66A of the October/November run 2008, used comparison stars: 'B' and 'C2')

H	13.7118	0.0400	0.0015	B	0.3
H	13.6963	0.0500	0.0015	C	0.5

The excerpt shows a measurement of the object of interest ('src') using three comparison objects: 'B', 'C' and 'H'. The magnitude of 'src' is determined using each comparison object separately, as well as the magnitude of each comparison object using the other ones. The last column (only for comparison objects) shows the residual of the determined and real magnitude displayed in multiples of the rms error of the comparison object. Tests showed that measurements with residuals smaller than approximately  $3\sigma$  show very good accuracy. Higher residuals may be passable in single cases. Such may occur if cosmics or other image artifacts are involved or if comparison star magnitudes scatter over a too large range.

The highest of the residual values is also displayed in the resulting `tablefile` for convenience.

### 6.3.2 Best Aperture Determination

The choice of aperture size is an important question. As already discussed in 6.1, a large aperture includes the majority of an objects flux but does not lead to the best result. In this case the large aperture area increases the noise term (Eq. 2.5) and therefore leads to a larger error. On the other hand, small apertures are prone to centering errors.

The best aperture size is defined by showing the smallest possible error of the magnitude. Tests to determine the best aperture size were performed using different SPM data sets. As a test routine aperture photometry was performed using elliptical apertures of different sizes. Results for

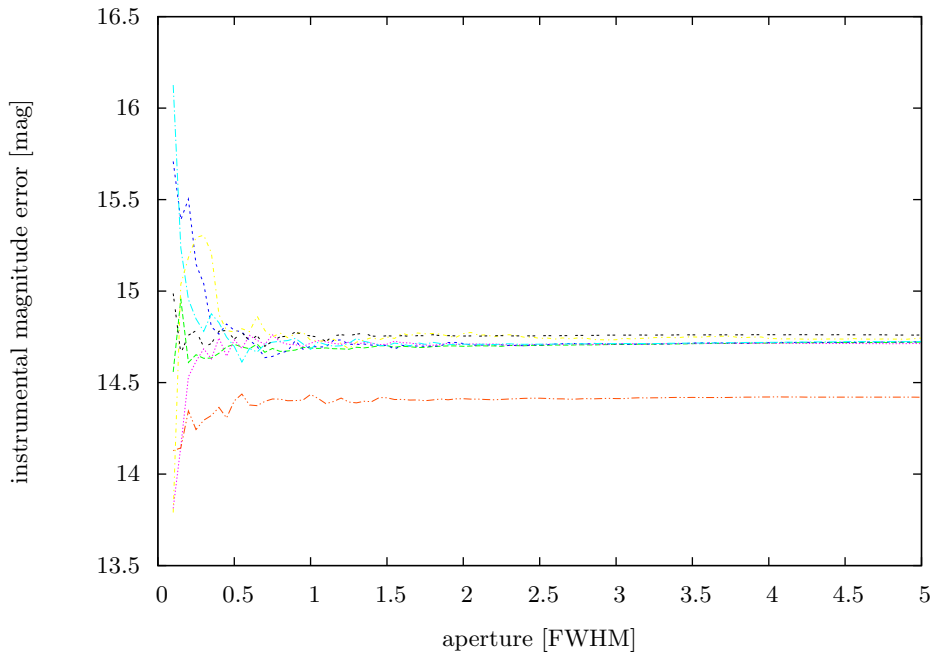


Figure 6.4: Insensibility of the magnitude regarding aperture diameters (different graphs correspond to different measurements of 3C 66A of the October/November run 2008, used comparison stars: 'B' and 'C2')

several sets are similar and are visualized exemplarily in Fig.6.3. The graph shows the instrumental magnitude error as a function of the size of the major axis of the ellipse expressed in FWHM of the objects PSF. Several curves are drawn standing for different image sets taken on different days.

It is clearly visible that the error shows a global minimum for major axis in the region between 2.0 and 2.5 FWHM approximately. This perfectly agrees with [Mig99] and other authors who suggest an aperture diameter of 2 FWHM of the objects PSF.

The insensibility of the magnitude determination as a function of the aperture size is displayed in Fig. 6.4. The graph shows no significant variations in magnitude for aperture diameters larger than 1.5 FWHM. Hence, the best aperture size is not determined by magnitude but by the smallest error, as stated before.

All tests mentioned above explicitly use elliptically shaped apertures. Tests were done using circular apertures, too. Results are similar. However, a circular aperture of a certain diameter incorporates a larger area than an elliptic aperture with a major axis of the same length. Therefore, the error of the measurement is slightly smaller.

### 6.3.3 Conclusion

dophotometry produces reliable and good results if used properly. The use of fitting elliptic apertures is recommended. Aperture diameters should be in the range of 2.0 to 2.5 FWHM.

However, results should be checked for outliers in magnitude and calculated comparison object residuals.

## 6.4 Photometry Results

In order to show the functionality of the `dophotometry` script, a number of data sets have been analyzed. They are introduced in the following sections.

Each graph is splitted into two parts: the upper part (red line) shows the magnitude as a function of time including error bars in both. The lower part (green line) displays the compstar residual, i.e. the mean residual of one comparison object in respect to all other comparison objects and its rms error (cf. Eq. 6.1). It is a visual aid to judge the quality of the measurement.

Some of the SPM data are going to be published in papers by other authors. Mainly photometric data are involved here. The publications so far are

- *AGILE detection of a rapid gamma-ray flare from the blazar PKS 1510-089 during the GASP-WEBT monitoring* by F. D Ammando et al., to be published in *Astronomy & Astrophysics*

Other publications are in progress.

### 6.4.1 Results of the October/November Run 2008

Some results of the October/November observing run in 2008 are shown in Fig. 6.5 to 6.10. Each object is part of the high priority list.

**3C 66A** shows a quick rise in brightness around Nov, 3rd (Julian Date 2454773) of nearly 0.4 magnitudes. Since there was only one usable comparison object in the field-of-view, no residual of comparison objects could be calculated (green line).

**OJ287** and **BL Lacertae** are known for their optically violent behaviour. BL Lacertae shows a general rise in brightness and fluctuates over 0.6 magnitudes. At least two comparison stars are available here. Therefore, a residual of real and calculated magnitude of the comparison star could be computed and shows a good data quality.

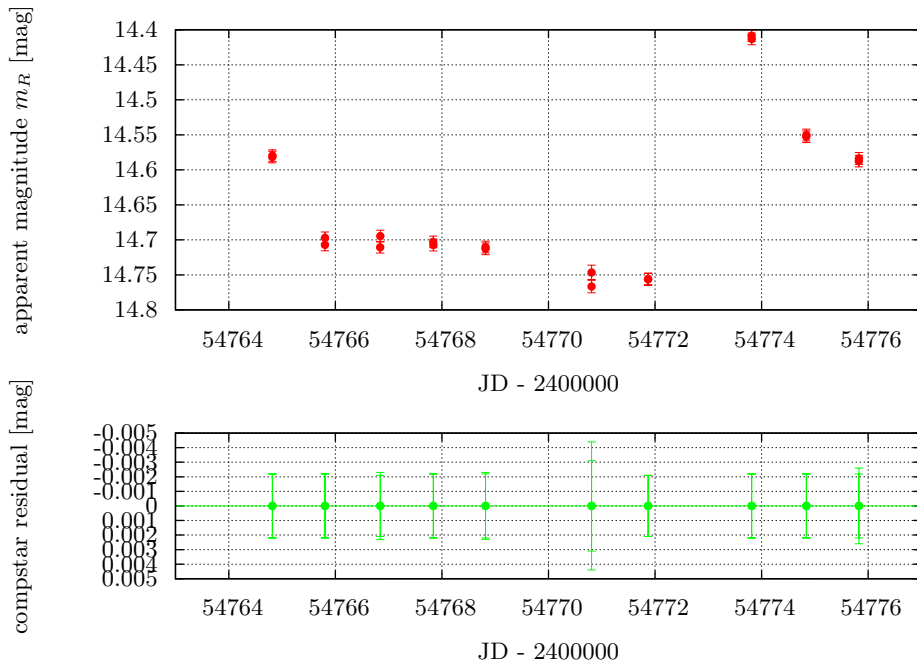
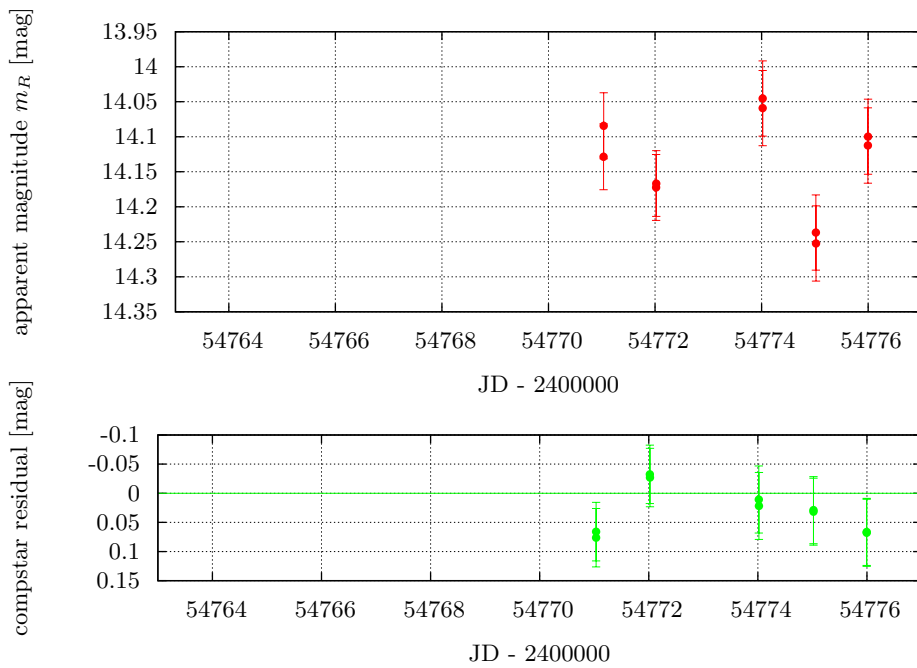
As part of the high priority object list, each object was imaged using a full cycle, i.e. two complete polarimetric measurements using each polarimeter adjustment angle. Therefore, each measurement is displayed by two measurement points - one for each complete polarimeter angle sequence.

**1ES 0647+250** shows a relatively calm behaviour. All measurements show a negative compstar residual, which is the result of having an inappropriate set of comparison objects: one star of 15.2 mag and three others around 13.4 mag while the object has a brightness of approximately 16.0 mag.

The large errorbars of **PKS 2155-304** lead to doubt, whether the brightness variations measured are real or just statistical variations.

**S4 0954+650** is presented here since it is one of the faintest objects of the object list. The comparison star residual show little variations, which are believed to be of statistical nature and lie within a one-sigma area. Therefore, the measurements are believed to be reliable. This shows that photometric measurements of faint objects are possible with the existing setup. Results of the still fainter object PKS 0528+134 are displayed in Fig. B.19. The comparison residual for this object is even larger than  $3\sigma$ . The results of such faint object can be doubted.



Figure 6.5: Photometric Results of **3C 66A** of the October/November Run 2008Figure 6.6: Photometric Results of **OJ 287** of the October/November Run 2008

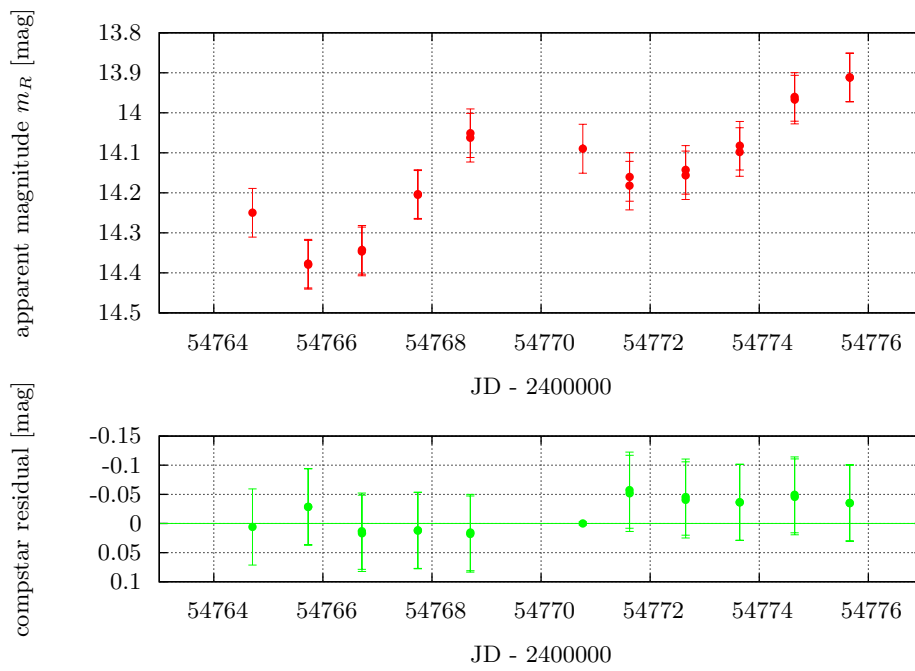


Figure 6.7: Photometric Results of **BL Lacertae** of the October/November Run 2008

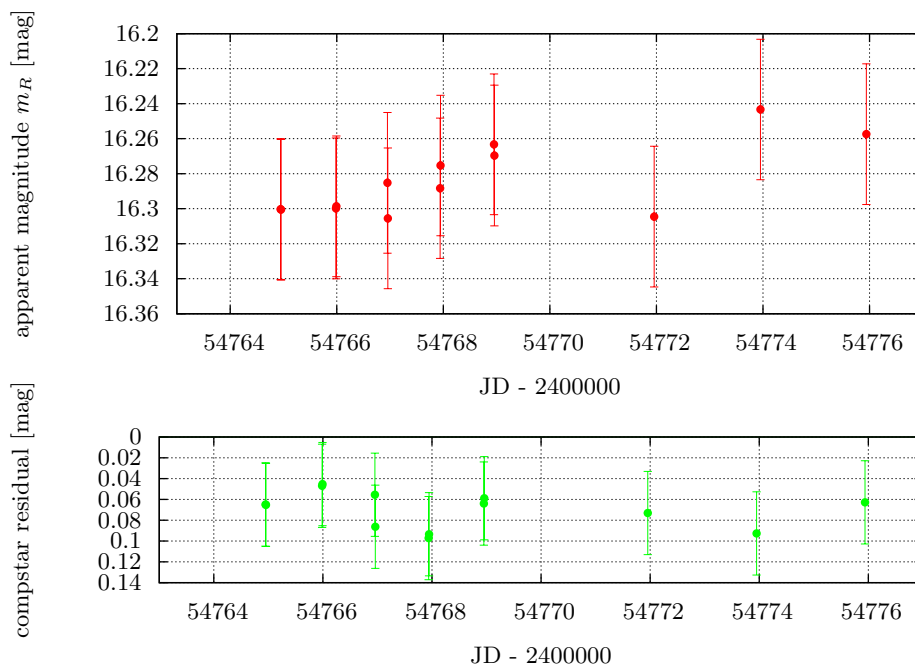


Figure 6.8: Photometric Results of **1ES 0647+250** of the October/November Run 2008

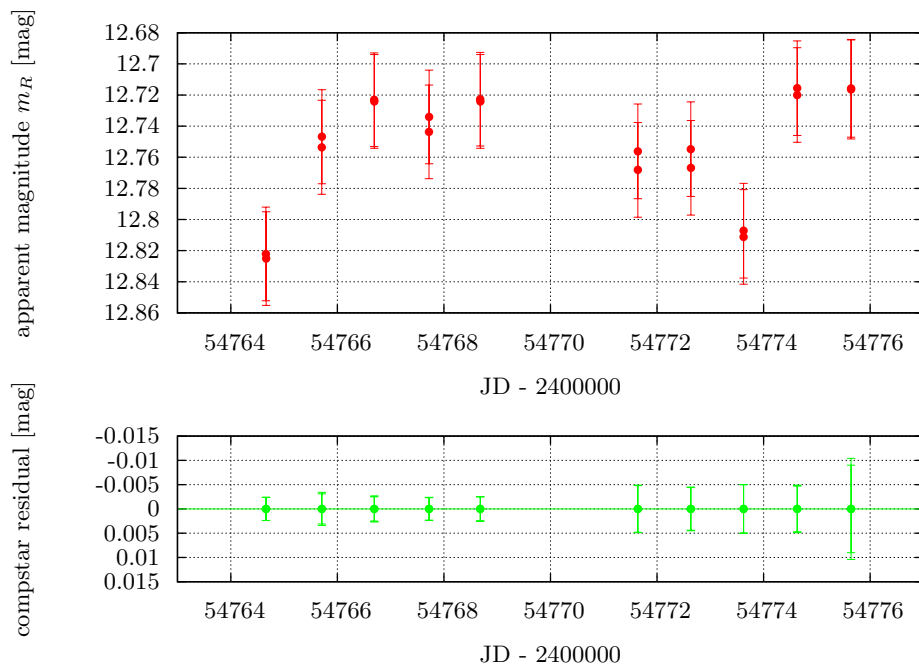


Figure 6.9: Photometric Results of **PKS 2155-304** of the October/November Run 2008

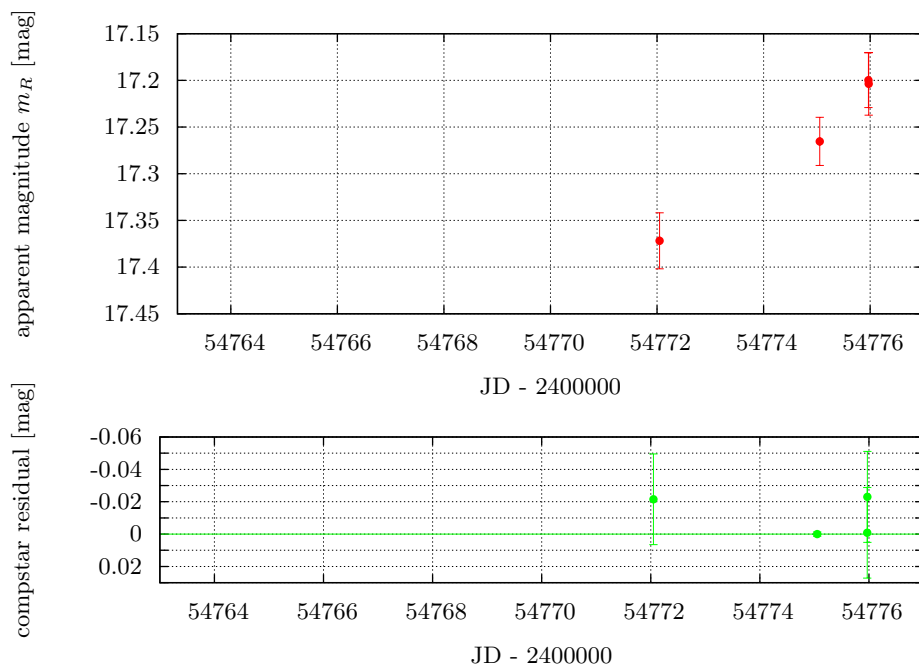


Figure 6.10: Photometric Results of **S4 0954+650** of the October/November Run 2008

Remaining data of this run can be found uncommented in B.1.

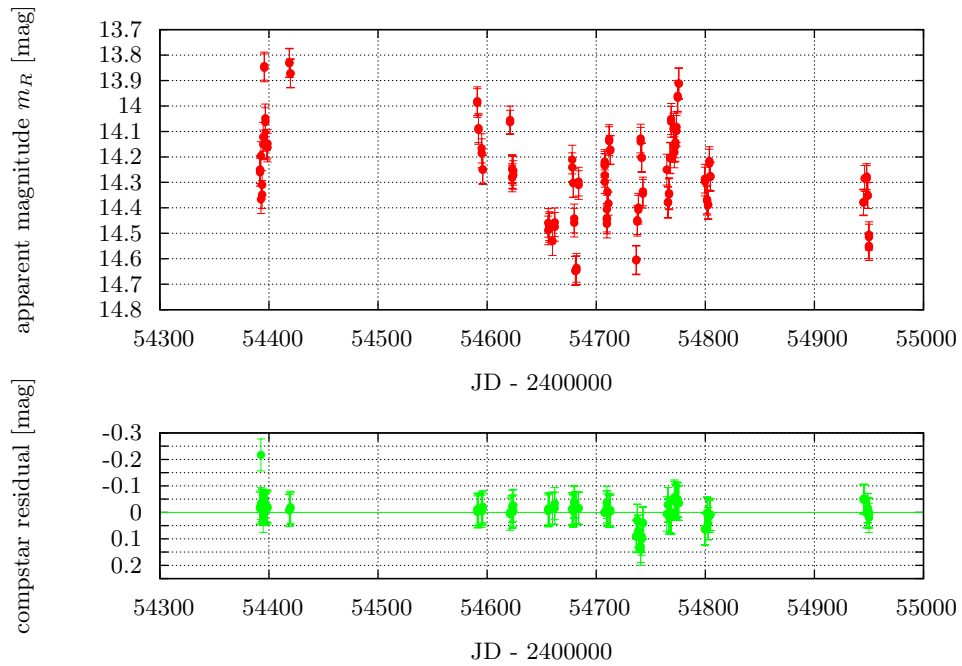
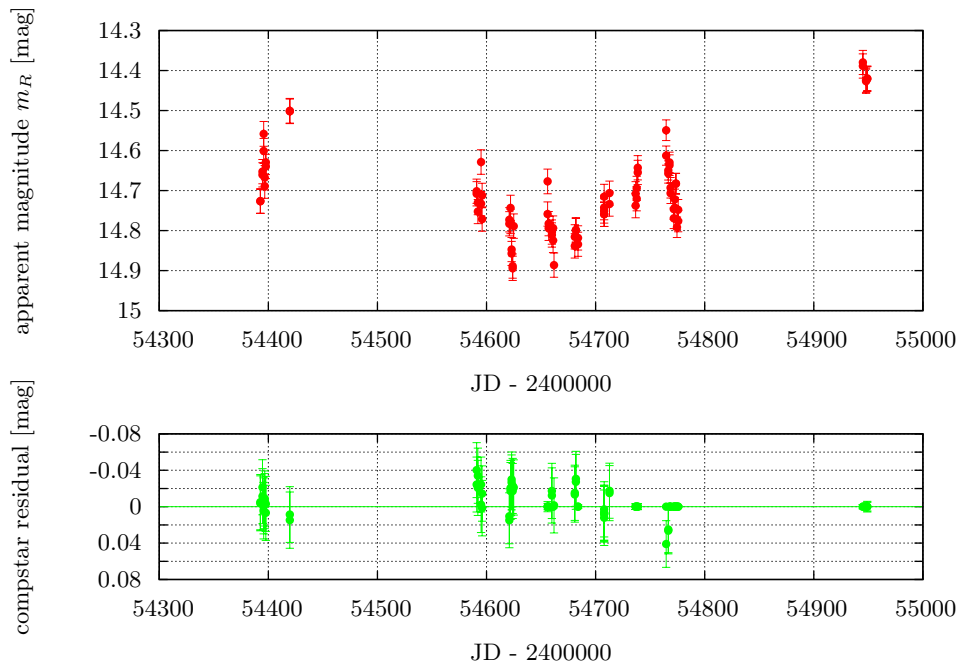
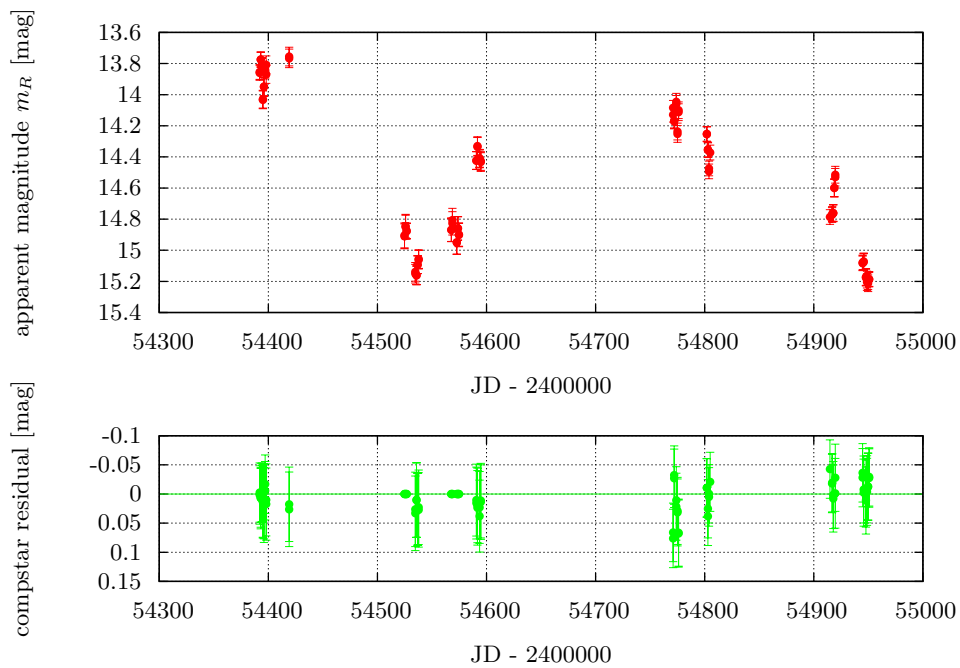


Figure 6.11: Photometric Results of **BL Lacertae** over all Runs

#### 6.4.2 Long-term Results of BL Lac, 1ES 1959+650 and OJ 287

The high degree of optical variability of some source gets clearly visible when observed over a long period. Data of all runs completed until April 2009 of the three objects mentioned above have been analyzed and are visualized in Fig. 6.11 to Fig. 6.13. They all show a certain degree of optical variability and a more or less violent behaviour.

Figure 6.12: Photometric Results of **1ES 1959+650** over all RunsFigure 6.13: Photometric Results of **OJ 287** over all Runs

# Chapter 7

## Polarimetry

Performing polarization measurements is a highly delicate task. Unlike photometric measurements, not only fluxes from a single image are measured but from a set of four images. The next sections demonstrate the importance of making these observations under exactly the same conditions.

*The first section gives an introduction on how to perform polarization measurements from CCD data and the `dopolarimetry` script created for this reason. Furthermore, the measured polarization angle is calibrated and the existence of an instrumental polarization and some possible origins of error are discussed. The last section presents some results of polarization measurements of the October/November 2008 observing run.*

### 7.1 Polarization Measurements

To perform polarization measurements, a number of four images per object is mandatory. Each of them has to be taken using a different polarimeter setup angle. A widely spread set of angles used for this purpose is  $0^\circ$ ,  $45^\circ$ ,  $90^\circ$  and  $135^\circ$ . The sequence itself has no impact on the measurement - disregarding influences of varying sky transparency. Information on the imaging process are given in 3.2. Object fluxes of each image are obtained according to photometric measurements. After calculating the Stokes parameters using Eq.2.9, the polarization degree and angle follow from Eq.2.10.

Although the determination of both quantities is a straight forward calculation, the result strongly depends on the proper measurement of the fluxes and the data quality. This is discussed in 9.

To obtain meaningful polarization data, one has to determine the rotational angle between the CCD detector and a predefined positional angle in the sky. Furthermore, the instrumental polarization has to be determined. This follows after the introduction of the polarimetry script, which is used for data analysis.

## 7.2 Polarimetry Script - dopolarimetry

Since polarimetric measurements demand flux determinations similar to photometric measurements, the script is based on the photometry script `dophotometry` (cf. 6.2). Many routines have been used again and task parameters as well as the first part of the task description are quite similar. The most significant difference is the treatment of measured fluxes to calculate polarization degree and angle using Eq. 2.9 and 2.10.

### 7.2.1 Parameters

`images = "*.fits"`                      `images to be used`

Images to be analyzed. Wildcard-symbols like the asterisk or question mark may be used. Polarimetric input images have to include the same number of images for each of the four polarimeter angles to avoid polarization effects.

`(srcstring = "src")`                      `object name to measure`

Designation of the source of interest used in the reference-magnitude-file. The Polima pipeline only uses the string 'src'. Other user-defined strings may be possible.

`(fitapertur = no)`                      `use a fixed circular aperture?`

`(ellipticfit = no)`                      `if fitting, use an ellipse?`

If `fitaperture` is set to 'no' a circular aperture is used with a fix aperture diameter. In this case the parameter `ellipticfit` has no meaning. However, if `fitaperture` is set to 'yes' the aperture is fitted to the objects image. The shape of the aperture depends on the parameter `ellipticfit`:

- `ellipticfit = yes`: a polygonal aperture of elliptical shape is fitted; the polygon has 12 vertices and is fitted using the objects FWHM, ellipticity and position angle
- `ellipticfit = no`: a circular aperture is fitted using the objects FWHM as diameters

`(aperture = 30.)`                      `full aperture in px or multiple FWHM`

Inner aperture radius for aperture photometry. The scale and meaning of this parameter depends on the settings of `fitaperture`:

- `fitaperture = no`: `aperture` means the full diameter of a circular aperture in pixels
- `fitaperture = yes`: `aperture` means the full diameter of a circular or the major axis of an elliptical aperture, respectively, measured in FWHM of the object image

`(minapradius = 5.)`                      `minimum aperture radius in px`

`(maxapradius = 50.)`                      `maximum aperture radius in px`

Both parameters define the range of allowed aperture radii in pixels. The intention is to limit the size of the aperture in case of crowded fields and provide a minimum aperture size. Please give attention to the fact that these parameters define a radius while `aperture` defines the diameter of the aperture.



---

```
(vignetting = 1.)                use multiple radius of unobscured field
```

Image regions close to the edge of the CCD are subject to obstruction due to the polarimeter device. In order to have proper photometry results only objects are used which are completely unobstructed (cf. 5.3.3). Sometime objects are located at the rim of the unobstructed circular area. If the user wishes to increase the radius of the usable area he has to increase the **vignetting** parameter by a small portion. It represents a factor which is multiplied to the radius of the unobstructed area.

```
(writetotable = no)              write result to table?
  (tablefile = "result.tab")     result table file
```

If **writetotable** is set to 'yes' the results of the analysis are written to the file **tablefile** in table form. This allows a quick access to analysis results for further processing.

```
(imagelist = "no entry here")   internal list variable
  (tables = "no entry here")    internal list variable
```

These parameters have no meaning for the user but have to be initialized here.

## 7.2.2 Description

First, internal parameters and arrays are initialized and a check for necessary IRAF packages is performed. After that, the **apphot** package is initialized which is needed to run included tasks properly. Some settings may be changed again later. Eventually, a file is created containing all image-filenames to be processed. This list is successively run through. The next steps are done for each image separately.

Important FITS header descriptors and detector dependent settings are read in for later image handling. In order to have accurate object center positions, the coordinate-file is read in and object positions are reestimated using the **apphot.center** task. The reference-magnitude-file is only used to find out which entry of the coordinate-file corresponds to the source of interest. The applied photometry method depends on the parameter **fixedaperture**:

If **fixedaperture = yes**, a circular aperture of fixed size is used for flux determination. Its diameter in pixels is determined by the parameter **aperture**. Flux determination is performed by the **phot** task of the **apphot** package.

In the case of **fixedaperture = no** there are two possible methods:

If **ellipticfit = no**, the FWHM of objects listed in the coordinate-file is measured and averaged. The applied aperture diameter equals the number given by **aperture** multiplied with the mean FWHM if in the limits of **maxapradius** and **minapradius**. Flux determination is then performed by the **phot** task.

Otherwise if **ellipticfit = yes**, FWHM, ellipticity and position angle of all objects in the coordinate-file are measured and averaged. According to the **dophotometry** script, 12 vertices of a polygon approximating an ellipse are determined and saved to a file. Flux determination is here performed using the **polyphot** task of the **apphot** package.

The results of each flux determination method are written to a text file named after the image

filename with the suffix '.mag' containing all results of the aperture photometry for each object contained in the coordinate-file. For each method of flux determination, the sky background annulus is determined the same way: its inner radius equals 3 aperture radii with a thickness of 3 aperture diameters. This provides a sufficient number of pixels for proper sky background estimation. The resulting value equals the median of the pixel value distribution.

Before calculations starts, each object is checked to be inside the obstruction free area of the image (cf. 5.3.3). Objects outside this area or on the edge are not used in the further process. Polarimetric data and all following calculation steps are written to the logfile to enable transparency and allow the user to follow each step.

The following steps are applied if all images have been processed. Furthermore, they differ from data handling in the `dophotometry` script.

Results of the flux determinations are exported to a table file (image filename'.tbl'), namely: object flux error ('STDEV'), number of pixels inside the aperture ('AREA') and flux ('FLUX'). The file contains one line per object. Outsourced data are read into arrays for quick access. Fluxes are corrected for airmass variations (cf. 2.3.3). To have a quality measurement, the fluxes of each comparison object over all polarimeter angles are summed up, too. This gives the total flux  $I$  of these objects. Comparison of their cumulated fluxes between different polarimetric measurements allow to judge over the sky transparency (e.g. cloudiness)

Before starting calculations, the number of images for each polarimeter angle is checked to be equal. Following, fluxes, areas and errors of the source of interest are summed up in respect to the polarimeter angle. These numbers are used to calculate the SN-ratio using Eq. 2.5, the Stokes parameters (Eq. 2.9) including errors (Eq. 2.12) and the polarization degree and angle including errors (Eq. 2.10 and 2.11, respectively). Polarimetric measurements of low SN-ratio are biased due to the quadratic term leading to the polarization degree. To correct for this bias, a simplified model created by [SS85] is applied: the measured polarization degree  $P_{\text{meas}}$  and its error  $\sigma_{\text{meas}}$  are used to calculate an approximation for the unbiased polarization degree  $P_0$

$$P_0 = \sqrt{P_{\text{meas}}^2 - 2 \cdot \sigma_{\text{meas}}^2}$$

The polarization angle is determined in a way that resulting values range between  $0^\circ$  and  $180^\circ$ . After calculating the mean time of exposure (cf. `dophotometry`), results are printed on the screen and written to `tablefile`, if wanted.

The entry of the `tablefile` contains the following data, seperated by tabulars:

- polarization degree (in percent)
- error of the polarization degree (in percent)
- polarization angle (in degree)
- error of the polarization angle (in degree)
- Stokes parameter  $I$ , normalized to 1 s integration time
- error of  $I$

- Stokes parameter  $Q$ , normalized to 1 s integration time
- error of  $Q$
- Stokes parameter  $U$ , normalized to 1 s integration time
- error of  $U$
- mean time of exposure
- error of the mean time of exposure (represents half of the total measurement time)
- string containing the normalized fluxes (regarding exposure time) of the available comparison objects
- list of applied aperture diameters (in pixels) for each image

### 7.2.3 Testing

The `dopolarimetry` task was tested using different data sets from SPM observations. The routine shows a robust handling. Results are reproducible and comparable to those of other SPM members.

#### Scatter of Results

However, polarimetric results - unlike photometric ones - show a certain amount of scatter which often exceeds  $3\sigma$  uncertainties. Reasons for this circumstance are numerous and discussed in 9.4.1.

Tests show that polarimetric measurements are highly reliant on proper flux determination, i.e. aperture sizes. For this reason, the `dopolarimetry` task was applied using circular apertures of different diameters. Fig. 7.1 shows the measured polarization degree as a function of aperture size<sup>1</sup>. The graph shows lines of different color representing different measurements. Measurements were taken at different days, hence the polarization degree varies between the measurements (i.e. lines). It is clearly visible, that the measured polarization degree highly depends on the applied aperture size. Strong variations in the range of small apertures are a result of incomplete flux measurements, i.e. only a fraction of the real flux is measured. Therefore, high polarization degrees appear. In the range of 4 to approximately 6 FWHM most measurements show a plateau, i.e. the polarization degree varies on a small scale only. For larger apertures, results diverge due to the inclusion of neighboring objects fluxes.

Therefore, aperture diameters ranging from 4 to 6 FWHM are recommended in this case. The actual range may vary between different data sets depending on seeing, focus and tracking accuracy. Hence, it is not possible to give a good guess and the user is asked to find the best aperture size.

Furthermore, a significant impact of aperture shape can be observed. Different from photometric measurements, where elliptical apertures lead to better results (smaller errors) due to smaller aperture areas, polarimetric measurements show better results using circular apertures, i.e. the scatter in polarization degree and angle are limited to a smaller range. An explanation for this

<sup>1</sup>used data: 3C 66A of the October/November run 2008

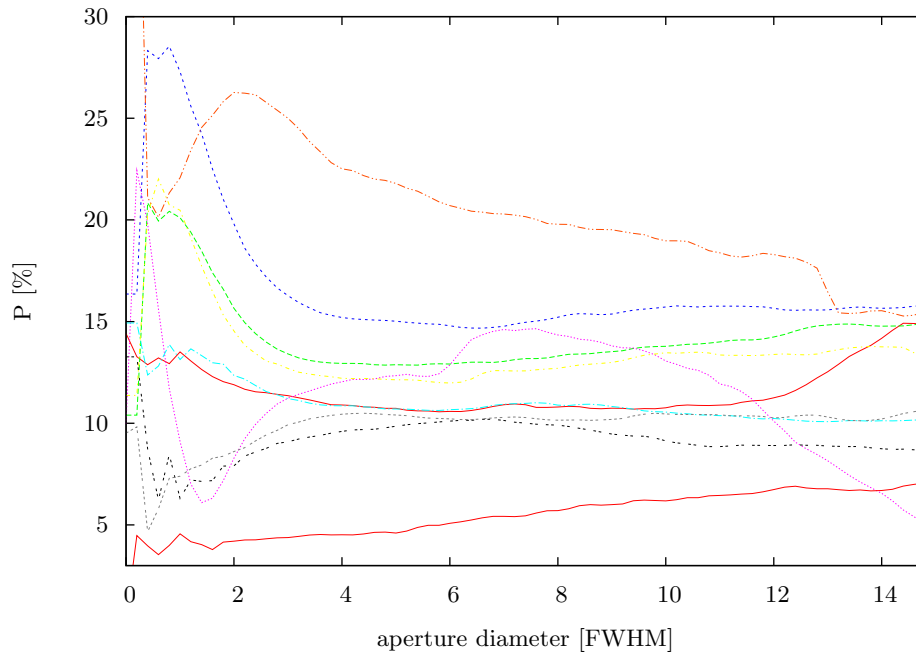


Figure 7.1: Polarization degree as a function of aperture diameter (lines of different color refer to different measurements taken on different days)

observation may be, that polarimetric measurements are highly prone to improper flux measurements. Photometric measurements do not suffer from measuring only a fraction of an objects flux, since the same fraction of flux is measured from each comparison object. The reason for this fact is that all objects are located on the same image. Even if using several images there is no impact, since the determined flux fraction is equal on each image and the fluxes of all images are summed up. In polarimetric measurements, however, fluxes are not just summed up but run through more complicated equations. It is crucial to measure in each image the same fraction of flux. This is achieved by collecting the most possible fraction of flux and therefore using a large aperture area, i.e. a circular aperture of sufficiently large radius. This corresponds to the plateau range in Fig. 7.1. Too large apertures, however, lead to the inclusion of neighbored objects fluxes and bad results.

**Conclusion** To limit the scatter of polarization degree and angle, it is highly recommended to use circular apertures of sufficient radius to include the highest possible fraction of object flux. This can be achieved by using a multiple of the objects FWHM (`'fitaperture = yes'`) or by using a fix aperture diameter (`'fitaperture = no'`). In order to avoid the inclusion of surrounding objects, the maximum radius of the aperture should be limited using `maxapradius`.

### Measures of Quality

In order to be able to judge the quality of polarimetric measurements, the flux of each comparison object available on each of the input images is summed up separately. The normalized sums (according to exposure time), which represent the total flux (Stokes parameter  $I$ ), are written to

the `tablefile`. To have sufficient image quality, the flux of one object should not vary more than  $3\sigma$  (with  $\sigma$  being the square-root of the flux as an estimation) from the maximum flux of all measurements.

The approach is explained using an example:

```
11.542 ... B:24073.221191925;C:4976.930328272;H:5299.2259794325; ...
10.722 ... B:24084.921638177;C:4976.0634211814;H:5279.0420048054; ...
22.985 ... B:22704.420961304;C:4385.4345272963;H:4770.0475445711; ...
14.274 ... B:24388.323384403;C:4701.886441319;H:5125.4822491278; ...
```

This is an excerpt of a `tablefile` containing the results of a set of polarimetric measurements. The first column represents the polarization degree, the second one the cumulated fluxes of comparison objects. Other columns have been removed. Each line represents one measurement. As can be easily seen, the fluxes of all four comparison objects of the third measurement is significantly lower leading to a much to high polarization degree. Therefore, this measurement can be ignored. The decrease in flux may be the result of an increased cloud coverage during the integration.

Minor deviations of cumulated fluxes over several measurements may be explained by poor transparency or scattered moon light. The interpretation of maximum deviations is the users task. Using a  $3$  or  $5\sigma$  range usually leads to good results.

## 7.2.4 Polarization Angle Calibration

In order to obtain meaningful polarization data, one has to account for the rotation of the CCD detector relative to a predefined position angle. This rotational angle  $\Delta\Theta$ , which is the difference between the real polarization angle  $\Theta_{\text{real}}$  and the observed one  $\Theta_{\text{obs}}$  can be measured using highly polarized (= highpol) standard stars. These stars show a static polarization of their light in time and polarization angle due to strong magnetic fields. The polarization degree lies around 4% to 8%.

The rotational angle  $\Delta\Theta$  is defined by the relation

$$\Delta\Theta = \Theta_{\text{obs}} - \Theta_{\text{real}} \quad (7.1)$$

A set of highpol standard stars is part of the target list (cf. A.2). To estimate the rotational angle, all measurements of highpol standards have been taken into account including the observing run of April, 2009. Three stars show a significant number of measurements and are therefore used for calibration: **HD 155197**, **HD 204827** and **VI Cygni**. In order to prevent disturbing influences on the polarization measurement due to moving clouds or other, only selected data were used in the further process.

**Data selection** It is hard to have a detailed record of the sky coverage during a night. It is practically impossible to log the cloud situation for every single image. However, logging provides a reliable overview over the night's weather situation.

In order to have a measure for the momentary transparency during one measurement, one needs an objective indicator. Large observatories use complementary observations of standard stars during a measurement for this reason. During a clear night, the flux of the standard star

Table 7.1: Results of the polarization angle calibration using highpol stars

Object	$P_{\text{obs}}$ [%] (median)	$P_{\text{real}}$ [%]	$\Theta_{\text{obs}}$ [°]	$\Theta_{\text{real}}$ [°]	$\Delta\Theta_{\text{mean}}$ [°]
HD 155197	$4.2 \pm 0.5$	$4.27 \pm 0.03$	$11 \pm 2$	$102.9 \pm 0.2$	$-91.88 \pm 2$
HD 204827	$4.7 \pm 0.4$	$4.89 \pm 0.03$	$151 \pm 2$	$59.1 \pm 0.2$	$91.9 = -88.1 \pm 2$
VI Cyg	$8.4 \pm 0.3$	$7.89 \pm 0.04$	$25 \pm 1$	$116.2 \pm 0.1$	$-91.23 \pm 2$

appears to be constant. If the night is cloudy, the flux varies. SPM does not offer such a facility. However, a similar estimation can be provided by the polarization measurement itself, since the total flux is the sum of the four fluxes obtained in the four expositions using different polarization angles. Hence, total flux is expressed by the Stokes parameter  $I$  (2.9). In order to check for a clear sky or at least a static transparency during one exposition, one has to compare the parameter  $I$  of this measurement with the same parameter of another measurement of the same object. Since cloudiness can vary during a short timescale, it is suggested to use full cycle measurements, i.e. two measurements taken successively.

For this reason, only full cycle sequences are used in the following analysis process. The total fluxes  $I$  of both measurements are subtracted from each other and compared with the mean error of both  $I$ . To have a good estimation of the data quality, only successive measurements with a residual total flux of smaller or equal to  $3\sigma$  are used further. This leads to a total number of 12 data points for HD 155197, 20 for HD 204827 and 12 for VI Cygni.

**Results** Figures 7.2 to 7.4 show the polarization degree  $P$  and the observed polarization angle  $P_{\text{obs}}$  of these data points plotted. Each graph also shows the expected polarization degree and the median of the measured distribution as well as the median of the measured polarization angles.

The plots show a high level of scattering which exceeds error limits. The origin of this scattering is not clear and will be discussed in 9.

Table 7.1 shows the determined values of polarization degree and angle and the real values according to literature values taken from the SPM homepage. The last column represents the mean rotational angle of the CCD calculated using relation 7.1 and the complete data set from all observing runs. Following the definition, one gets two negative and one positive angle. Due to the ambiguity of the polarization angle, it can be transformed into a negative value by subtracting it from  $180^\circ$ . This conserves the physical meaning of the angle.

All determined values are medians due to the high degree of scattering in polarization degree and angle.

As a result, one receives a mean rotation of the CCD of

$$\Delta\Theta = (-91 \pm 2)^\circ \quad (7.2)$$

with respect to the the sky plane alignment. The error of the angle is relatively large compared to that of a single measurement. It is caused by a high level of scattering, which can be seen in the polarization degree as well as in the polarization angle.

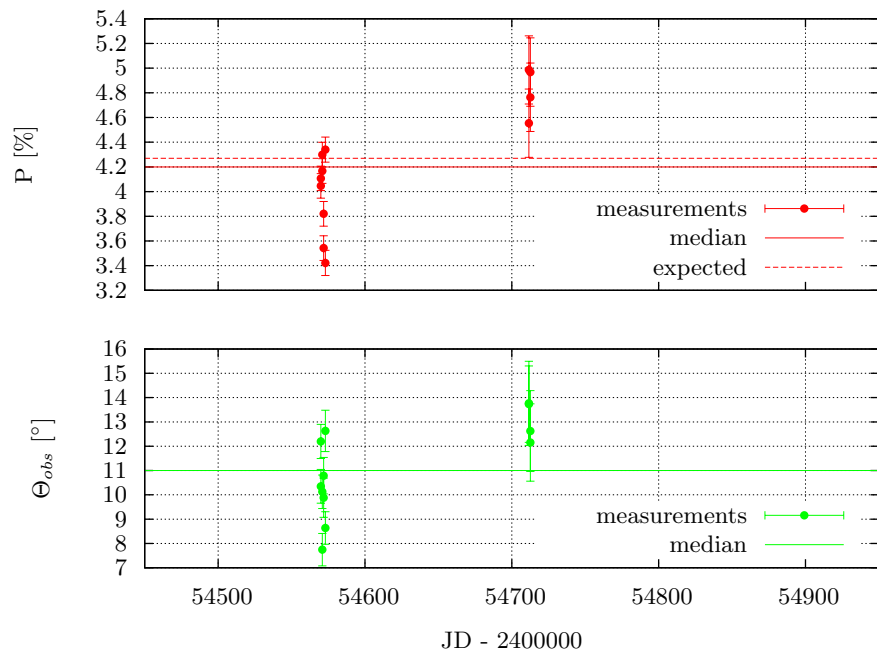


Figure 7.2: Polarization Measurements of HD 155197 ( $3\sigma$ -selected measurements)

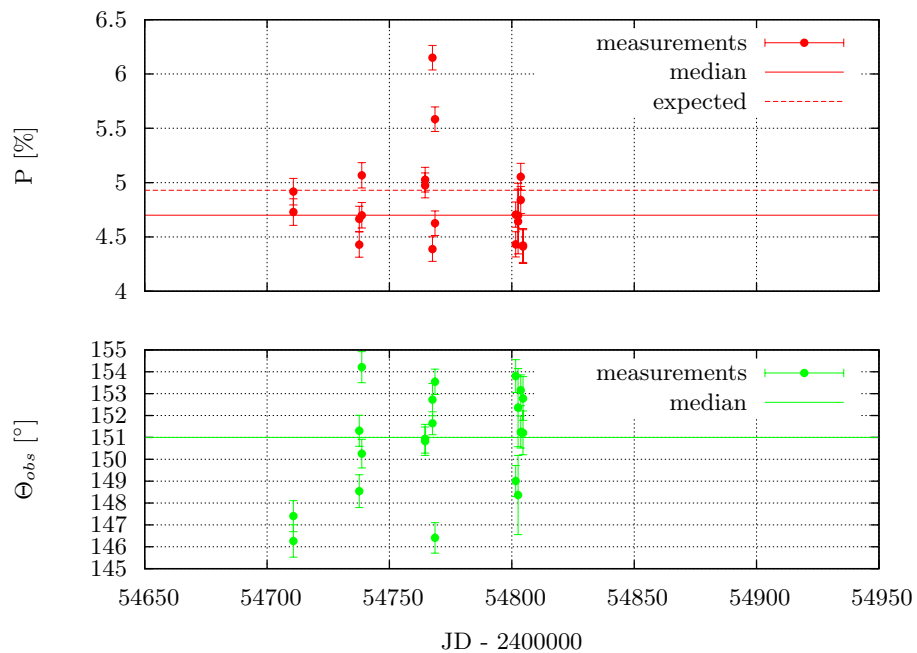


Figure 7.3: Polarization Measurements of HD 204827 ( $3\sigma$ -selected measurements)

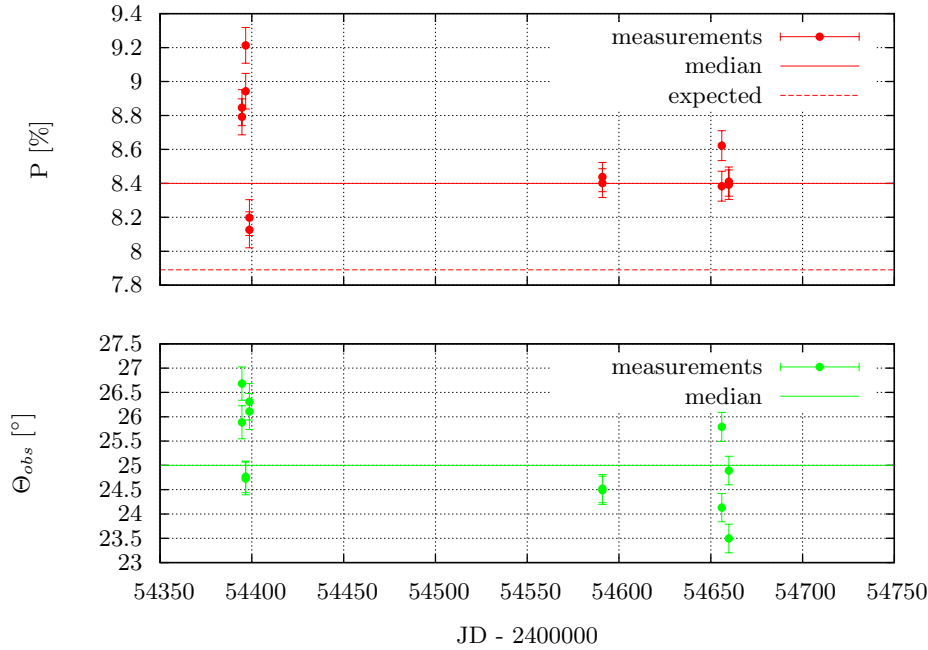


Figure 7.4: Polarization Measurements of VI Cyg ( $3\sigma$ -selected measurements)

**Less strict data sets** All preceding calculations were done using selected data, i.e. data with total flux (Stokes parameter  $I$ ) variations smaller or equal to  $3\sigma$  (with  $\sigma$  being the error of  $I$ ). This selection process is mandatory to assure an adequate data quality. On the other hand, it limits the number of usable measurements. To have a comparison of results using a less strict selected data set, all calculations above have been redone with data characterized by flux variations smaller or equal to  $10\sigma$ .

As a result of the less strict selection process the number of data points of all three objects in sum doubled from 44 ( $3\sigma$ -selected) to 88 ( $10\sigma$ -selected), improving statistics. At the same time, the data quality is expected to decrease by allowing higher flux variations.

A comparison of the  $3\sigma$ - and  $10\sigma$ -selected data sets show a perfect match of the results, i.e. of the mean rotational angle and polarization degrees of the standard stars. The only difference is a slightly larger error of the former one. Both influences, decreased data quality and improved statistics, seem to balance each other.

As a conclusion one can state that a less strict selected data set leads to - carefully spoken - comparable results. In this case, the matching is nearly perfect, which might be an exception. Using a larger but less qualitative data set is surely a good approach. Even higher  $\sigma$  values might be possible, since outliers show large flux variations of several tens of  $\sigma$ .

**Stability of the rotational angle** The resulting rotational angle is a mean, i.e. calculated from data of all observing runs so far. One might oppose that the rotational angle might change from one observing run to the next since the POLIMA device is removed from the telescope after each run. As a result of reattachment, the rotational angle might slightly differ from that one of the precedent run. Actually, one can measure variations of the rotational angle between the observing



Table 7.2: Variations in the CCD's rotational angle between different observing runs

Run	$\Theta_{\text{hi960}} [^\circ]$	$\Theta_{\text{vicyg}} [^\circ]$	$\Theta_{\text{h2048}} [^\circ]$
Oct. 2007	$142.5 \pm 1.2$	$26.6 \pm 0.4$	$149.8 \pm 1.4$
July/Aug. 2008	$146.0 \pm 1.2$	$26.8 \pm 0.4$	$147.8 \pm 0.7$
residual	$-3.5 \pm 1.7$	$-0.2 \pm 0.6$	$+2.0 \pm 1.6$

runs.

Some data of the highpol standard stars *Hiltner 960*, *VI Cygni* and *HD 204827* of two runs are listed in table 7.2 to represent this variations. These data were selected for the reason that these three objects were measured in both runs. There is no other data set with three or more highpol standard stars measured in the same two runs. The data are part of the  $10\sigma$ -selected data to have a sufficient number of data points.

Obviously, the polarization angle errors of one single run are smaller than the calculated one for the mean (i.e. data of all runs combined). This might speak for a calculation of the rotational angle for each run separately. On the other hand, creating the residual of the rotational angle for each object between the two runs as done in the last line of Tab. 7.2 does not show a clear trend and varies in both, positive and negative directions. This means, it is not possible to detect a homogeneous variation of the rotational angles of both runs. Hence, the variations detected here are caused by statistical scattering and have no systematic contributions. Inbetween the error limits, there is no rotation of the CCD between these two runs.

This justifies the use of a mean rotational angle instead of a rotational angle determined for each run separately.

### 7.2.5 Instrumental Polarization

In order to find a possible instrumental polarisation, a set of zero-polarized (= zeropol) standard stars is observed. These show a minor but static polarization degree of smaller or equal to 0.2% roughly, which is therefore negligible.

Instrumental Polarization is created by the telescope optic itself and other influences. Due to grazing reflections on the optical elements light beams might become linearly polarized to some degree. Besides that, polarization effects can occur outside the telescope. The daylight sun leads to a high degree of sky polarization. This might affect polarization measurements during twilight.

The following measurement is set up to reveal, whether such effects occur.

A set of zeropol standard stars is part of the target list (cf. A.3). As with the polarization angle calibration, all data until April 2009 was taken into account and selected to receive a  $3\sigma$  data set. A number of 100 data points are available from this selection and is displayed in Fig. 7.5.

Using the median and standard deviation one gets an instrumental polarization degree of

$$P_{\text{inst}} = (0.6 \pm 0.5)\%$$

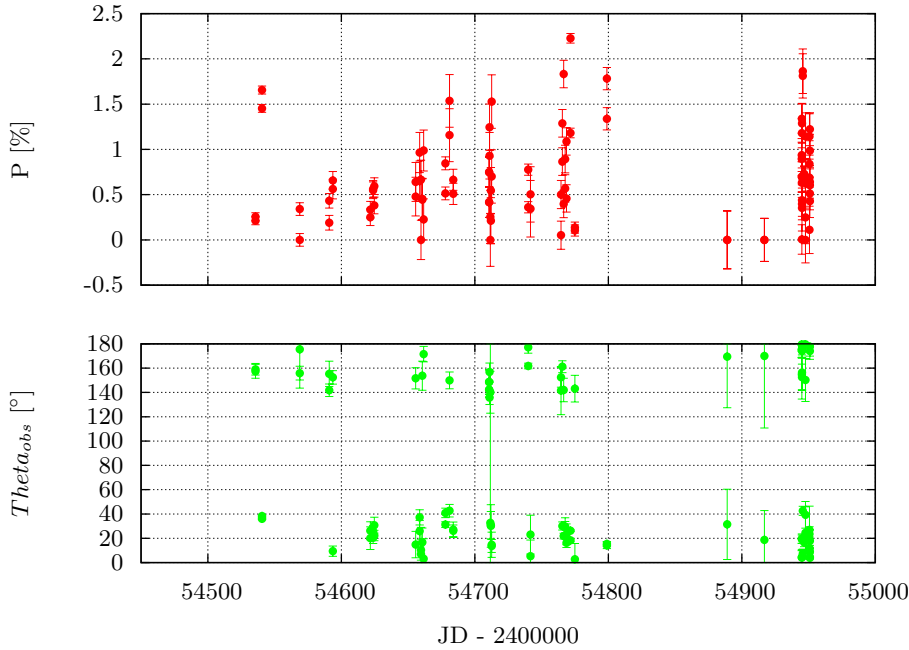


Figure 7.5: Polarization Measurements of Zeropol Standard Stars ( $3\sigma$ -selected measurements)

The instrumental polarization angle is derived using the incidence that angles between  $90^\circ$  and  $180^\circ$  can be substituted by their equivalent angle in the plane of polarization between  $-90^\circ$  and  $0$ . This leads to

$$\Theta_{\text{obs}} = (7 \pm 24)^\circ$$

using median and standard deviation. A histogram showing the distribution of polarization angles is shown in Fig. 7.6 Polarization angles are shifted in this plot in order to have the distribution centered around  $0^\circ$ , according the ambiguity of the polarization angle plane.

The wide spread of the occurring polarization angles and the large error of the median angle leads to the hypothesis, that there is not a concrete instrumental polarization, but a trend leading to some preferred polarization direction. The instrumental polarization degree measured above might be explained by the statistical scattering of photon fluxes in the four images of the measurement. This scatter makes the Stokes vectors  $U$  and  $Q$  vary around their true values according to Eq. 2.9. Since the polarization degree is derived using a quadratic addition of both vectors (Eq. 2.10), each variation of  $U$  and  $Q$  lead to an overestimated polarization degree.

Therefore, I would prefer to state, that there is an instrumental polarization, which is indicated by a preferred polarization direction, but its polarization degree is smaller than  $0.6\%$ .

## 7.2.6 Problems

There are many effects that disturb polarimetric measurements. Some major ones are discussed here.

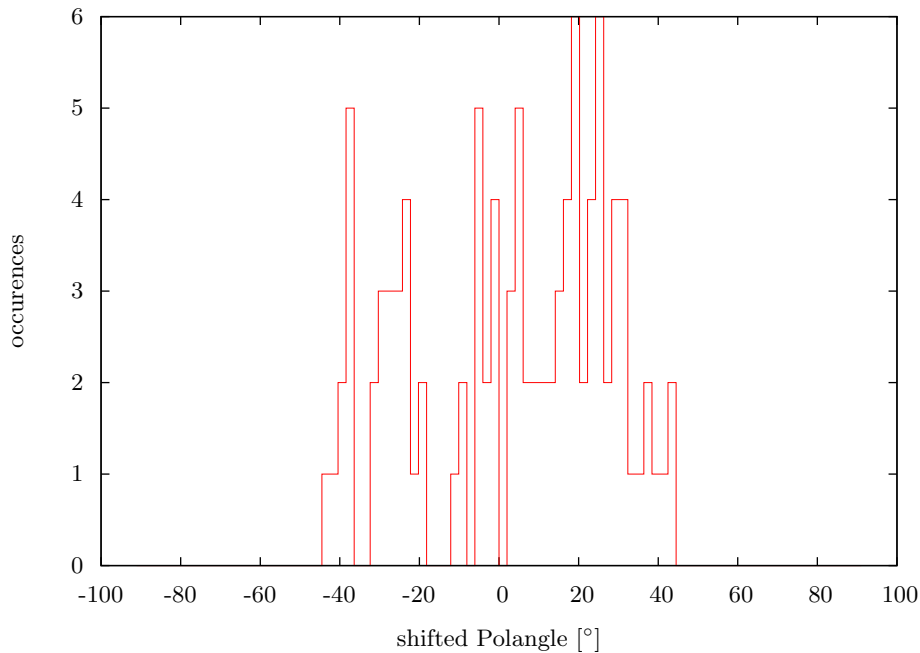


Figure 7.6: Distribution of Polarization Angles of Zeropol Standard Stars ( $3\sigma$ -selected measurements)

**Clouds** Clouds are affecting polarimetric measurements in two ways.

Since polarimetry is a combination of photometric measurements, it suffers in the same way as photometry from overcast skies. This means, that one measures a smaller flux of an object when overcast, compared to a cloud-free sky. Hence, using the same integration time, one gets a smaller signal-to-noise ratio.

However, even thin clouds are a problem for polarimetry, since one needs a set of a four images, which have to be taken under the exact same condition. Clouds moving through the field of view during an integration sequence cause variations of the object's flux which may lead to a misleading polarization measurement. This gives rise to exorbitant polarization degrees of (sometimes much) more than 30%. For this reason, all data are filtered using a  $3\sigma$ -selection, for instance. Unfiltered data shows serious scattering of polarization degree and angle and is subject to many outliers.

**Twilight and Moon** The daylight sky is highly polarized by the sun due to scatter effects. This scatter occurs when a photon excites an electron and therefore starts to vibrate. This linear movement makes the electron act like an antenna, which re-radiates a new photon in a random direction but within a plane, which is perpendicular to the incoming beam. This happens according to the directional characteristic of a Hertz' dipole. Hence, the sky is polarized tangential to a circle centered in the sun and maximum polarization is found at ninety degrees from it. Short time after sunset (or before sunrise) the degree of polarization of the sky can reach its maximum of about 75% in very clear days. The polarization at that time is aligned parallel to the meridian, since the sun is positioned in the west or east, respectively.

Since the moon reflects sunlight, it is subject to similar effects and may create sky polarization,

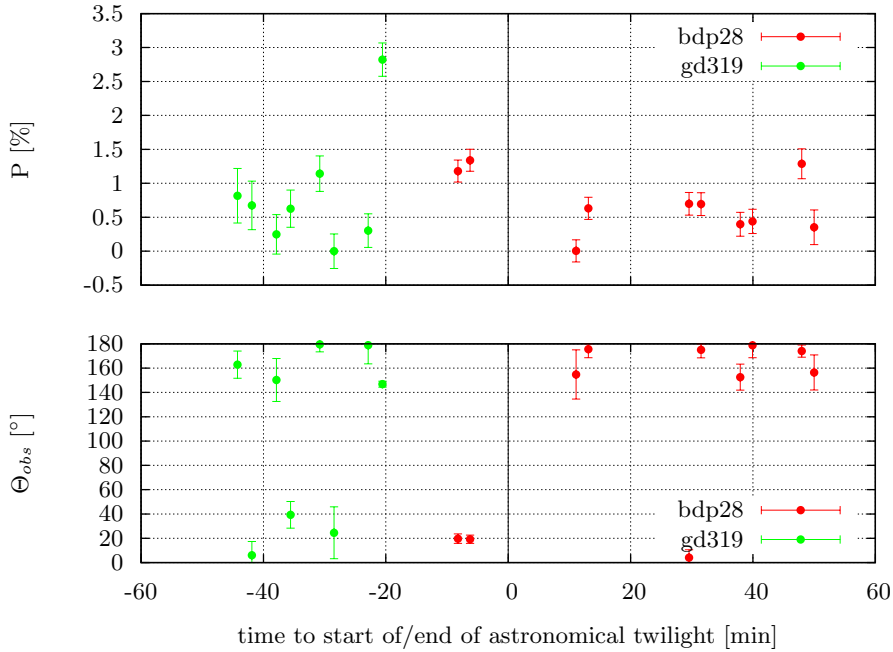


Figure 7.7: Polarization measurements of zeropol standard stars during twilight (10 $\sigma$ -selected measurements)

(for bdp28-data the vertical line represents the start of astronomical twilight, for gd319-data the end of the latter)

too. However, the polarization degree is expected to be less due to the lower brightness of the moon.

This sky polarization may affect polarization measurements of night sky objects, too. To investigate this, unpolarized standard stars have been imaged in series during twilight. The following objects were imaged for this reason:

- *BD +28d4211* (zeropol), imaged on April 23, 2009; 8 measurements starting before astronomical twilight and finished during nautical twilight; start of nautical twilight 5:09am local time, start of civil twilight 5:39am
- *GD 319* (zeropol), imaged on April 25, 2009; 8 measurements starting during nautical twilight and finished during astronomical twilight; start of astronomical twilight 8:11pm local time, end of astronomical twilight 8:42pm

If sky polarization would affect polarization measurements, one would expect a monotoneous variation of the polarization degree and angle over the time (due to the moving of the sun).

Results for are plotted in Fig. 7.7. It can be stated that variations in polarization degree and angle are far too large to see any clear trend. Furthermore, the mean orientation of the polarization angle is stable over the different phases of twilight. This leads to the conclusion, that there is no measureable influence of the sky polarization during twilight - at least for standard stars. The

impact on less bright objects might be quite measurable, since the S/N ratio of these is much lower and the sky background brightness comes into account.

For this reason, the twilight phases might be used for standard acquisition, to have the dark night for objects only.

One can derive from these conclusions, that the influence of moonlight on the measurements might even be smaller and can be neglected for bright objects. Of course, moonlight leads to an increased sky brightness and therefore a decreased S/N ratio, which affects the measurement. However, there is no impact on the polarization degree and angle to be expected.

## 7.3 Polarimetry Results

In order to show the functionality of the `dopolarimetry` script, a number of data sets have been analyzed. They are introduced in the following sections.

Each graph is splitted into two parts: the upper part (red line) shows the polarization degree as a function of time including error bars in both. The lower part (green line) gives the polarization angle, which is corrected for the rotational angle determined above. All measurements are quality checked using the cumulated comparison object fluxes.

### 7.3.1 Results of the October/November Run 2008

Some results of the October/November observing run in 2008 are shown in Fig. 7.8 to 7.13. Each object is part of the high priority list.

Sources presented here are the same ones which are presented in the photometry chapter (cf. Fig.6.5 to Fig.6.10), namely: **3C 66A**, **OJ287**, **BL Lacertae**, **1ES 0647+250**, **PKS 2155-304** and **S4 0954+650**. Although data have been filtered using only such with comparison star flux variations of smaller than  $3\sigma$ , the scattering in polarization degree and angle is evident and often exceeds a  $3\sigma$  limit. One might say, that variations are subject to physical processes. However, measurements using 'full cycles', i.e. two successively taken complete polarimeter sequences, show clear deviations on a very short time scale. Such variations are unlike to be real variations of the source. Some deviations scatter on a range of several  $\sigma$  leading to uncertainties of up to 2 % in polarization degree (Fig. 7.11) and some  $10^\circ$  in polarization angle. Similar results can be derived from other data sets. Averaging of 'full cycle' measurements may improve the results. However, it is desirable to use 'half cycle' (only one complete polarimeter sequence) measurements, which do not lead to two independent measurements. Therefore, the user has to rely on the result of a single measurement.

Nevertheless, the high degree of polarization of polarization is obvious and variations in polarization degree and angle are clearly detectable. However, it is hard to differentiate between *real* variations and scattering. Sources of scattering and estimations are discussed in 9.4.1.

The faintest source of the set, **S4 0954+650**, shows an extremely large error in polarization degree of more than 1.5 %. At that time, the brightness of the object was approximately 17.3 mag,

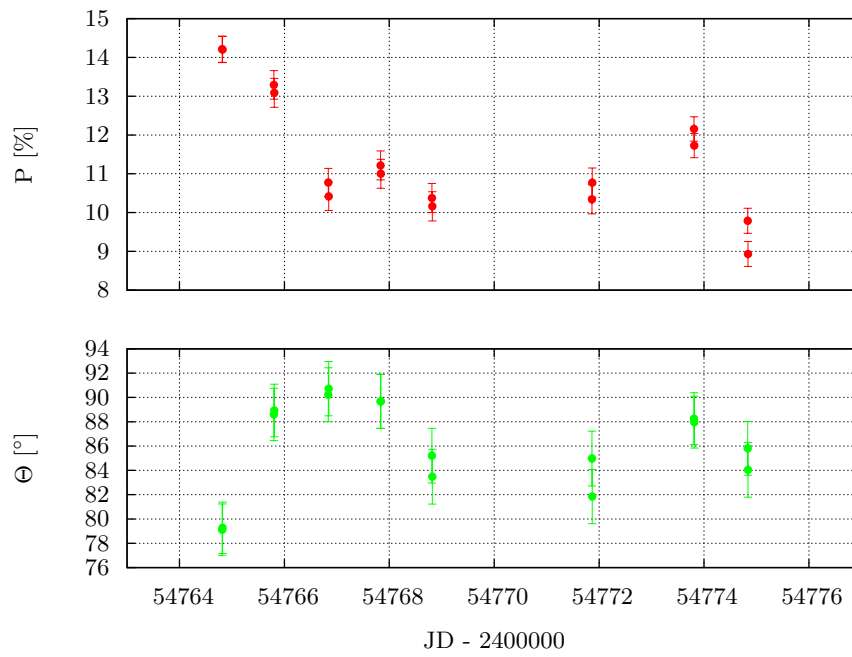


Figure 7.8: Polarimetric Results of **3C 66A** of the October/November Run 2008

with an signal-to-noise ratio of approximately 70. This seems to be the limit of the current setup. Monitoring of such faint objects is only advisable in case of outbreaks.

Remaining data of this run can be found uncommented in B.1.

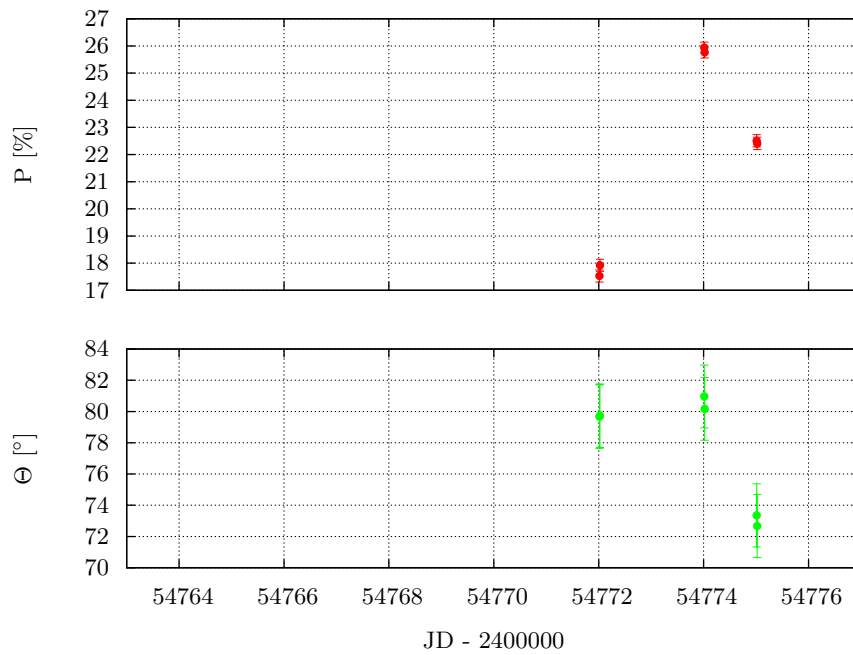


Figure 7.9: Polarimetric Results of **OJ 287** of the October/November Run 2008

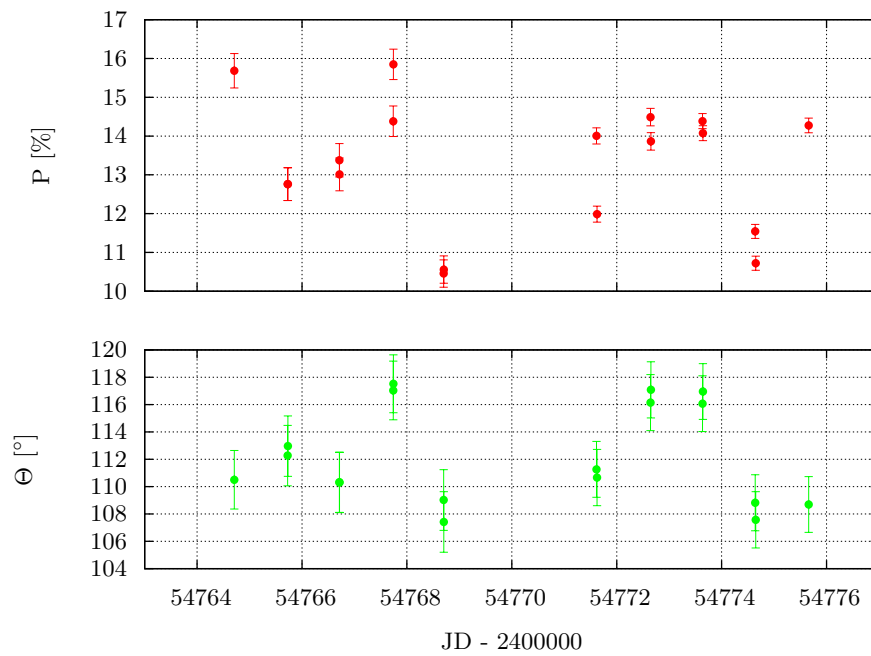
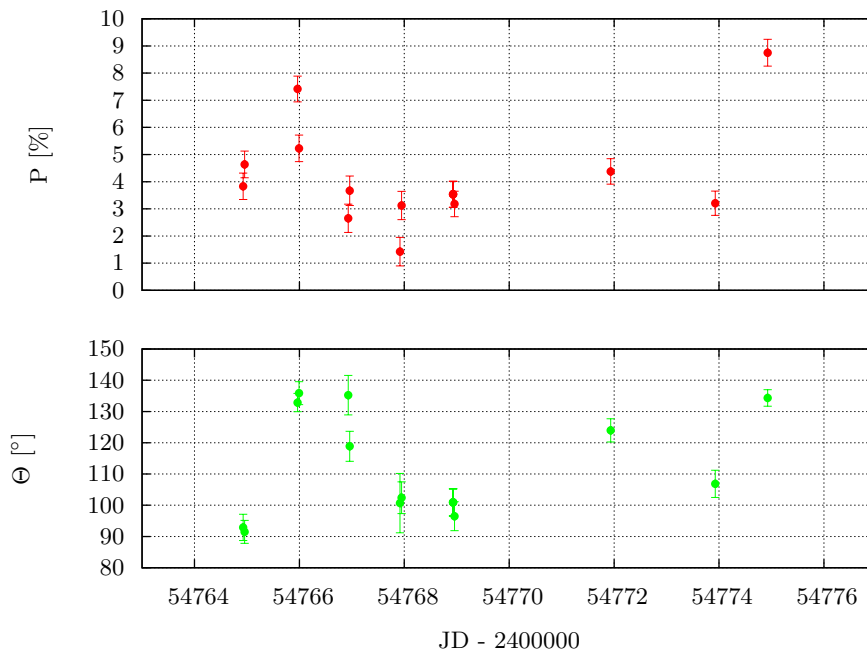
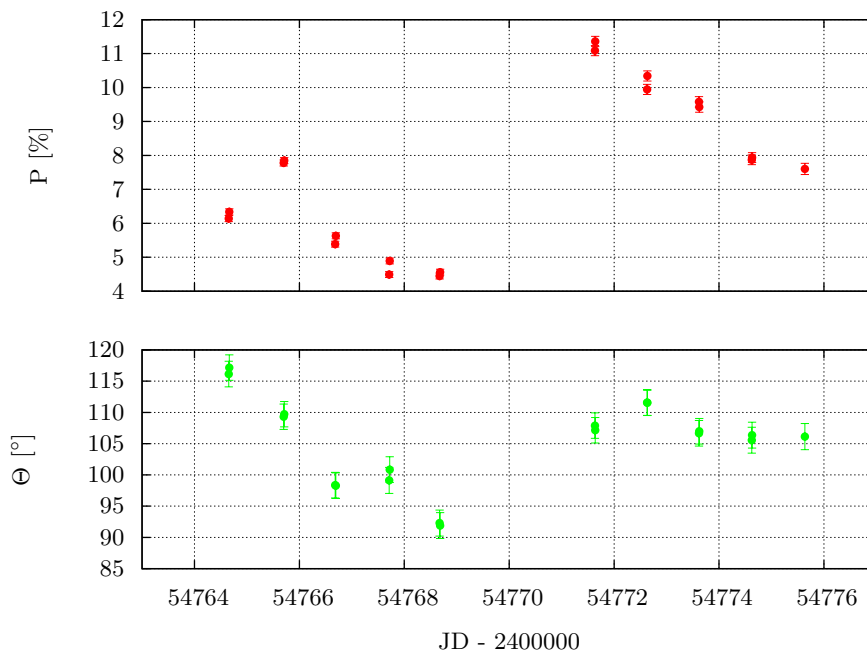


Figure 7.10: Polarimetric Results of **BL Lacertae** of the October/November Run 2008

Figure 7.11: Polarimetric Results of **1ES 0647+250** of the October/November Run 2008Figure 7.12: Polarimetric Results of **PKS 2155-304** of the October/November Run 2008



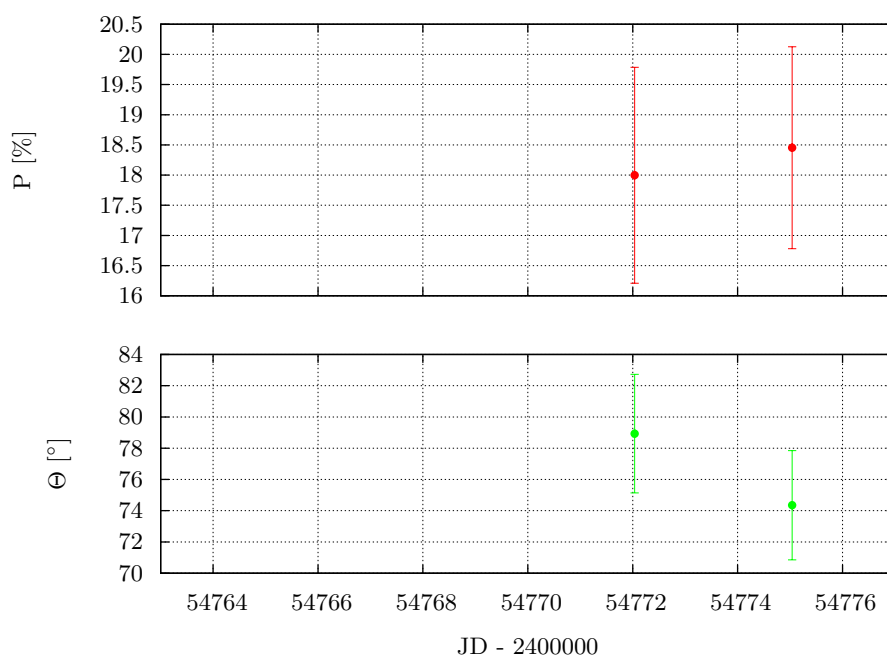


Figure 7.13: Polarimetric Results of **S4 0954+650** of the October/November Run 2008

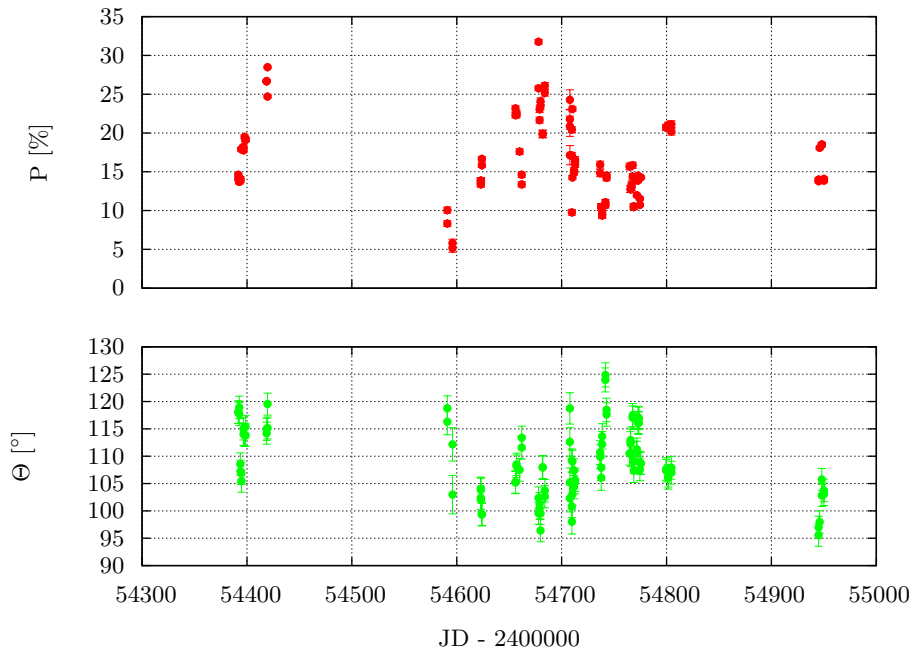
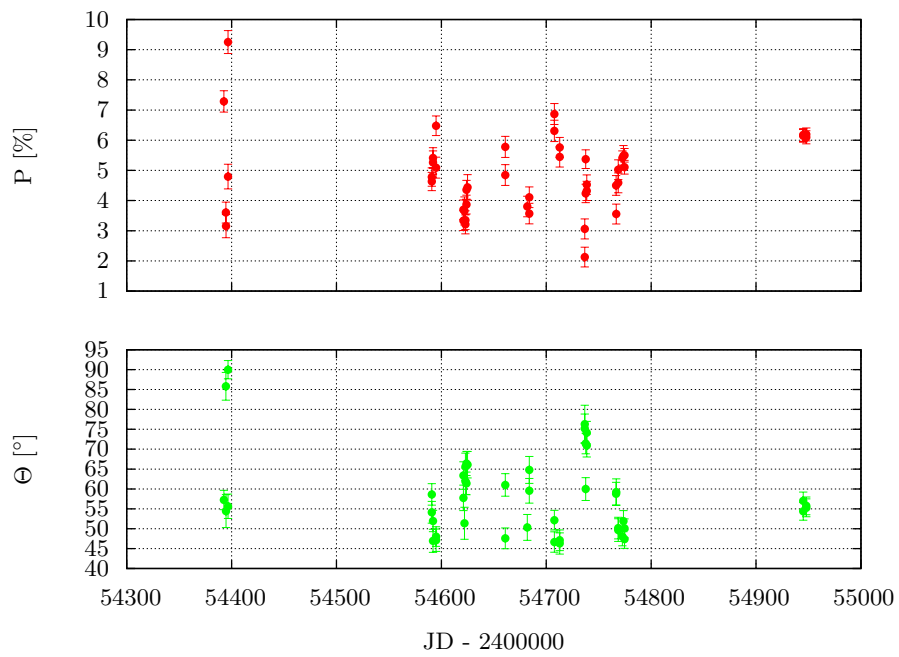
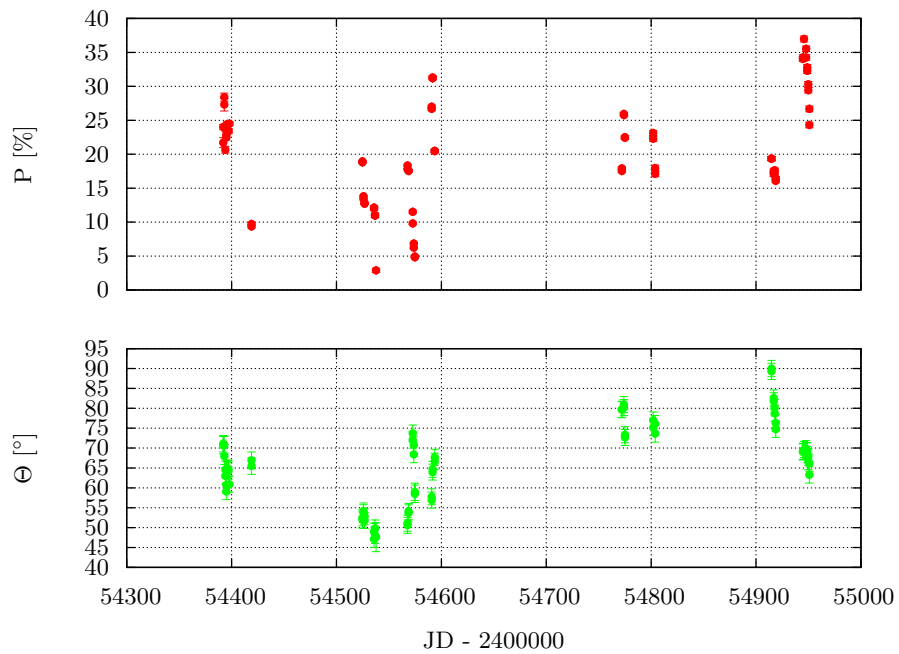


Figure 7.14: Polarimetric Results of **BL Lacertae** of all Runs

### 7.3.2 Long-term Results of BL Lac, 1ES 1959+650 and OJ 287

Analysis of long-term data of some objects show clear variations in polarization degree and angle of periods of some days. The amplitude of the variations are clearly larger than 2 % in polarization degree, which is typical for statistical scattering. Hence, long-term variability is clearly detectable using the setup but with a strictly limited accuracy.

Again, as in the photometric results, **OJ 287** and **BL Lacertae** show a highly violent behaviour in polarization degree and variations in the polarization angle.

Figure 7.15: Polarimetric Results of **1ES 1959+650** of all RunsFigure 7.16: Polarimetric Results of **OJ 287** of all Runs



# Chapter 8

## Conclusion

The aims of the thesis have been achieved. An automatized pipeline software has been designed and is ready to be used. Sample data have been reduced and analyzed leading to acceptable results.

*In the following, the achievements concerning the Polima pipeline, photometric and polarimetric analysis are outlined.*

### 8.1 Image Reduction - the Polima Pipeline

The `polima` software package includes various tasks for image reduction, photometric and polarimetric analysis. It offers the advantages of the IRAF software package and is fully integrated there. Installation is simple and the handling of the software is easy to learn but offers a high degree of freedom using different task parameters. The software allows to reduce and analyze data of a complete observing run within some hours.

Image reduction routines are completely automatized. The software is able to produce reduced images from a set of raw science and correction images. However, the use of external correction images is possible. Each processing step is archived using a log file to achieve transparency for the user.

The reduction process is well tested using manually reduced data sets and showing good results.

### 8.2 Photometry

The photometry task `dophotometry` offers circular and elliptical shaped apertures which are of fix size or fitted to the image. Object identification is automatized using the stand-alone software `wcs-tools`<sup>1</sup>. Calculation steps are archived using a log file to achieve transparency for the user. Results can be printed in tabular form to a file to simplify further data analysis.

Tests showed, that best photometric results can be achieved using fitted elliptical shaped apertures with a major axis length of 2 to 2.5 FWHM of the objects point spread function. In this case, the determined magnitude gives the best estimation and simultaneously the smallest magnitudal

---

<sup>1</sup><http://tdc-www.harvard.edu/wcstools/>

error. Magnitude errors usually range in the  $10^{-2}$  and are strongly influenced by the comparison object uncertainty. Measurements of magnitudes up to 17 mag and more are possible and reliable.

The data quality can be judged using the mean magnitudal residual of a comparison object, i.e. the averaged difference of the real magnitude of the object and the calculated magnitude using each other comparison object. This provides a good measure to find bad data sets.

### 8.3 Polarimetry

The polarimetry task `dopolarimetry` is widely based on `dophotometry` concerning flux determination and object identification. It therefore offers the same features.

Results show that the quality of polarimetric measurements depend much more on sky transparency than photometric ones. Therefore, proper data quality control is mandatory to receive trustworthy results. For this reason, fluxes of comparison stars are summed up. A comparison of these allow to judge the sky quality during the exposure.

Due to the high sensitivity to sky transparency variations, the accuracy of polarimetric measurements is limited. Additionally, results show variations on very short time-scales, even in successively taken measurements polarization degree variations of 2 % may occur. Sources of such variations are discussed in 9.4.1.

Polarimetric measurements demand a higher signal-to-noise ratio than photometric measurements. Sources fainter than 17 mag lead to large errors in polarization degree that can exceed 1.5 %. Therefore, the limiting magnitude of polarization measurements is adviced to be 17 mag.

Best results can be obtained using circular apertures for flux determination - different from photometric analysis. The aperture diameter should be chosen in a way to include the most possible fraction of an objects flux but exclude contributions from neighboring objects. Cumulated comparison object fluxes should not deviate more than  $3\sigma$  (i.e. three times the square-root of the comparison object flux) from the maximum flux value of this object for all measurements.

Analysis of polarimetric standard stars showed that the instrumental polarization of the setup is  $(0.6 \pm 0.5)\%$  with a polarization angle of  $(7 \pm 24)^\circ$ . The large errors of both values speak for a neglectable instrumental polarization. The rotational angle of the polarimeter was determined to be  $\Delta\Theta = (-91 \pm 2)^\circ$  (with  $\Delta\Theta = \Theta_{\text{obs}} - \Theta_{\text{real}}$ ).

# Chapter 9

## Discussion

After introducing the `Polima` pipeline and presenting some results, possible error sources and future enhancements of the software are discussed.

*Following, telescope setup, image reduction, photometric and polarimetric results and possible sources of error are discussed.*

### 9.1 Telescope Setup

Results show that both, telescope setup and site, are appropriate to perform polarimetric monitoring. The telescope setup allows imaging of faint objects down to 17 mag and even more leading to good photometric results. Polarimetric results underlie scattering but are usable.

The telescope handling is easy to learn and robust. The setup is undergoing some modernization measurements (e.g. dome opening/closing automatization) which will continue in the near future.

#### 9.1.1 Recommendations

In order to improve results, two measures concerning the telescope setup are suggested.

##### Improving of Dome-Guiding

The telescope dome slit is supposed to follow the direction of the telescope automatically to prevent the telescope aperture to be partly obstructed by the dome. However, the dome of the 0.84 m telescope at SPM is sometimes misaligned and cannot follow the direction of the telescope correctly. Therefore, the measured flux of an object is diminished by this occultation.

This is a problem for polarimetric measurements, since four images form one single polarization measurement. If the dome tracking does not work properly and the occulted fraction of the telescope aperture varies for each integration, incorrect fluxes are measured. The result would be an artificial polarization which is measured.

The worst scenario would be a not moving dome that gradually obscures the telescope aperture. To have an estimation of the effect, the following calculations were done.

In order to simplify the model, geographic latitude and the declination of the object are ne-

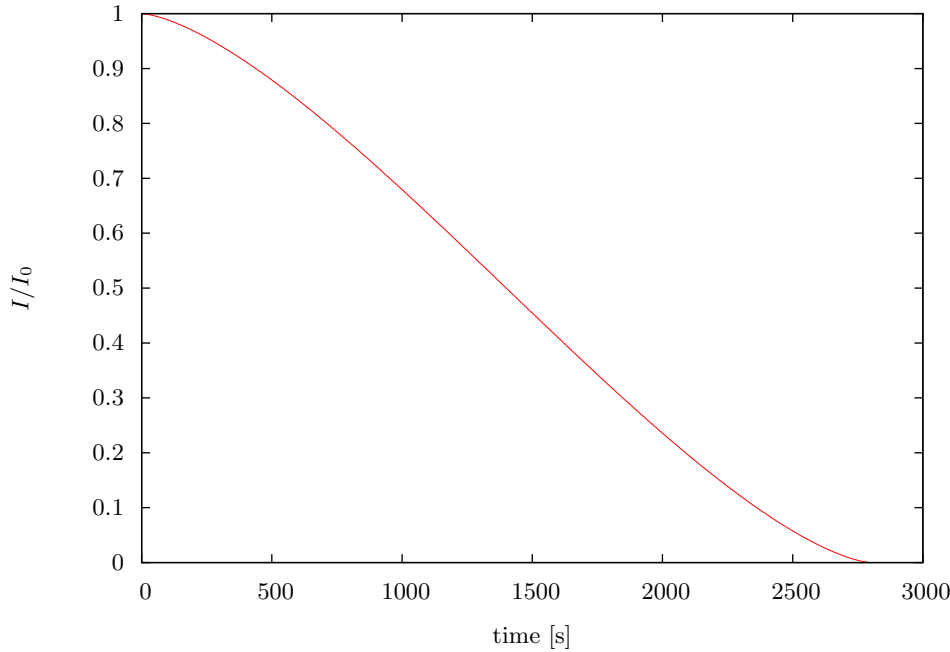


Figure 9.1: Simulated decrease of an objects intensity if dome tracking is disabled

glected. Hence, following calculations refer to an object moving parallel to the horizon.

The situation regarded is that telescope and dome slit are aligned in a way that the aperture of the telescope is not obstructed at  $t = 0$  but at any later moment due to Earth's rotation. The telescope is following the object while the dome remains in it's position. Hence, the intensity fraction  $I/I_0$  between the measured intensity  $I$  and the unobscured intensity  $I_0$  equals 1. With the telescope moving, a growing segment of the mirror gets obscured and the intensity fraction decreases. The distance of the outermost part of the telescope mirror being obscured from the slit's edge is  $x(t)$ , which is increasing in time. The obscured area is then expressed by

$$A(t) = \left(\frac{D}{2}\right)^2 \arccos\left(1 - \frac{2x(t)}{D}\right) - \sqrt{Dx(t) - x^2(t)} \cdot \left(\frac{D}{2} - x(t)\right) \quad (9.1)$$

and the intensity fraction then follows with

$$\frac{I(t)}{I_0} = \frac{\left(\frac{D}{2}\right)^2 \pi - A(t)}{\left(\frac{D}{2}\right)^2 \pi} = 1 - \frac{4A(t)}{D^2 \pi} \quad (9.2)$$

The distance  $x(t)$  can be expressed using Earth's rotational frequency  $\omega = 2\pi/86400\text{s}$  and the distance of the dome measured from the telescope mirror, which is estimated to be  $r = 4$  m,  $x(t) = \omega t r$ . Using these values, the decrease of the intensity fraction follows Fig. 9.1. The telescope's aperture is completely obscured after  $2800 \text{ s} = 46 \text{ min } 40 \text{ s}$ .

The (fractional) flux, that would have been measured by an observer, is obtained by integrating the fractional intensity over the integration time. Especially for short integration times the CCD



Table 9.1: Simulated artificial polarizations for different integration times with a stationary dome

<b>integration time</b> [s]	$P_{(0/45/90/135)}$ [%]	$P_{(0/90/45/135)}$ [%]
10	3.5	2.0
20	4.2	2.4
30	4.9	2.7
60	6.7	3.7
180	12.5	6.8
300	19.0	9.0
600	39.4	22.3

readout time has to be regarded, since the telescope is moving during this times, too. The readout time is measured to be approximately 10 s per integration.

The artificial polarization measured for an object with unobstructed intensity  $I_0$  can be estimated by calculating the differences in flux for the different polarimeter angles and then using Eq. 2.9 and 2.10. Results are listed in Tab. 9.1 for different integration times. Two polarization values have been calculated. They represent the estimations for different polarization analyzer sequences according to the noted subscript sequences.

It is obvious, that even for short integration times - as used for standard stars - the polarization degree is highly affected. The resulting deviation is up to the real degree of polarization of some standard stars. Furthermore, there is a high impact of the polarization analyzer sequence on the results. As expected in 3.2, the sequence  $0^\circ, 90^\circ, 45^\circ, 135^\circ$  is less prone to such flux variations.

The listed results are estimations for a stationary dome. Usually, dome tracking is activated and the impact of dome obscuration is smaller than estimated here. If the area of obscuration is the same for each integration, the effects cancels out and the polarization degree can be obtained properly. However, this case is unexpected, since dome tracking at SPM is not a continuous process but done stepwise. Therefore, even small degrees of obscuration may affect measurements and surely contributes to the measured scatter of polarization degrees and angles. Hence, a proper dome tracking is mandatory.

### Two-beam Polarimeter

The currently used Polima polarimeter (cf. 3.1.3) creates a single fully linear polarized beam. Each polarimeter angle adjustment has to be imaged separately.

The installation of a two-beam polarimeter would halve the integration time for a complete measurement and improve data quality. Different from a one-beam polarimeter, it splits the incoming into two beams, which are each linearly polarized in planes perpendicular to each other. Therefore, only two images have to be taken of each object which are rotated by  $45^\circ$ . This halves integration time. Another advantage would be, that images belonging to perpendicular polarimeter angles (i.e.  $0^\circ$  and  $90^\circ$ , as well a  $45^\circ$  and  $135^\circ$ , respectively) are taken under exactly the same observational conditions. Therefore, the influence of atmospheric effects decreases and data quality

increases.

The purchase of such a new polarimeter was discussed but is not yet planned.

## 9.2 Image Reduction

Image reduction was tested extensively and shows good results. However, the impact of some effects are not yet cleared.

### CCD linearity

At the observatory available CCD detectors have a dynamical range of 16 bit, i.e. a range 65536 possible values. However, the useable range is limited due to nonlinearities in the detector behaviour. The desired median value of flatfield images is preset to a value of 30000. This is to avoid nonlinear effects, which show up in the range of high values.

In order to be sure, that images (especially flatfield images) underlie linearity, the detector behaviour should be examined extensively. If necessary, imaging macros and observing behaviour should be adapted.

### Shutter Speed

The limited shutter speed leads to an inhomogeneous illumination of an image. The impact of this can be observed in images of extreme short exposure time ( $\approx 1$  s). Since some of the objects and standard stars observed are bright sources, shutter speed may have an impact on the results, especially those of polarimetric measurements.

It is advisable to examine the impact of the shutter speed on polarimetric measurements and adapt corrections if necessary.

## 9.3 Photometry

The photometry script `dophotometry` shows good results and robust handling. Errors are mainly determined by comparison object errors.

Possible enhancements are not obvious at the moment.

## 9.4 Polarimetry

The most important question concerning polarimetric measurements is the origin of the scattering of results. Besides that problem, data analysis using the `dopolarimetry` script works good.

### 9.4.1 Scatter of Polarimetric Results

One can observe a distinct level of scattering in polarimetric measurements in both, polarization degree and angle. The scatter is observed in every kind of target, polarized and unpolarized standard stars and scientific objects. It superposes the 'real' variations of a source which becomes

distinct in 'full cycle' measurements: it contains two independent measurements which scatter in a range, which may overspan much more than  $3\sigma$  (cf. results in Fig. 7.8 and following).

The source of this scatter is not obvious, several effects may contribute:

**Atmospheric effects** Variations in sky transparency caused by clouds have already been discussed in 7.2.6. In order to detect variations and judge data quality, the total flux of each comparison object is calculated for each measurement. It is recommended to use only such measurements with variations inbetween a  $3\sigma$ -range.

However, due to the allowed variations inbetween this limits, some effects might be neglected. Such may be moving bands of cirrus clouds or vapor trails caused by aircrafts transiting the object for a short time leading to a decrease of the measured flux and therefore a falsification of the result.

Simple calculations using Eq. 2.9 and 2.10 show, that an attenuation of the object flux during one integration of the polarimeter sequence of 1 % leads to an error in polarization degree of 0.5 %. However, using a  $3\sigma$ -area in comparison star fluxes leads to the same uncertainties in object flux and therefore usually more than 1 % fluctuations. Errors of more than 1 % are possible.

In order to improve results and limit uncertainties, a stricter selection of data is recommended if the data set allows this. The impact of atmospheric effects can also be limited by using a two-beam polarimeter (cf. 9.1.1).

However, scatter of polarimetric results can also be observed in data taken in completely cloudless nights. Hence, other effects must contribute to the scatter.

**Dome obstruction** The impact of improper dome guiding is explained in detail in 9.1.1. An improvement of the dome guiding would extinct this error source completely.

**Inproper flux determination** From experience, it is recommended to use circular apertures of fix but user-defined size. Maybe other aperture shapes and sizes lead to better flux determinations. For instance, polygons of arbitrary shape may be fitted to each object in the image separately. This would account for bad focus and guiding errors.

However, the impact of such a measure is believed to be small, since tests showed that flux determination works fine.

**Inproper error estimations** A completely different ansatz to explain the scatter in polarimetric results is to question the calculated errors. Examinations of polarized standards stars (cf. Fig. 7.2, 7.3 and 7.4) show that the scatter of the polarization degree is approximately 3 times higher than the mean of the calculated errors. Therefore, the calculated errors seem to be underestimated. Polarimetric errors in this thesis (Eq. 2.11 and 2.12) are derived from Eq. 2.9 and 2.10 using gaussian error propagation. Therefore, error bars are symmetrical.

Another approach is given by Simmons and Stewart ([SS85]), who introduce confidence intervals and account for the signal-to-noise ratios of the measurement.



# Appendix A

## Target Lists

### A.1 Objects

A table containing the sources observed during this project divided into two sections are displayed in Tab. A.1. High priority targets are divided from low priority targets. An explanation of this division can be found in section 1.1.3.

### A.2 Standard Stars

Polarized standard stars are listed in Tab. A.2, unpolarized standard stars in Tab. A.3, respectively.

Table A.1: High and Low Priority Target List

<b>object name</b>	<b>object code</b>	<b>RA (2000)</b>	<b>Dec (2000)</b>	<b>z</b>
3C 66A	3c66a	02 22 39.6	+43 02 08	0.444
1ES 0647 +250	e0647	06 50 46.5	+25 03 00	0.203
S5 0716 +714	s0716	07 21 53.4	+71 20 36	0.3 ?
PKS 0735 +178	p0735	07 38 07.4	+17 42 19	0.424
OJ 287	oj287	08 54 48.9	+20 06 31	0.306
S4 0954 +650	s0954	09 58 47.2	+65 33 55	0.368
Mkn 421	mk421	11 04 27.3	+38 12 32	0.030
ON 231	on231	12 21 31.7	+28 13 59	0.102
3C 273	3c273	12 29 06.7	+02 03 09	0.158
3C 279	3c279	12 56 11.1	- 05 47 22	0.536
Mkn 501	mk501	16 53 52.2	+39 45 37	0.034
OT 546	ot546	17 28 18.6	+50 13 10	0.055
3C 371	3c271	18 06 50.7	+69 49 28	0.051
1ES 1959 +650	e1959	21 58 52.0	- 30 13 32	0.116
BL Lac	bllac	22 02 43.3	+42 16 40	0.069
1ES 2344 +514	e2344	23 47 04.8	+51 42 18	0.044
1ES 0033 +595	e0033	00 35 52.6	+59 50 05	0.086
RGB 0136 +391	r0136	01 36 32.7	+39 06 00	?
RGB 0214 +517	r0214	02 14 17.9	+51 44 52	0.049
AO 0235 +164	a0235	02 38 38.9	+16 36 59	0.940
PKS 0420 -014	p0420	04 23 15.8	- 01 20 33	0.914
PKS 0528 +134	p0258	05 30 56.4	+13 31 55	2.060
1ES 0806 +524	e0806	08 09 49.2	+52 18 58	0.138
OJ 248	oj248	08 30 52.1	+24 11 00	0.939
OJ 49	oj049	08 31 48.9	+04 29 39	0.174
PKS 0836 +710	p0836	08 41 24.3	+70 53 42	2.172
PKS 1127 -145	p1127	11 30 07.0	- 14 49 27	1.184
4C 29.45	q4c29	11 59 31.8	+29 14 44	0.729
PKS 1222 +216	p1222	12 24 54.5	+21 22 46	0.432
PKS 1510 -089	p1510	15 12 50.5	- 09 06 00	0.360
DA 406	da406	16 13 41.0	+34 12 48	1.401
4C 38.41	q4c38	16 35 15.5	+38 08 04	1.813
3C 345	3c345	16 42 58.8	+39 48 37	0.592
4C 51.37	q4c51	17 40 37.0	+52 11 43	1.375
CTA 102	ct102	22 32 36.4	+11 43 51	1.037
3C 454.3	3c454	22 53 57.7	+16 08 54	0.360

Table A.2: highly polarized standard stars

object name	object code	RA (2000)	Dec (2000)	mag (R)
BD+64d106	bdp64	00 57 36.7	+64 51 27	10.3
HD 236633	h2366	01 09 12.3	+60 37 41	9.2
HD 7927	h7927	01 20 04.9	+58 13 54	5.0
BD+59d389	bdp59	02 02 42.1	+60 15 27	9.1
HD 236954	h2369	02 13 37.3	+59 10 15	9.4
HD 19820	h1982	03 14 05.4	+59 33 48	7.1
HD 23512	h2351	03 46 34.2	+23 37 27	8.2
HD 25443	h2354	04 06 08.1	+62 06 07	6.8
HD 245310	h2453	05 36 23.0	+21 11 11	9.0
HD 251204	h2512	06 05 05.7	+23 23 39	10.3
HD 43384	h4338	06 16 58.7	+23 44 27	6.3
HD 154445	h1544	17 05 32.2	-00 53 32	5.6
HD 155197	h1551	17 10 15.6	-04 50 03	9.2
HD 155528	h1555	17 12 19.9	-04 24 09	9.6
HD 161056	h1610	17 43 47.0	-07 04 46	6.3
HD 183143	h1831	19 27 26.5	+18 17 45	6.9
Hiltner 960	hi960	20 23 28.4	+39 20 56	10.6
VI Cyg 12	vicyg	20 32 40.9	+41 14 26	11.5
HD 204827	h2048	21 28 57.7	+58 44 24	7.9

Table A.3: zero polarized standard stars

object name	object code	RA (2000)	Dec (2000)	mag (R)
Beta Cas	becas	00 09 10.7	+59 08 59	2.3
HD 12021	h1202	01 57 56.1	-02 05 58	8.9
HD 14069	h1406	02 16 45.2	+07 41 11	9.0
HD 21447	h2144	03 30 00.2	+55 27 07	5.1
G191B2B	g191b	05 05 20.6	+52 49 54	11.8
HD 94851	h9485	10 56 44.2	-20 39 52	9.2
GD 319	gd319	12 50 04.5	+55 06 03	12.3
Gamma Boo	gaboo	14 32 04.7	+38 18 30	3.0
BD+332642	bdp33	15 51 59.9	+32 56 54	10.8
HD 154892	h1548	17 07 41.4	+15 12 38	8.0
BD+32d3739	bdp32	20 12 02.1	+32 47 44	9.3
BD+28d4211	bdp28	21 51 11.1	+28 51 52	10.5
HD 212311	h2123	22 21 58.6	+56 31 53	8.1
Zeta Peg	zepeg	22 41 27.7	+10 49 53	3.4



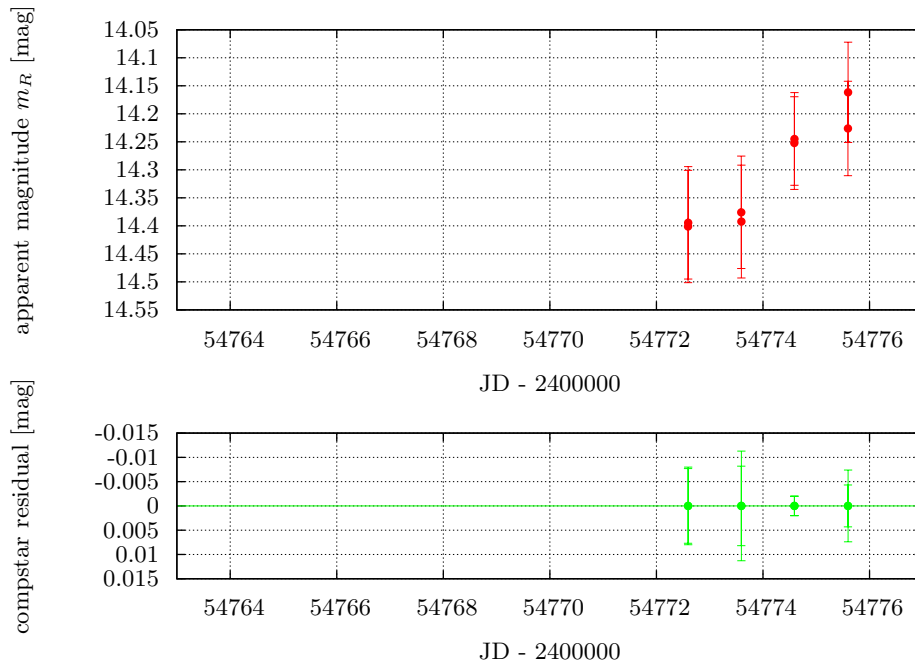
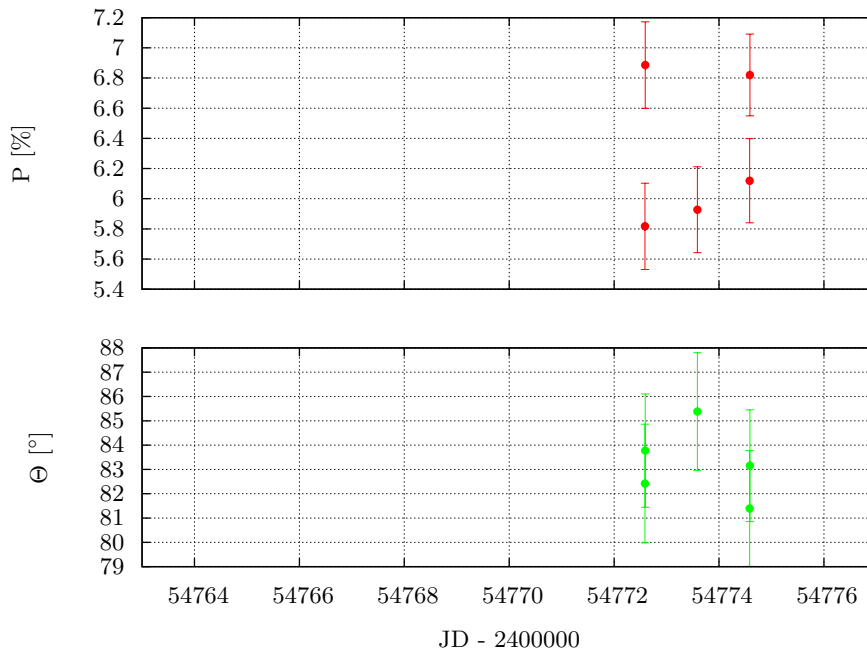


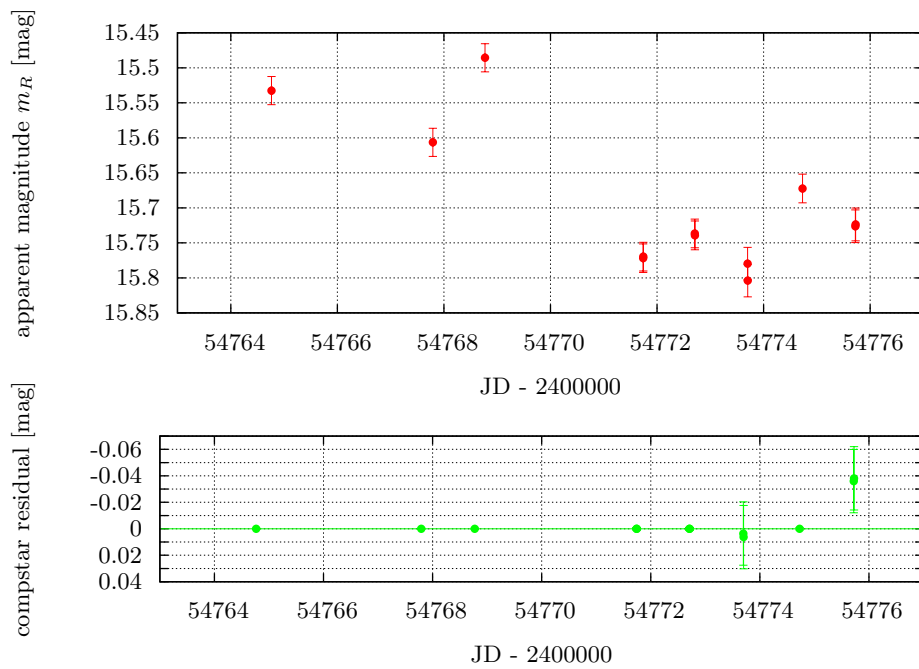
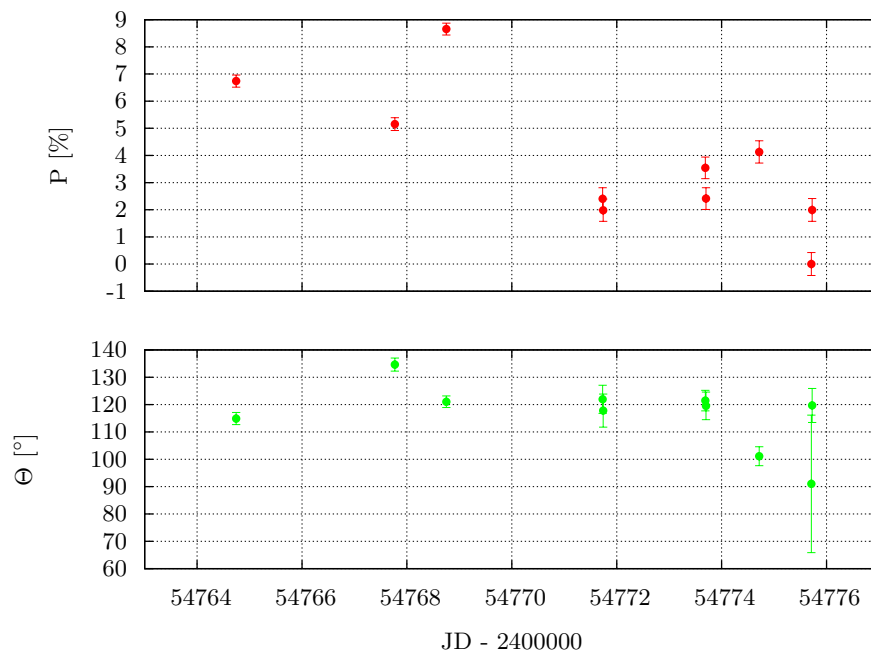
## Appendix B

# Further Results

### B.1 October/November Run 2008

Uncommented photometric and polarimetric data of this run follow. Due to bad data quality, there are no polarimetric data of the object 'PKS 0528+134'.

Figure B.1: Photometric Results of **3C 371** of the October/November Run 2008Figure B.2: Polarimetric Results of **3C 371** of the October/November Run 2008

Figure B.3: Photometric Results of **3C 454.3** of the October/November Run 2008Figure B.4: Polarimetric Results of **3C 454.3** of the October/November Run 2008

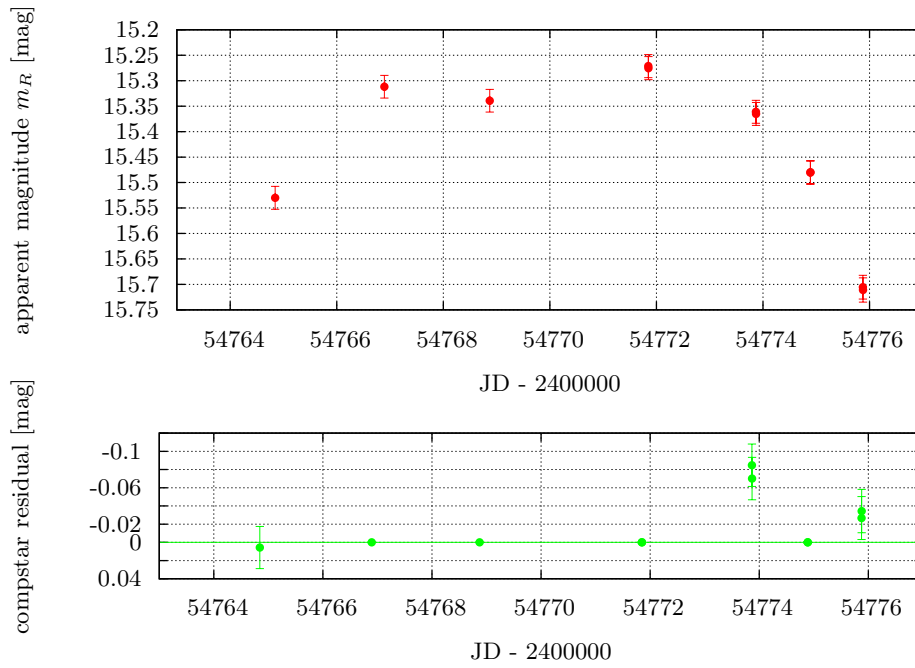


Figure B.5: Photometric Results of **AO 0235+164** of the October/November Run 2008

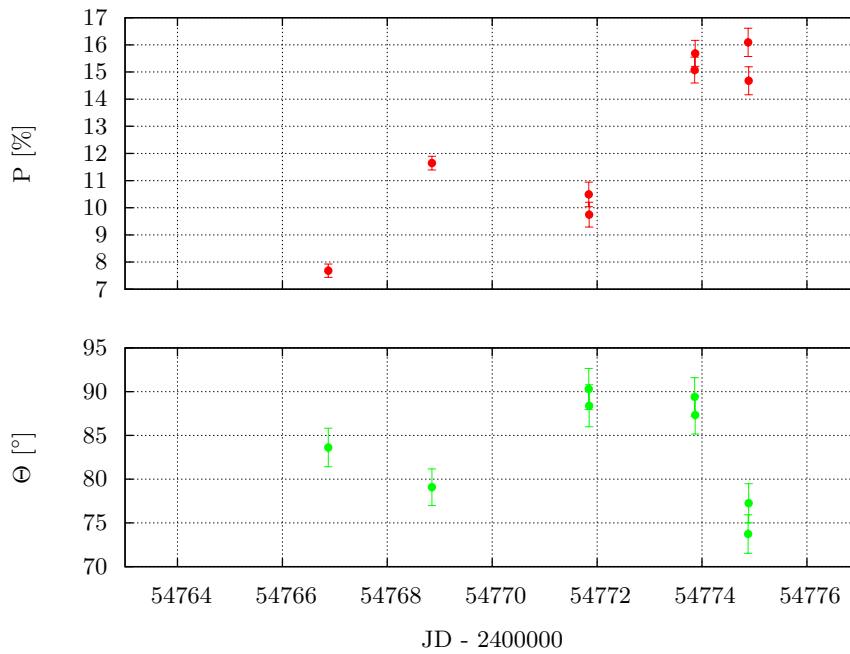
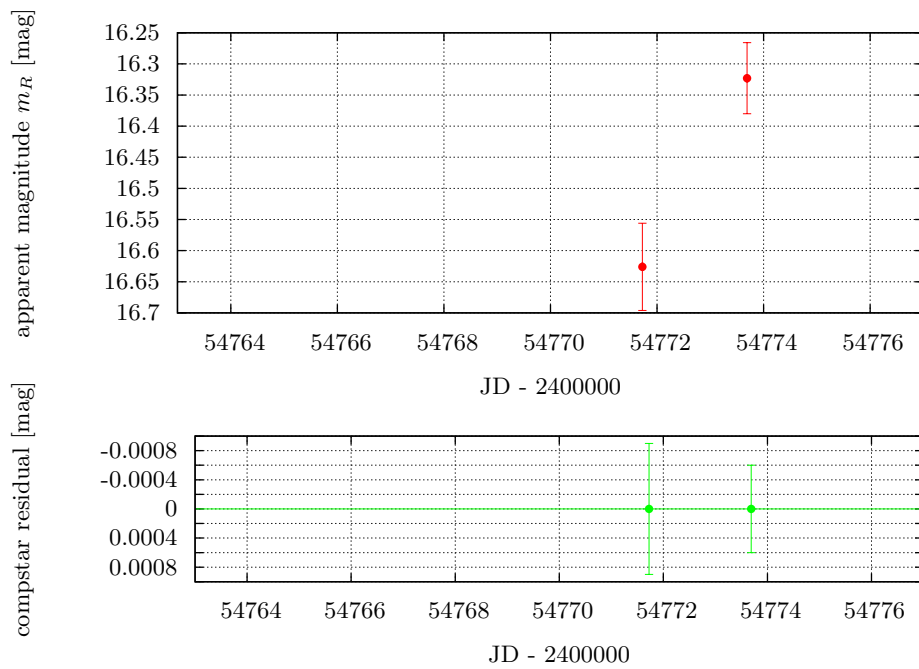
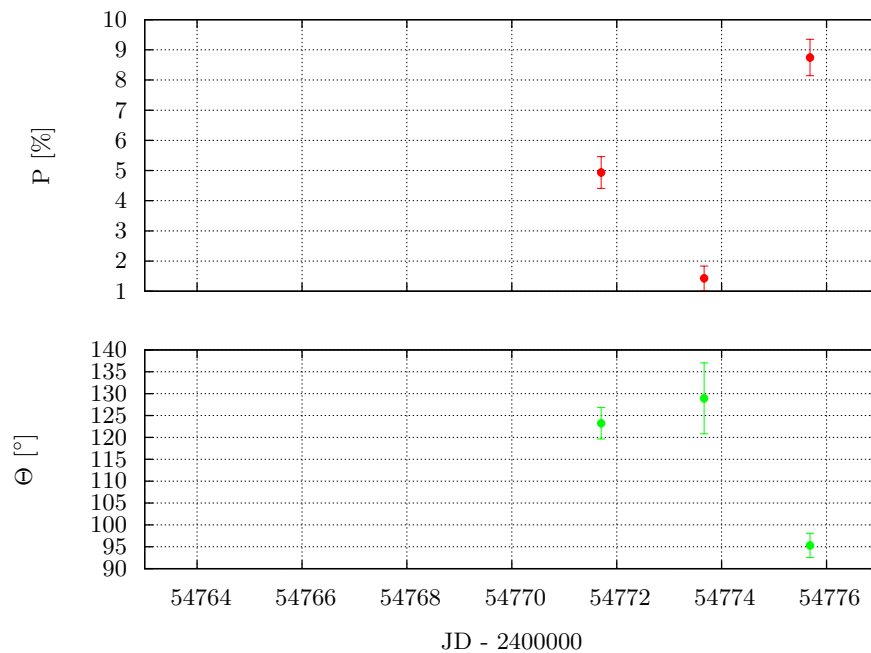
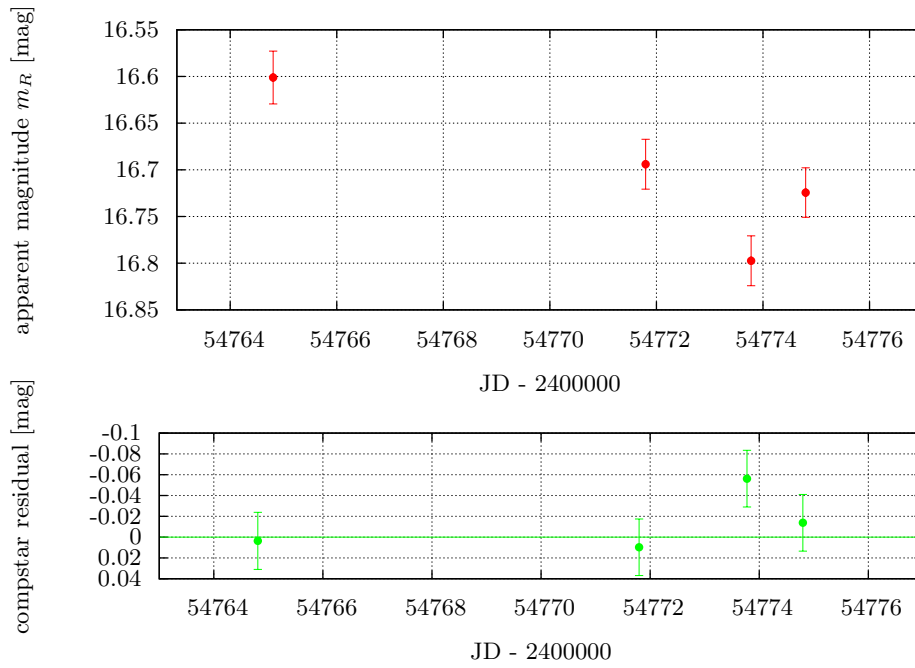
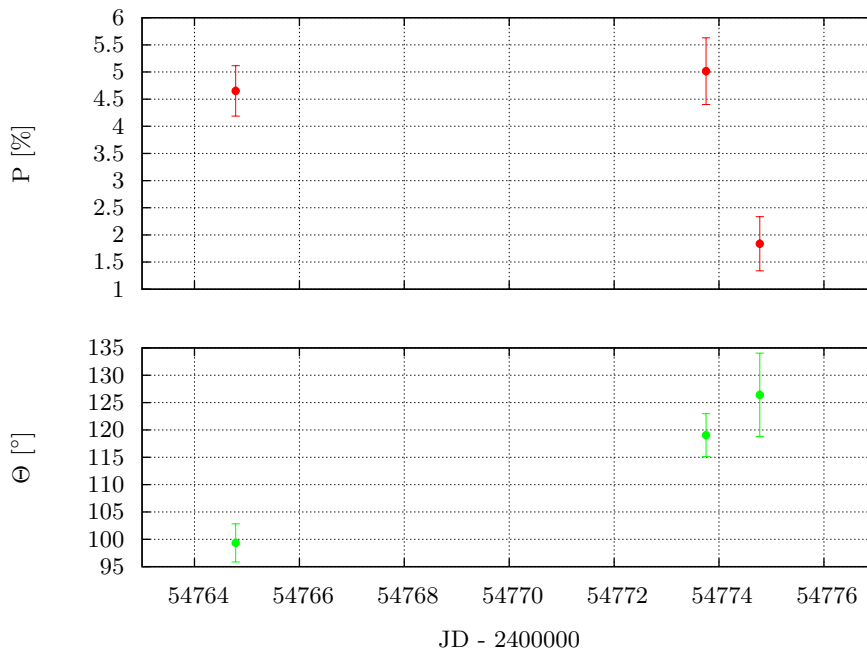
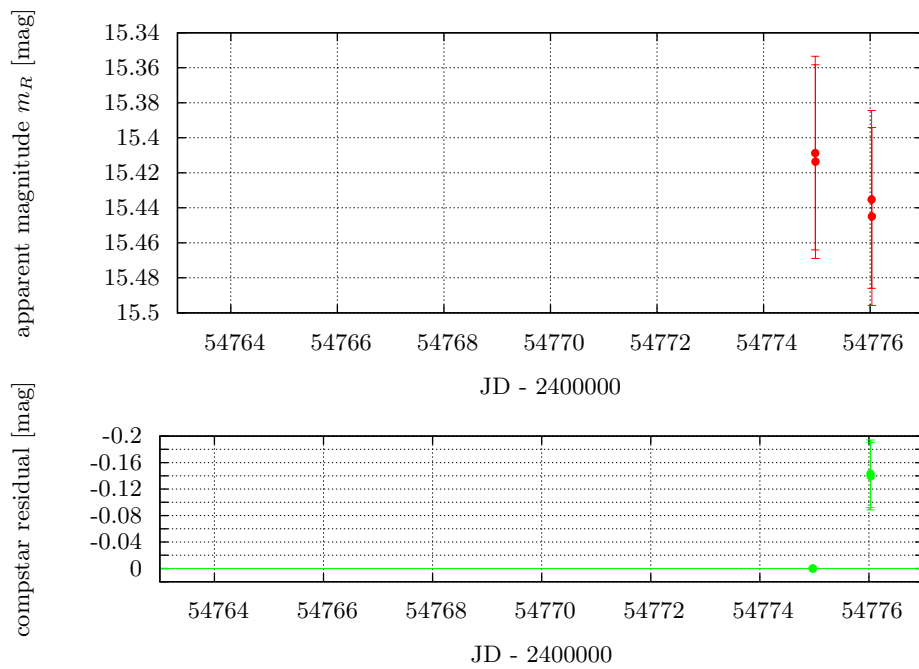
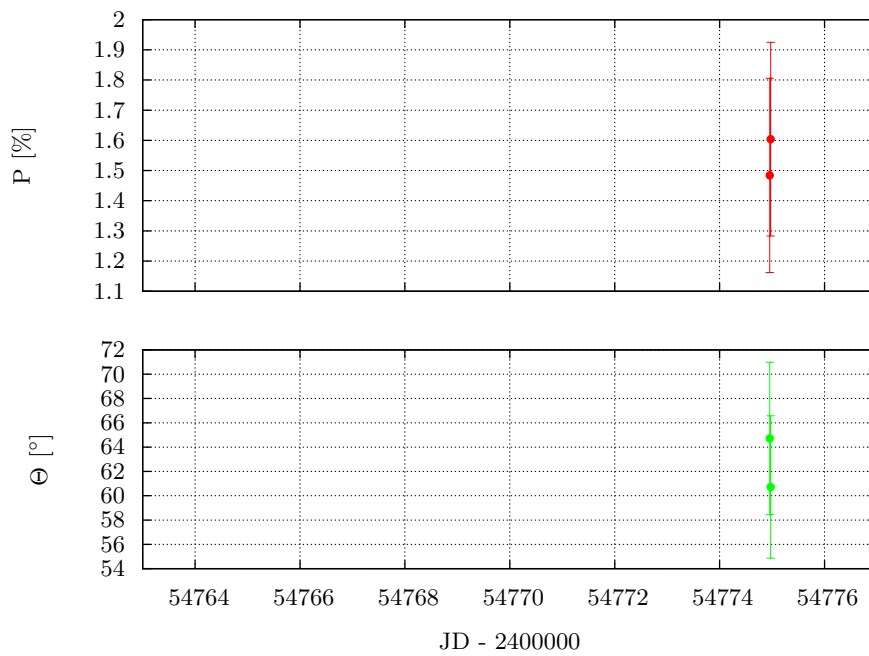
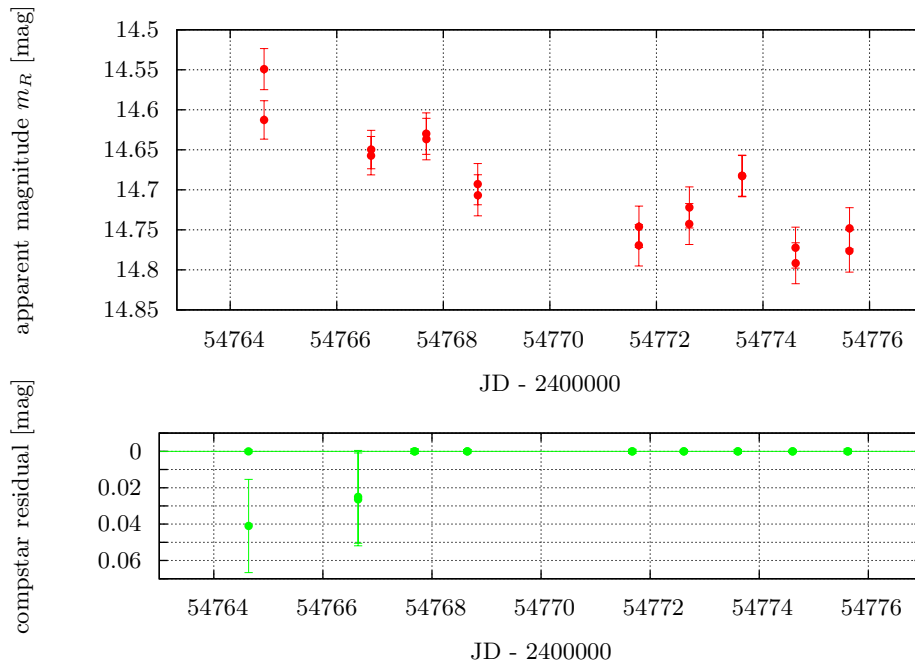
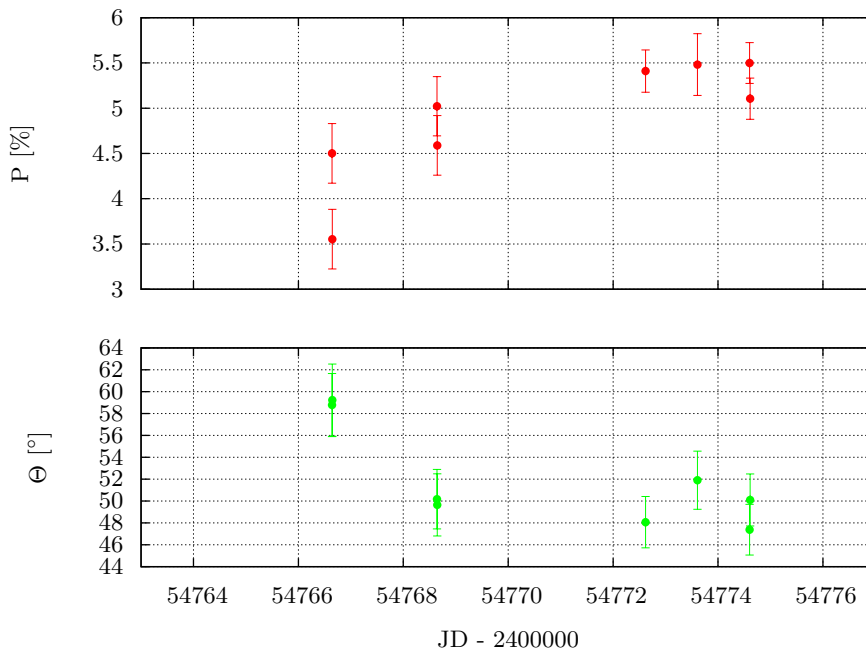


Figure B.6: Polarimetric Results of **AO 0235+164** of the October/November Run 2008

Figure B.7: Photometric Results of **CTA 102** of the October/November Run 2008Figure B.8: Polarimetric Results of **CTA 102** of the October/November Run 2008

Figure B.9: Photometric Results of **1ES 0033+595** of the October/November Run 2008Figure B.10: Polarimetric Results of **1ES 0033+595** of the October/November Run 2008

Figure B.11: Photometric Results of **1ES 0806+524** of the October/November Run 2008Figure B.12: Polarimetric Results of **1ES 0806+524** of the October/November Run 2008

Figure B.13: Photometric Results of **1ES 1959+650** of the October/November Run 2008Figure B.14: Polarimetric Results of **1ES 1959+650** of the October/November Run 2008



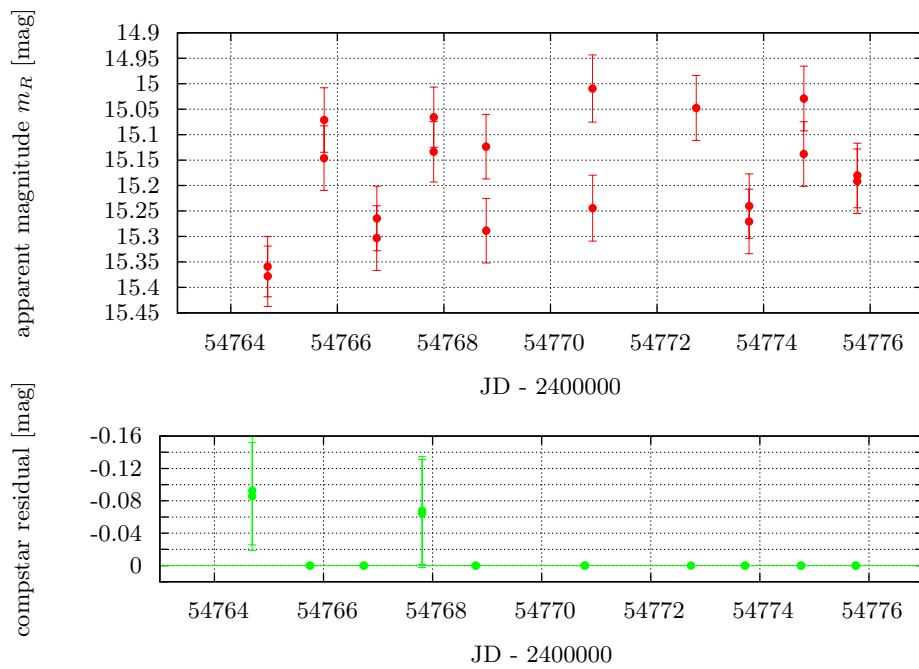


Figure B.15: Photometric Results of **1ES 2344+514** of the October/November Run 2008

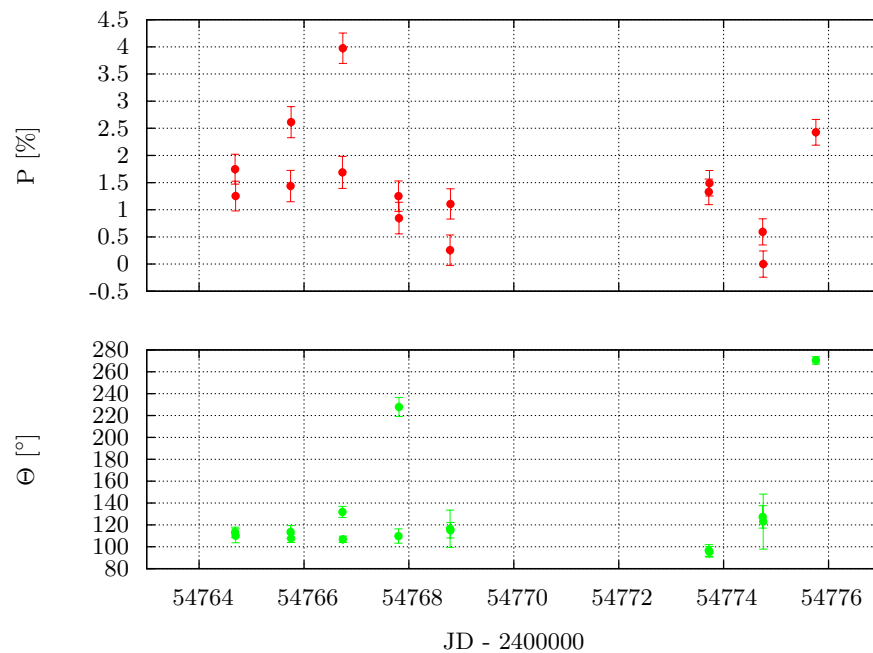


Figure B.16: Polarimetric Results of **1ES 2344+514** of the October/November Run 2008

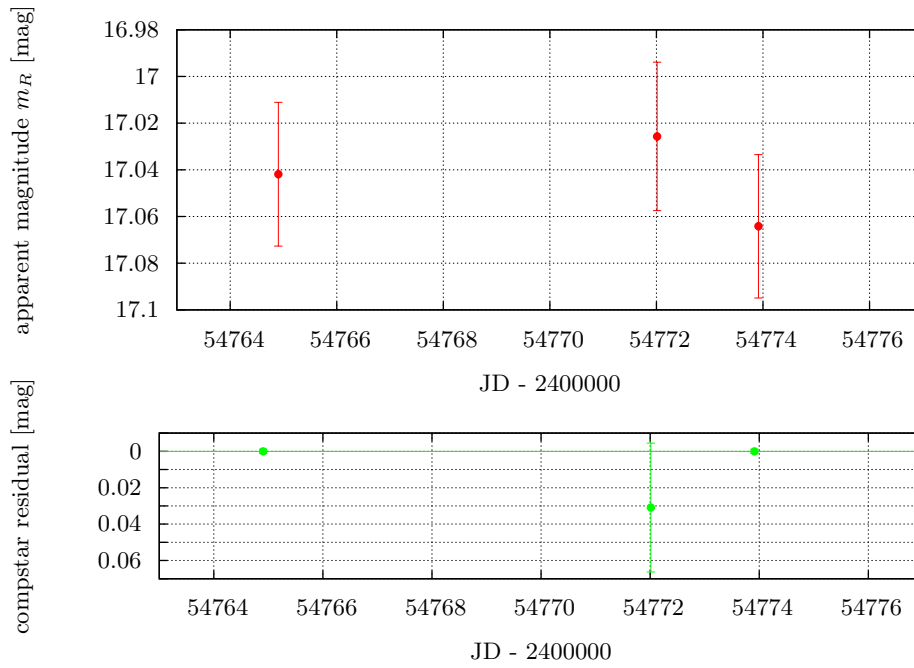


Figure B.17: Photometric Results of **PKS 0420-014** of the October/November Run 2008

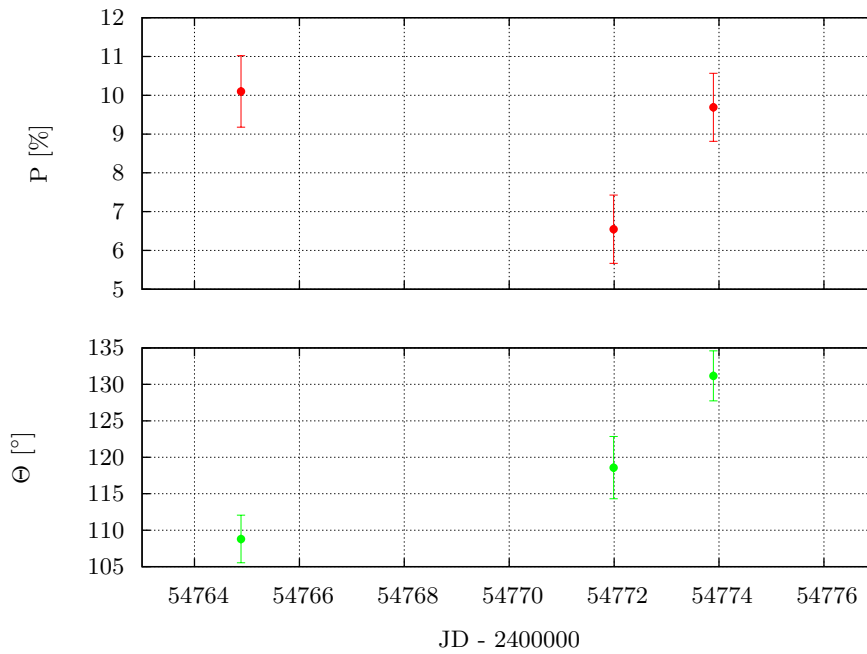


Figure B.18: Polarimetric Results of **PKS 0420-014** of the October/November Run 2008

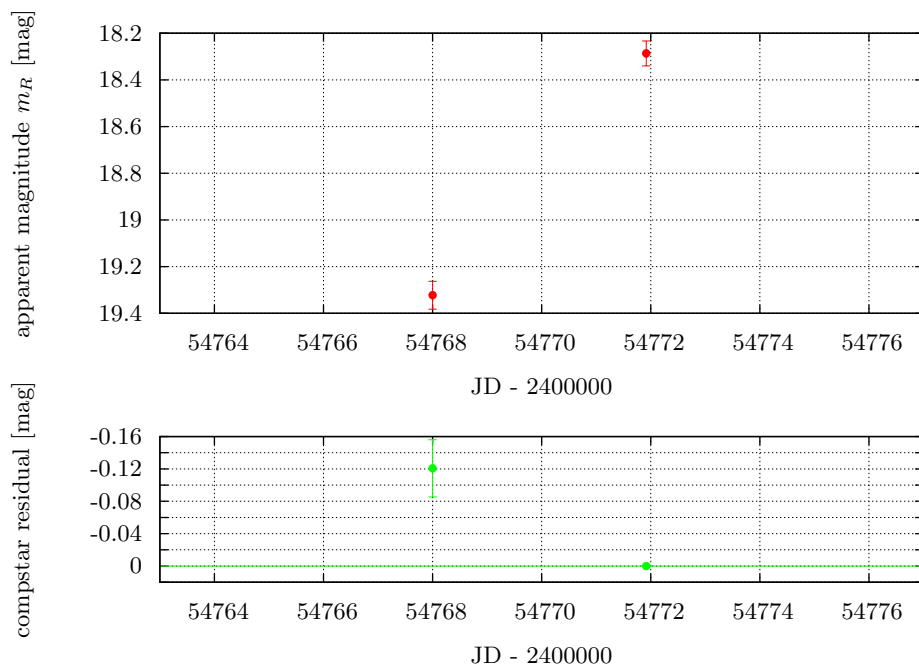
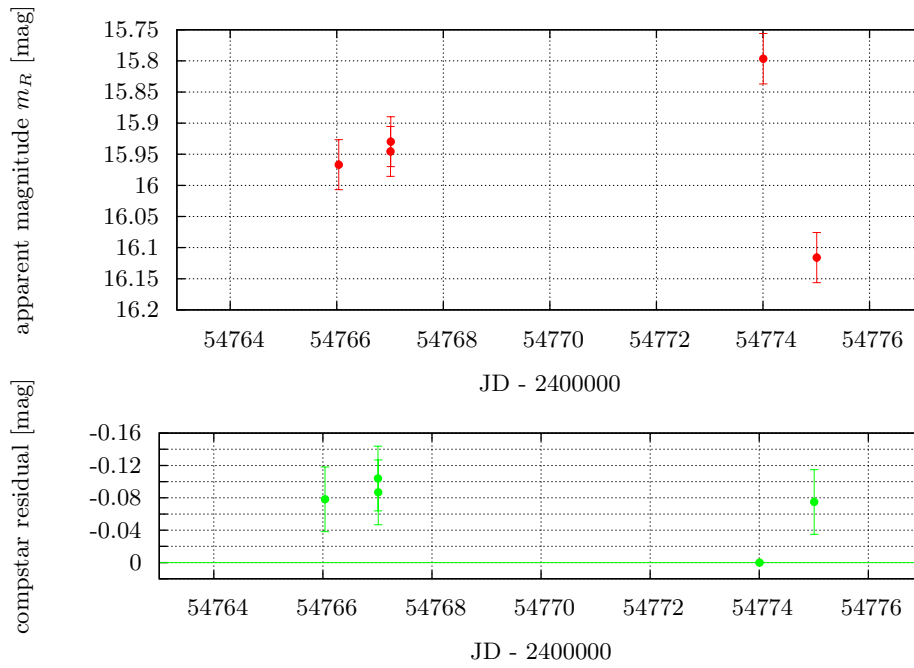
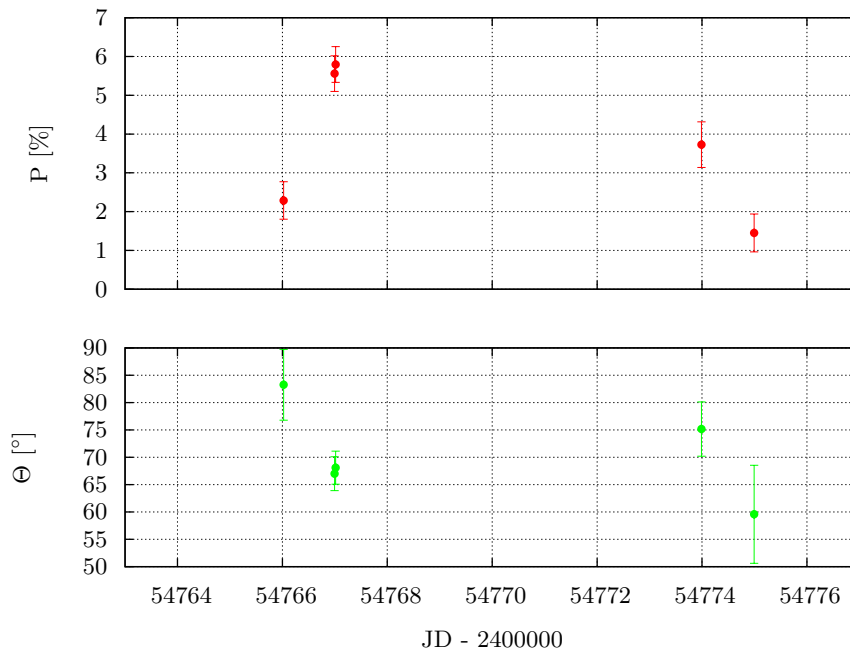


Figure B.19: Photometric Results of **PKS 0528+134** of the October/November Run 2008

Figure B.20: Photometric Results of **PKS 0735+178** of the October/November Run 2008Figure B.21: Polarimetric Results of **PKS 0735+178** of the October/November Run 2008

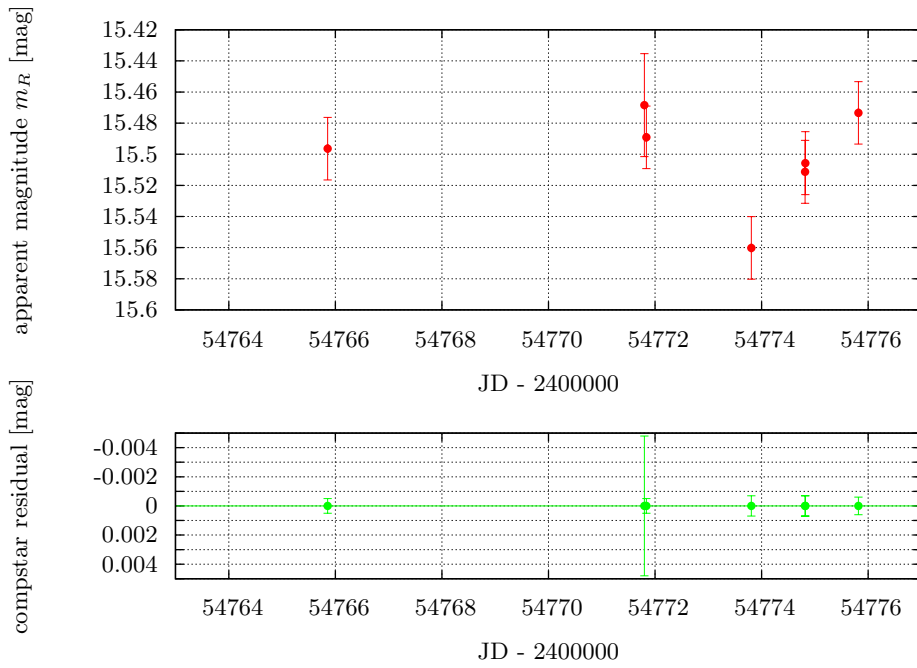


Figure B.22: Photometric Results of **RGB 0136+391** of the October/November Run 2008

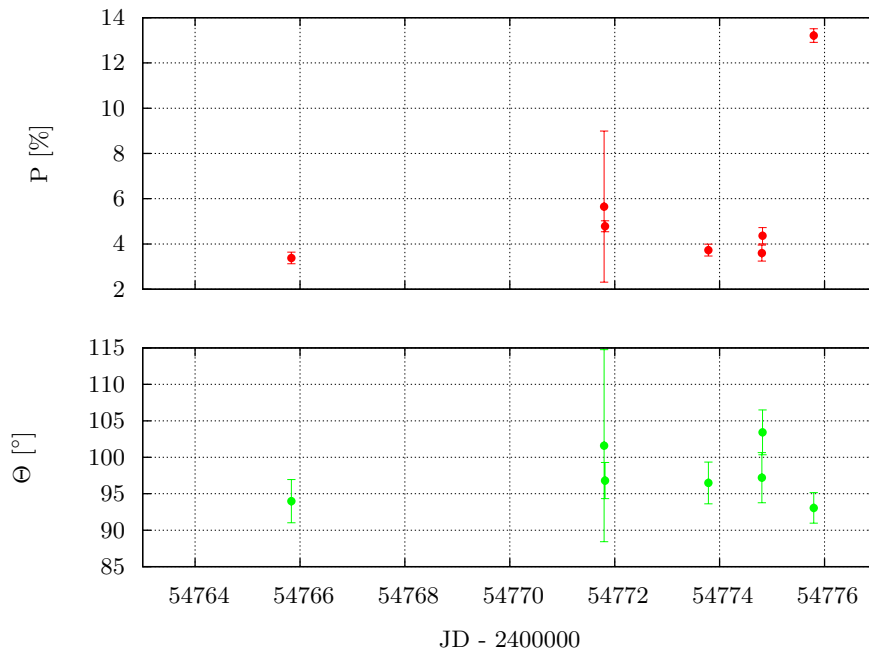
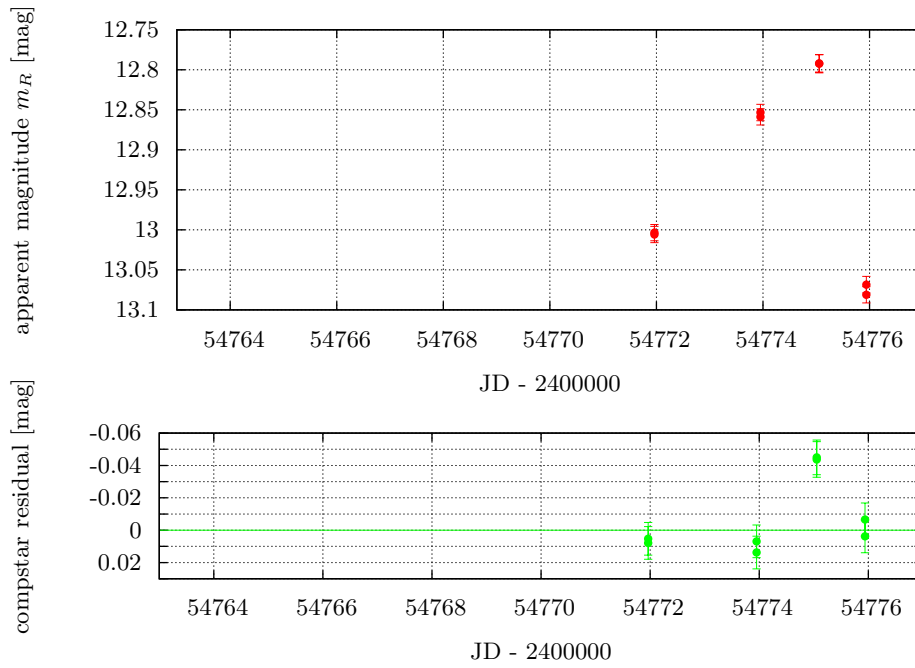
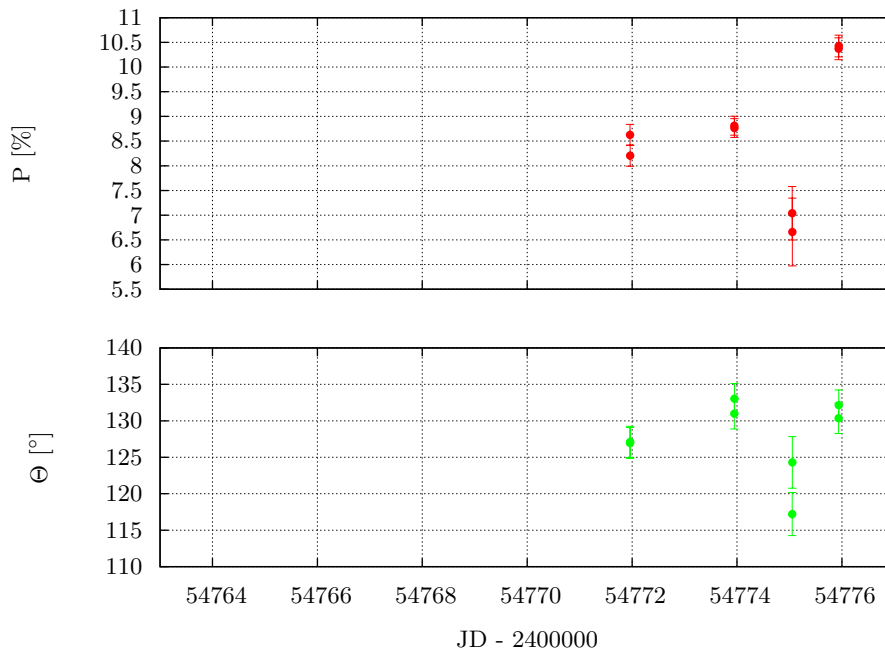


Figure B.23: Polarimetric Results of **RGB 0136+391** of the October/November Run 2008

Figure B.24: Photometric Results of **S5 0716+714** of the October/November Run 2008Figure B.25: Polarimetric Results of **S5 0716+714** of the October/November Run 2008

# Appendix C

## Using the Polima Pipeline

In the following sections it is outlined, how to use the pipeline tasks properly.

The user starts with a set of object and correction FITS images, which are all located in the same directory.

### C.1 Image Reduction

The user has to take care, that the image type ('flat', 'bias', 'object' etc.) is assigned properly to each image. Later changes are possible, but are easiest done here. Checking can be done using the IRAF task `ccdlist`. The output may look like this:

```
polima> ccdlist *
3c2730001o.fits[1076,1024] [ushort] [object] [0]:3c273
3c2730002o.fits[1076,1024] [ushort] [object] [90]:3c273
3c2730003o.fits[1076,1024] [ushort] [object] [45]:3c273
3c2730004o.fits[1076,1024] [ushort] [object] [135]:3c273
3c2730005o.fits[1076,1024] [ushort] [object] [0]:3c273
3c2730006o.fits[1076,1024] [ushort] [object] [90]:3c273
...
bias0001b.fits[1076,1024] [real] [zero] [135] [0]:bias
bias0002b.fits[1076,1024] [real] [zero] [135] [0]:bias
bias0003b.fits[1076,1024] [real] [zero] [135] [0]:bias
...
flat0002f.fits[1076,1024] [real] [flat] [0] [0Z]:flat
flat0003f.fits[1076,1024] [real] [flat] [0] [0Z]:flat
flat0004f.fits[1076,1024] [real] [flat] [0] [0Z]:flat
flat0005f.fits[1076,1024] [real] [flat] [0] [0Z]:flat
...
```

The third column in squared brackets designates the image type. Another important column is the following one, which displays the polarimeter angle, which should be correct, too. Usually, with the use of macros during the observations, there are no problems to be expected.

After checking for consistency, header data have to be processed using `polidentify`. It has to be applied to the complete image set:

```
polima> polident *fits
  processing 3c2730001o.fits
  processing 3c2730002o.fits
  processing 3c2730003o.fits
  processing 3c2730004o.fits
  ...
  processing s09540005o.fits
  processing s09540006o.fits
  processing s09540007o.fits
  processing s09540008o.fits
-> object identification completed
```

In this case, no warnings are displayed and the user may proceed with image reduction using `polprocess`.

However, warnings may be displayed. There are two possible problems:

- Warning: image n030031o.fits has a peculiar POLANGLE value, please check! IMAGETYP set to badpolangle
- Warning: unknown object with residual 678.3 arcmins, image file: n030024o.fits

In the former case, the polarimeter angle set in the *polangle* FITS header descriptor is not contained in the set of '0', '45', '90' and '135'. The user has to adjust for the correct angle and change the image type again:

```
polima> chpolangle n030031o.fits 0
polima> chimagetype n030021o.fits object
```

In the latter case, the residual of image coordinates and pointing coordinates is extremely large. Either, the object imaged here is not part of the reference-catalog-file or the telescope is pointing for an arbitrary position due to correction image acquisition. In the former case, the actual object name has to be set using `chobject n030024o.fits real_objectname`. Otherwise, one should check again for the correct image type flag.

Finally, image reduction can be started:

```
polima> polpro *fits redpath=./
... setting up instrument
... starting image reduction
... processing bias images
```



```

... processing flatfield images
... processing object images
    processing 3c2730001o.fits
    processing 3c2730005o.fits
    processing 3c2730004o.fits
    processing 3c2730008o.fits
...
    processing mk5010003o.fits
    processing mk5010007o.fits
    processing mk5010002o.fits
    processing mk5010006o.fits

---> image reduction completed, have a good night!

```

Reduced images are stored in the same directory in this case.

If the user wants to use his own set of correction images, he can do this by typing for instance:

```

polima> polpro *fits create_bias- biasfile=mybias.fits create_flat-
        flatlistfile=myflats.lst flatprefix=myflat_ redpath=./

```

## C.2 Post Reduction Handling

Application of the `popol`-script is mandatory for the use of analysis tools, due to the creation of coordinate- and reference-magnitude-files. This is done using:

```

polima> popo *fits crop+ wcs+ bright-

```

Cropping is highly recommended; `wcs` is used for object images, `bright` for standard star images. There is a lot of output which is usually not of interest. It is just to show, the script is working.

Resulting images carry the same names as the input images but now have a `'coo'`- and a `'_ref.mag'`-file each<sup>1</sup>. The correctness of object identification can be checked using `checkcoo *fits`<sup>2</sup>. If all objects have been identified properly, the images are ready to be analyzed.

If object identification did not succeed, coordinate- and reference-magnitude-files have to be created manually. This can be done using `imexam` to determine object positions on each image. Both auxiliary files then have to be corrected or created using a text editor.

However, if only some data are corrupted, the `cpcoo`-script may be helpful. If, for instance, object identification succeeded in only one image of a complete polarimeter, the script can be used like this:

```

polima> cpcoo 3c279*26_1.fits 3c279_090_2009-04-26_1.fits center=19

```

<sup>1</sup>In the case of WCS-registration, a `'wcslog'`-file is created, too

<sup>2</sup>An opened `ds9`-window is mandatory. If not existing, type `'!ds9 &'`.

image	x_ref	y_ref	x_new	y_new	dx	dy
3c279_000_2009-04-26_1.fits	327.8	441.7	315.2	448.8	-12.6	7.1
3c279_000_2009-04-26_1.fits	355.8	78.1	343.2	85.2	-12.6	7.1
3c279_000_2009-04-26_1.fits	222.5	513.0	209.9	520.1	-12.6	7.1
image	x_ref	y_ref	x_new	y_new	dx	dy
3c279_045_2009-04-26_1.fits	327.8	441.7	319.2	445.1	-8.6	3.4
3c279_045_2009-04-26_1.fits	355.8	78.1	347.2	81.5	-8.6	3.4
3c279_045_2009-04-26_1.fits	222.5	513.0	213.9	516.4	-8.6	3.4
image	x_ref	y_ref	x_new	y_new	dx	dy
3c279_135_2009-04-26_1.fits	327.8	441.7	332.2	449.4	4.4	7.7
3c279_135_2009-04-26_1.fits	355.8	78.1	360.2	85.8	4.4	7.7
3c279_135_2009-04-26_1.fits	222.5	513.0	226.9	520.7	4.4	7.7

In this example, the image set '3c279\*26\_1.fits' is reprocessed using the reference image '3c279\_090\_2009-04-26\_1.fits'. The `centerbox` parameter is chosen to be '19' since focus was quiet bad. A second check using `checkcoo 3c279*26_1.fits` reveals perfect identification.

### C.3 Image Analysis

Due to the analogy of the `dophotometry` and `dopolarimetry` script, both are presented here together.

Photometry using fitted elliptical apertures may look like this:

```
polima> dophot 3c279*26_1.fits fit+ ell+ ap=2.3 writetotable+ tablefile=phot.tbl
using 3c279_000_2009-04-26_1.fits
-> aperture would be too large (100.7 px), using aperture diameter of 100.0 px
using 3c279_045_2009-04-26_1.fits
using 3c279_090_2009-04-26_1.fits
using 3c279_135_2009-04-26_1.fits
photometry data read in, start calculations
source magnitude is: (16.3372 +- 0.0281) mag (see photlog for further information)
```

It is important to use an image set according to a complete polarimeter sequence. The major axis of the aperture in this case overspans 2.3 FWHM of the object's PSF. Results are written to the file 'phot.tbl'.

Polarimetry of the same image set using fix circular apertures may look like this:

```
polima> dopol 3c279*26_1.fits fit- ap=30 writetotable+ tablefile=pol.tbl
using 3c279_000_2009-04-26_1.fits
using 3c279_045_2009-04-26_1.fits
using 3c279_090_2009-04-26_1.fits
```

using 3c279\_135\_2009-04-26\_1.fits

Stokes parameter

I = 94100.48+-576.51, Q/I = 0.06163+-0.00877, U/I = -0.03025+-0.00857

-> polarization degree [biased] p = 6.865+-0.874  
polarization angle Theta = 166.93+-3.59 degree

---> bias corrected polarization degree: p\_0 = 6.753+-0.874

The use of fitted/fix or circular/elliptical apertures is the same in both tasks.



## Appendix D

# Pipeline Source Code

In order to limit the number of pages<sup>1</sup> in this work, the source code of the pipeline can be downloaded from the author's homepage<sup>2</sup>.

---

<sup>1</sup>The complete source code covers 4424 lines, which would end up in more than 102 additional pages.

<sup>2</sup><http://www.lsw.uni-heidelberg.de/users/mmommert/>

# Index

- 3 $\sigma$  data set, 86
- 3 $\sigma$ -selection, 86
  
- accretion disk, 14
- active galaxy, 10
- ADU, 19
- AGILE, 5
- AGN, 9, 10
- airglow, 64
- airmass, 26
- aperture, 64
- avsigclip, 52, 53
  
- bias, 20
- Binning, 19
- birefringent material, 29
- BL Lac, 13
- blazar, 9, 13, 16
- blob, 11, 16
- BLR, 16
- BLRG, 13
- Blue Bump, 10
  
- calcite, 29
- circular polarization, 27
- compstar residual, 68
- coo-file, 55, 56
- coo.polygon, 67
- coordinate-file, 55, 56
- cosmics, 23
- crop (FITS header descriptor), 58
  
- dark current, 20
- date-obs (FITS header descriptor), 49
- dec (FITS header descriptor), 49
- DS9, 41
- dust torus, 16
  
- dynamical range, 19
  
- elliptical polarization, 29
- epoch (FITS header descriptor), 49
- extraordinary beam, 29
  
- FERMI, 5
- full cycle, 40
  
- gain, 19
- gain (FITS header descriptor), 49
- GASP, 5
- Glan-Taylor prism, 38
- GLAST, 5
  
- half cycle, 40
- highpol, 85
- hot pixels, 20
  
- image reduction, 20
- IMWCS, 42
- IRAF, 41
  
- jd (FITS header descriptor), 49
  
- linear polarization, 27
  
- masterbias, 23
- masterdark, 23
- masterflat, 23
- mean, 23
- mean time of exposure, 69
- median, 23
  
- NLR, 16
- NLRG, 13
  
- object code, 7
- ordinary beam, 29
- overscan, 20

---

OVV, 13

photometric error, instrumental, 26

photometric error, total, 26

PI, 5

point spread function, 63

polangle (FITS header descriptor), 49

polarimeter, 31

polarimeter angle, 38

polarization analyzer, 31

polarization angle, 27

polarization degree, 27

polarization plane, 27

polima package, 41

polygon-file, 67

PSF, 63

QSO, 12

quantum efficiency, 19

quasar, 10, 12

ra (FITS header descriptor), 49

Radio galaxies, 13

radio-lobes, 14

radio-loud, 10, 12

radio-quiet, 10, 12

radio-selected, 12

rdnoise (FITS header descriptor), 49

readout noise, 20

ref.mag-file, 55, 56

reference-catalog-file (`polidentify`), 47

reference-magnitude-file, 55, 56

relativistic beaming, 18

S/N ratio, 24

secpix (FITS header descriptor), 49

Seyfert galaxy, 9, 12

Seyfert Type 1, 12

Seyfert Type 2, 12

shutter, 20

SKY2XY, 43

SPM project, 5

statsec, 52

Stokes vector, 30

subsets, 50

synchrotron emission, 14, 18, 32

tdec (FITS header descriptor), 49

tjd (FITS header descriptor), 49

tra (FITS header descriptor), 49

Type 1-AGN, 13

Type 2-AGN, 13

USNO-A2.0, 42

ut (FITS header descriptor), 49

WCS, 42

WEBT, 5

X-ray-selected, 12

zeropol, 89





# Bibliography

- [Ant93] R. Antonucci. Unified models for active galactic nuclei and quasars. *Annual Review of Astronomy and Astrophysics*, 31:473–521, 1993.
- [Dav90] Lindsey Elspeth Davis. *A User's Guide to the IRAF Apphot Package*. National Optical Astronomy Observatories, August 1990.
- [Dem06] Wolfgang Demtroder. *Experimentalphysik 2*. Springer Berlin Heidelberg, 2006.
- [Eea98] J. Echevarría et al. Site testing at observatorio astronómico nacional in san pedro mártir. *Revista Mexicana de Astronomía y Astrofísica*, 1998.
- [Hea] David Hiriart et al. *POLIMA - Manual Usuario*. Instituto de Astronomía, UNAM.
- [How06] Steve B. Howell. *Handbook of CCD Astronomy*. Cambridge University Press, 2006.
- [Mig99] Kenneth J. Mighell. Algorithms for ccd stellar photometry. *ASP Conf. Ser.*, 1999.
- [Sch06] Peter Schneider. *Extragalactic Astronomy and Cosmology*. Springer Berlin Heidelberg, 2006.
- [SP01] W.J. Schuster and L. Parrao. The atmospheric extinction of san pedro mártir. *Revista Mexicana de Astronomía y Astrofísica*, 2001.
- [SS85] J. F. L. Simmons and B. G. Stewart. Point and interval estimation of the true unbiased degree of linear polarization in the presence of low signal-to-noise ratios. *Astronomy and Astrophysics*, 142:100–106, January 1985.
- [Tin96] Jaap Tinbergen. *Astronomical polarimetry*. Cambridge University Press, 1996.
- [UP95] C. M. Urry and P. Padovani. Unified Schemes for Radio-Loud Active Galactic Nuclei. *Publications of the Astronomical Society of the Pacific*, 107:803–+, September 1995.
- [Wat01] Richer Watson. *CCD Imaging at the OAN-SPM 84-cm Telescope*. <http://www.astrossp.unam.mx/resast/man84cm/manual-en.html>, 04 2001.
- [Wea04] Alan Watson et al. Annual report on ccd imaging at the oan. Technical report, Instituto de Astronomía, UNAM, 2004.



# Appendix E

## Acknowledgments

Ich danke zuallererst *Jochen Heidt* für seine ausgezeichnete Betreuung - ob an der Sternwarte, in Mexiko oder im Fussballstadion. Das von dir vermittelte Wissen übersteigt die Durchführung von Beobachtungen, Photometrie und Polarimetrie bei weitem und hätte diese Arbeit nur noch dicker gemacht<sup>1</sup>. Vielen Dank für deine tatkräftige Unterstützung, dein mir entgegengebrachtes Vertrauen und deine Förderung!

Ein besonderer Dank geht an *André Germeroth* in seiner Funktion als Quasi-Zweitbetreuer, Zimmernachbar, fachlicher und sprachlicher Berater, Zuhörer, Erzähler, Kummerkasten, Instituts-Kindergarten-Mitglied, Kakteenpfleger (Grüße an Sancho, Pancho und Julio), Waldorf (oder Statler, je nachdem), Gründungsmitglied des 'Toolbag Observation Center'<sup>2</sup> und jetzigem Direktor des 'Toolbag Memorial Center'.

Außerdem danke ich den Korrekturlesern<sup>3</sup> dieser Arbeit: *Stephanie Schwemmer*, *André Germeroth* und *Marcus Hauser*. Vielen Dank für das Aufpüren der überzähligen Apostrophen und fachlichen Fehler.

Ich danke meinen Eltern, *Christa* und *Peter Mommert*, und meinem Bruder *Sascha Mommert* für die moralische und finanzielle Unterstützung während meines Studiums, der Zeit auf dem Kolleg und davor. Ohne euch stünde ich nun nicht, wo ich bin.

Ein besonderer Dank gilt meinen Freunden, die mich all die Jahre unterstützt und aufgemuntert haben. Ich danke ganz besonders *Michaela* dass sie nach all den Jahren immer noch für mich da ist und dass das auch immer sein wird. Danke auch an *Sonja* für die schöne Zeit im Stadion und auch ausserhalb und *Stephi* als beste Kletterpartnerin aller Zeiten.

Außerdem danke ich unter anderem *Damian* ('rocket science!'), *Julien* ('ohne Worte'), *Patrick* ('geh'ma äнна trinke?') und *Waldi* ('mööööööö!') für die nötige Ablenkung von der Arbeit und vom Studium.

Allgemein möchte ich der *Happel-Besatzung* und allen *Sternwartenmitarbeitern* für die schöne

---

<sup>1</sup>... allerdings fand ich beispielsweise ein Kapitel 'Survival in Strange Foreign Countries' auch etwas unangebracht.

<sup>2</sup>Ja, wir haben es gesehen!

<sup>3</sup>Beschwerden sind an sie zu richten.

---

Zeit danken. Es wird jetzt wieder ruhiger im Happel.

Muchas gracias an *David Hiriart* und die *Mitarbeiter des OAN* (besonders die Küche!) für die Unterstützung bei meinen Aufenthalten am Observatorium, die netten Unterhaltungen<sup>4</sup> und *Fernando* für die Fahrten nach San Diego.

Außerdem möchte ich den Mitgliedern der '*Eisgruppe*' des 'Instituts für Umweltphysik' für die tolle Zeit bei euch danken. Danke, *Dietmar*, für die langjährige Unterstützung und das Vertrauen, *Barbara*, *Christoph* und *Pascal* ('dem Basgall!') für die schöne Zeit und das Skifahren!

Ich danke meiner WG im 'Haus das Verrückte macht', die sich über zwei Jahre immer wieder mal geändert hat aber trotz (oder gerade wegen) des Chaos mir immer wieder ans Herz gewachsen ist: *Ines*, *Mareike*, *Erik*, *Julien* und *René* ('Ränääii!').

Ich danke meinen Kommilitonen für die Hilfe und die schöne Zeit während des Studiums: *Anika*, dafür dass sie immer für mich da war, *Alex*, *Philipp*, *Simon* und *Stefan* für die Hilfe und Unterstützung. Ohne euch hätte ich Mathe und Theo wohl nie bestanden.

Ein weiterer Dank geht an die Musikkneipe *Eckstein* für die nette Lern-, Arbeits- und Entspannungsumgebung, die Übertragung aller Fussballspiele und den Kicker.

Ich danke *Ali* von *Alamo Car Rentals* für den Ford Mustang, den ich eine Woche durch die USA jagen durfte und der *Amerikanischen Küche*, die mir vor Augen führte, wie gut die Deutsche ist. Weiterhin danke ich dem *Auswärtigen Amt* und den *Medien* für die Panikmache wegen des H1N1-Ausbruchs während meines zweiten Mexiko-Aufenthalts. Ansonsten wäre es nur halb so spannend gewesen. Außerdem danke ich nochmal *Waldi*, dass er mich bei unserem Trip ausgehalten hat und die abgefahrene Zeit im Renter-Schlachtschiff.

Ausserdem danke ich *failblog.org*, diversen online-Ausgaben namhafter *Zeitungen* und den vielen lernresistenten *Verschwörungstheoretikern* ('Mal sehen, was da so kommen wird') für die nette Ablenkung von der Arbeit.

Zuletzt möchte ich *Ulrich Bastian*, der mich auf die Idee des Studiums brachte und allen Menschen am *Staatlichen Kolleg Mannheim* danken, die mich auf dem Weg zum Abitur begleiteten und daraus eine tolle Zeit gemacht haben.

Sollte hier jemand fehlen, so liegt das nicht an ihm, sondern an meiner Panik in den letzten Stunden vor Abgabe dieser Arbeit. Aus diesem Grunde<sup>5</sup>:

mommert@lsw:~/> danke \* &

---

<sup>4</sup>+: ¿Este militar? -: Si. +: ¿Por qué? -: Drogas. +: Oha.

<sup>5</sup>Nerd → Deutsch: Ich danke allen, die mich unterstützt haben!



## Erklärung

Ich versichere, dass ich diese Arbeit selbstständig verfasst habe und keine anderen als die angegebenen Quellen und Hilfsmittel benutzt habe.

Michael Mommert  
Heidelberg, den 28. August 2009